NASA Contractor Report 3192

# Exploratory Studies of the Cruise Performance of Upper Surface Blown Configurations

## Experimental Program - Test Facilities, Model Design, Instrumentation, and Low-Speed, High-Lift Tests

J. A. Braden, J. P. Hancock,
K. P. Burdges, and J. E. Hackett

CONTRACT NAS1-13871
JUNE 1980

NASA

NASA Contractor Report 3192

# Exploratory Studies of the Cruise Performance of Upper Surface Blown Configurations

## Experimental Program - Test Facilities, Model Design, Instrumentation, and Low-Speed, High-Lift Tests

J. A. Braden, J. P. Hancock,
K. P. Burdges, and J. E. Hackett
*Lockheed-Georgia Company*
*Marietta, Georgia*

Prepared for
Langley Research Center
under Contract NAS1-13871

NASA
National Aeronautics
and Space Administration

**Scientific and Technical
Information Office**

1980

## FOREWORD

This document is submitted in accordance with the requirements of NASA Contract NAS1-13871, Exploratory Studies of the Cruise Performance of Upper Surface Blown Configurations. W. C. Sleeman, Jr. is the NASA-Langley Contract Monitor and J. A. Braden is the Lockheed-Georgia Project Manager.

The technical results under this contract are presented in five reports. For convenience, the overall program documentation is summarized below:

### DOCUMENTATION SUMMARY

| CR-Number | Title |
|---|---|
| CR-3193 | Summary Report |
| CR-3192 | Experimental Program - Test Facilities, Model Design, Instrumentation, and Low-Speed, High-Lift Tests |
| CR-159134 | Experimental Program - High-Speed Force Tests |
| CR-159135 | Experimental Program - High-Speed Pressure Tests |
| CR-159136 | Program Analysis and Conclusions |

TABLE OF CONTENTS

## TABLE OF CONTENTS (CONT'D)

## LIST OF FIGURES

## LIST OF FIGURES (CONT'D)

## LIST OF FIGURES (CONT'D)

## LIST OF FIGURES (CONT'D)

## LIST OF TABLES

## SUMMARY

The purpose and scope of the Cruise Performance Data Base Contract (NAS1-13871) are reviewed briefly in Section I of this document. Descriptions are provided for the test facilities employed in the total program. The model design approach is discussed and dimensional definitions are presented for the various hardware components. A detailed description of the wing-nacelle fillet design process is also presented. Hardware used for calibration of the nozzles and instrumentation arrangements for the various test setups are described. For the low speed, high lift test, the objectives and run schedule are then described in some detail. The test results presented include installed simulator performance, static performance of nozzle-wing-flap system, and lift characteristics at different thrust coefficients as a function of alpha, moment coefficient, and drag coefficient. Oil flow photographs of the flow over the wing-flap-nacelle surfaces are also presented. Test results from this program are compared with those obtained from alternate powered lift systems, such as the externally blown flap and augmentor wing, and also with upper surface blowing (USB) test results obtained in other facilities. Data from this test are also correlated with theoretical program results and with the analytical computer program used for predicting the high lift performance of the Task II aircraft. The major conclusions are that USB high lift performance is competitive with a similar externally blown flap (EBF) system, that simple slot blockage works almost as well as a smooth Coanda plate, and that the data obtained correlate well with

data from large scale USB models tested in other facilities and also with data produced by current theoretical and analytical programs.

## 1.0 INTRODUCTION

In early 1975, the NASA awarded a contractual effort (NAS1-13871) to the Lockheed-Georgia Company for the acquisition of a high-speed, experimental data base for aircraft configurations featuring nacelles mounted on the upper wing surface. This design concept, known as upper-surface-blowing (USB), had received earlier, experimental endorsement as a viable means of achieving moderate-to-good powered lift performance along with beneficial noise reduction in the STOL environment. In the interest of further development of the USB-system, the contractual work performed by the Lockheed-Georgia Company emphasized the transonic cruise characteristics of USB-designs on an exploratory basis. The overall program was comprised of extensive experimental tests of USB-configurations in a transonic wind-tunnel, with support provided by an analytical modeling of the system, Figure 1. Testing was planned around a matrix of nozzle configurations suitable for evaluating the effects of key USB design variables. A build-up approach was used in designing the models so that, through interchangeability, a wide range of configuration combinations was possible. All model design work was performed by Lockheed, while fabrication of the models was carried out by Microcraft, Inc. of Tullahoma, Tennessee.

In addition to test facilities, model design and instrumentation, the present document describes the low-speed, high-lift tests performed and the resulting high-lift performance achieved with the USB-nacelle installation. It is to be recognized that the basic intent of the Task III Study is to demonstrate the feasibility of the system for generation of powered lift performance commensurate with desired cruise and noise footprint goals. In keeping with this objective, the low-speed tests and model described herein do not necessarily demonstrate the full, high-lift potential of the USB system.

Use of trade names or names of manufacturers in this report does not constitute an official endorsement of such products or manufacturers, either expressed or implied, by the National Aeronautics and Space Administration.

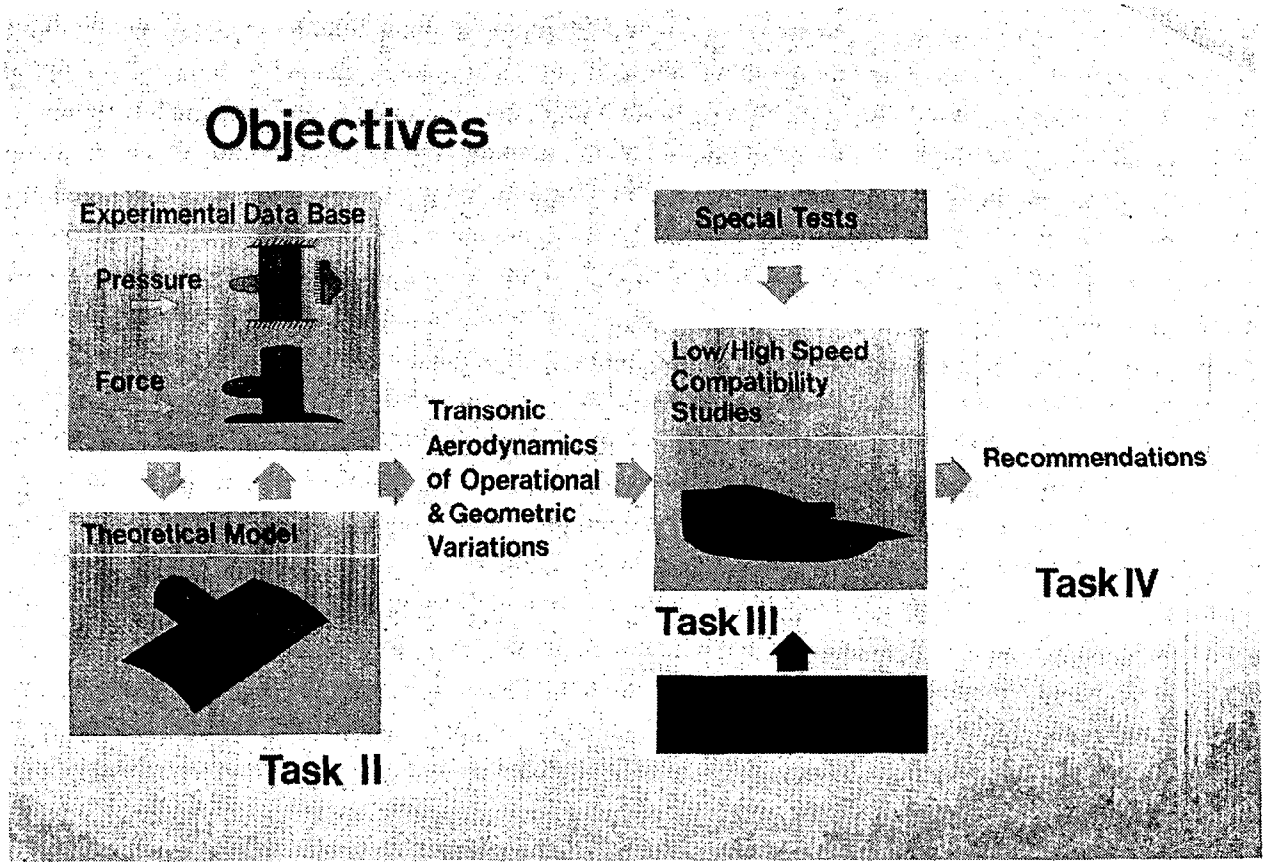


Figure 1. Major elements of USB Cruise Program.

## 2.0 LIST OF SYMBOLS

Dimensional data are presented herein in both the International System of Units (SI) and the U.S. Customary Units. The measurements and calculations were made in the U.S. Customary Units.

| | |
|---|---|
| $A$ | area, $cm^2$ ($in.^2$) |
| AR | aspect ratio |
| $c$ | local wing chord, cm (in.) |
| $\bar{c}$ | mean aerodynamic chord, cm (in.) |
| $C_D$ | model drag coefficient $D/q\ S_W$ |
| $C_L$ | model lift coefficient, $L/q\ S_W$ |
| $C_L$ | circulation lift coefficient, $L\ /q\ S_W$ |
| $C_M$ | model pitching moment coefficient, $M_Y/q\ S_W$ |
| $C_\mu$ | model gross thrust coefficient, $F_{NF}/q\ S_W$ |
| $C_T$ | nozzle gross thrust coefficient, $F/q\ S_W$ |
| $C_X$ | coefficient of total force on model in thrust direction, $= \bar{C}_{D_M}$ |
| $d_N$ | diameter of nozzle, cm (in.) |
| $D$ | model drag, N (lb) |
| $F_A$ | axial force, N (lb) |
| $F_N$ | normal force, N (lb) |
| $F_{NF}$ | model gross thrust with flaps removed, N (lb) |
| $H_j$ | jet total pressure, $N/m^2$ ($lb/in.^2$) |
| $l$ | length, cm (in.) |
| $L$ | model lift, N (lb) |
| $L_\Gamma$ | model circulation lift, N (lb) |
| $M$ | Mach number |
| $M_Y$ | model pitching moment about quarter chord, m-N (in.-lb) |
| $M_\infty$ | freestream (tunnel) Mach number |
| $P_\infty$ | freestream static pressure, $N/m^2$ ($lb/in.^2$) |
| $q_\infty$ | freestream dynamic pressure, $N/m^2$ ($lb/ft^2$) |
| $R$ | radius, cm (in.) |
| $R_N$ | Reynolds number |

| | |
|---|---|
| $S_W$ | wing area, $m^2$ ($ft^2$) |
| t | thickness, cm (in.) |
| x | distance parallel to tunnel centerline, cm (in.) |
| y | transverse (spanwise) distance, cm (in.) |
| z | vertical distance, cm (in.) |
| $\alpha$ | angle of attack, degrees |
| $\beta$ | boattail angle, degrees |
| $\delta_{ail}$ | aileron deflection angle, degrees |
| $\delta_c$ | change in flap camber angle, degrees |
| $\delta_f$ | flap deflection angle, degrees |
| $\delta_j$ | jet deflection angle, degrees |
| $\eta$ | percent semispan |
| $\eta_t$ | jet turning efficiency, $\sqrt{\left(F_N^2 + F_A^2\right)} / F_{NF}$ |

Subscripts:

| | |
|---|---|
| A | aerodynamic |
| l | lower |
| u | upper |
| M | measured |
| MAX | maximum |
| STALL | stall |

## 3.0 FACILITIES

### 3.1 Compressible Flow Facility

3.1.1 Basic Facility Description - The experimental phase of the USB-Cruise Program was formulated around the use of minimum-cost, powered models in a porous-wall blowdown test facility. This combination permitted a test program covering a comprehensive series of test configurations and parameter variations over an extensive range of test conditions. The Lockheed Compressible Flow Facility (CFF), shown in Figures 2 and 3, is a specialized, exploratory test facility capable of conducting transonic investigations at Mach numbers from 0.2 to 1.2 and Reynolds numbers up to 164 x $10^6$/m (50 x $10^6$/ft.). The tunnel is of the blowdown type, exhausting directly to the

USB CRUISE PROGRAM

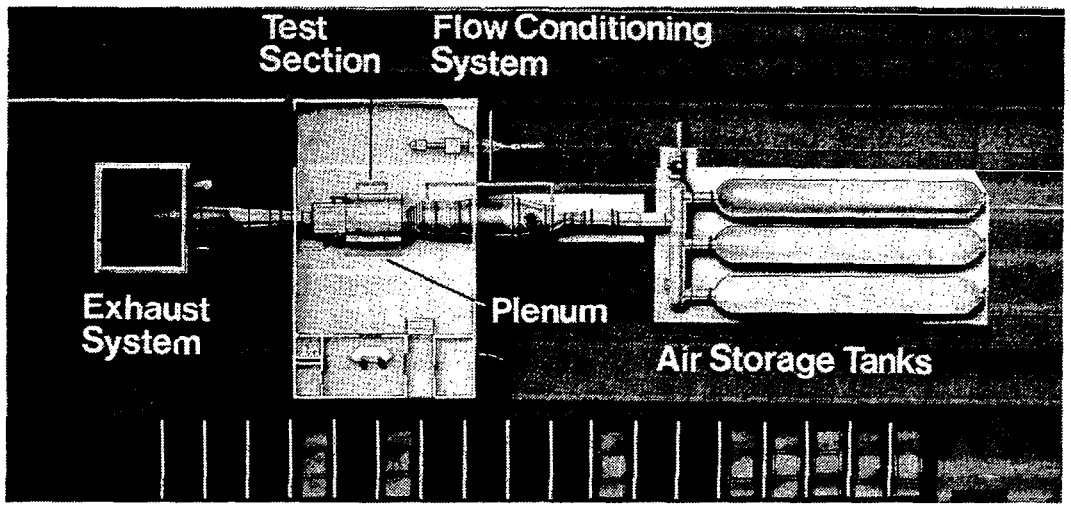


TRANSONIC BLOWDOWN TUNNEL $0.2 \leq M \leq 1.2$

HIGH REYNOLDS NUMBER CAPABILITY $164 \times 10^6$ / m ($50 \times 10^6$ / FT)

VARIABLE WALL POROSITY

MODEL BLOWING CAPABILITY 207 $N/cm^2$ (300 PSI)

Figure 2. Lockheed compressible flow facility (CFF)

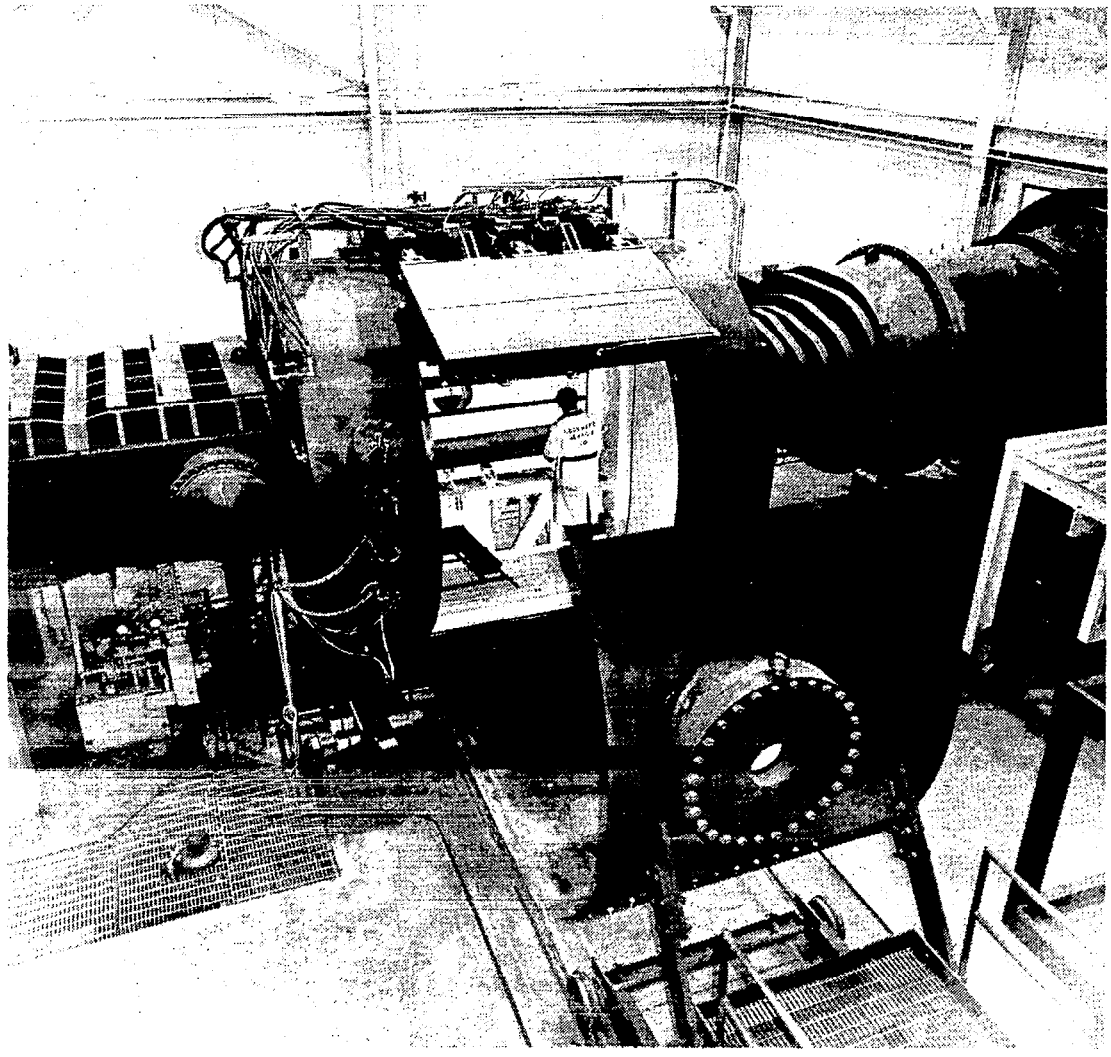

Figure 3. CFF Test Section

atmosphere. The air storage capability is 368 $m^3$ (13,000 $ft^3$) at 413 dynes/$cm^2$ (600 psia). A sleeve-type control valve accurately maintains the settling chamber stagnation pressure at selected pressures less than or equal to the 172 dynes/$cm^2$ (250 psia) maximum and at mass flow rates less than 1089 kg/sec (2400 lb/sec). The test section is 50.8 cm (20.0 in.) wide by 71.2 cm (28.0 in.) high by 183 cm (72.0 in.) long and is enclosed in a 3.7 m (12.0 ft.) diameter plenum chamber. The top and bottom walls of the two-dimensional test section have variable-porosity capability (from 0 to 10 percent), obtained by sliding two parallel plates with 0.635 cm (0.250 in.) diameter holes slanted 60 degrees from the vertical. The 2-D test section side walls are not porous. The three-dimensional test section has variable-porosity top and side walls. The bottom wall where the balance is located is not porous. The 5-component semispan balance used in these tests is located in the floor of the tunnel. High-pressure air is passed through the balance to the model engines via two opposing bellows arrangements.

3.1.2 CFF With Upstream Pipe Assembly - For some of the test configurations included in this program, it was not possible to supply an adequate flow of high-pressure nozzle air through the wing-pylon-nacelle internal duct system. To permit testing in these cases, an alternate air supply arrangement was devised, as illustrated in Figure 4. A straight section of co-annular pipe 4.35 m (14.37 ft.) long was extended into the test section from the settling chamber upstream. The inner pipe supplied the high-pressure air to the model, while the outer annulus provided a discharge path for pipe boundary layer removed near the leading edge of the nacelle forebody. Details of the annular pipe design and boundary-layer slot arrangement are included in Figure 4.

All power testing of nacelles with non-scrubbing discharges was performed using the upstream pipe. These nacelles were mounted on thin pylons and their effluxes discharged at either one-half or one full nozzle diameter above the wing surface. The upstream pipe arrangement was also extensively used for testing different nozzle chordwise discharge positions by using different length nacelle spacers.

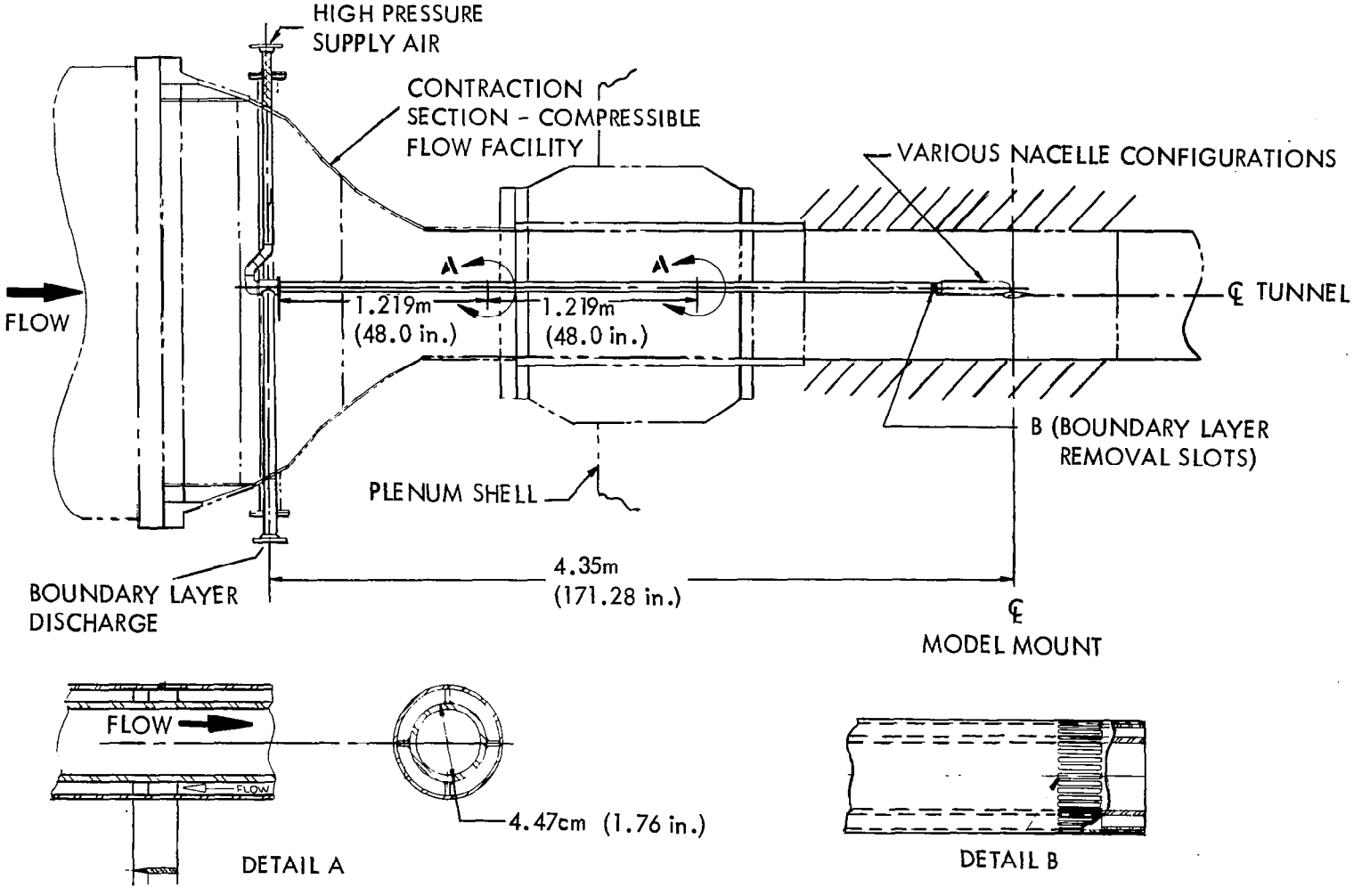


Figure 4. Model test installation with upstream pipe air supply arrangement

3.1.3 Lockheed-California 4 x 4 Wind Tunnel - The Lockheed-California 4 x 4 ft. Wind Tunnel is similar to the CFF except that it has a much larger test section flow area. For this test, a six-component wall-mounted balance was employed. The basic design and air ducting arrangement was essentially similar to the system utilized in the CFF.

## 3.2 Low-Speed Wind Tunnel (LSWT)

Nozzle calibration for the primary test and the supplementary low-speed test program were carried out in the Lockheed-Georgia Low-Speed Wind Tunnel. This facility is a horizontal, atmospheric-pressure, single-return circuit, closed-throat system with an overall circuit centerline length of 238 m (780.5 ft.). The facility has large tandem test sections that provide for testing V/STOL configurations in the larger upstream section and more conventional configurations in the downstream section.

The low-speed test section used in these tests is 7.09 m (23.25 ft.) wide 4.96 m (16.25 ft.) high and 13.11 m (43 ft.) long. The roof and floor of each test section are parallel, while the side walls diverge to account for boundary layer growth. No corner fillets are fitted. Each test section has full-height adjustable slots located in the side walls at the downstream ends to vent the operating section to atmospheric pressure. The empty test section speed range is 21.3 m/sec (70 ft/sec) to 112.8 m/sec (370 ft/sec).

Forces were measured by means of a pyramidal external balance system installed under the test section. Provision was made for ducting up to 4.55 Kg/sec (10 lb./sec.) of high-pressure air up through the balance for performing tests with powered nacelles.

## 4.0 MODEL DESIGN AND INSTRUMENTATION

The basic objective of the model design effort was to develop a wing-nacelle arrangement which could accommodate a wide range of USB nozzle types for comparative evaluation. An arrangement for metering smooth-profile, high-pressure air to the nozzle entrance was considered necessary. Means for obtaining static pressure distributions on key surface areas and for model force measurements were also required. For the low-speed, high lift test, the objective was to demonstrate USB system compatibility in the low speed regime. A representative short haul aircraft model with powered nacelles was deemed appropriate for this task.

### 4.1 Model Design Approach

To accomplish the objectives outlined above, the high-speed test configurations were developed around two wing-body combinations with untapered wings swept 0 and 25 degrees. These basic test vehicles could be combined in build-up fashion with a series of nacelle forebodies to form a wide range of powered or unpowered configurations. Figure 5 provides an exploded view of a typical example of the selected model design concept. The choice of piped-in nozzle supply air over a powered simulator was made for simplicity and economy. A smooth flow profile at the nozzle entry was ensured by a choke plate with 0.159 cm (1/16 in.) diameter holes evenly distributed over the plate. The removable nozzle block provides for the substitution of nacelles with other under-wing pylon designs as well as the conversion to the clean-wing configuration. As shown, the wing has two tangs for mounting in the two-dimensional configuration. For three-dimensional testing, one tang was removed and replaced by the tip, also shown in the figure. Although not shown here, a fuselage half-body accompanies the 3-D test installation. A remote-controlled traversing wake rake was positioned one chord length downstream to provide for complete mapping of the model/jet wake pattern.

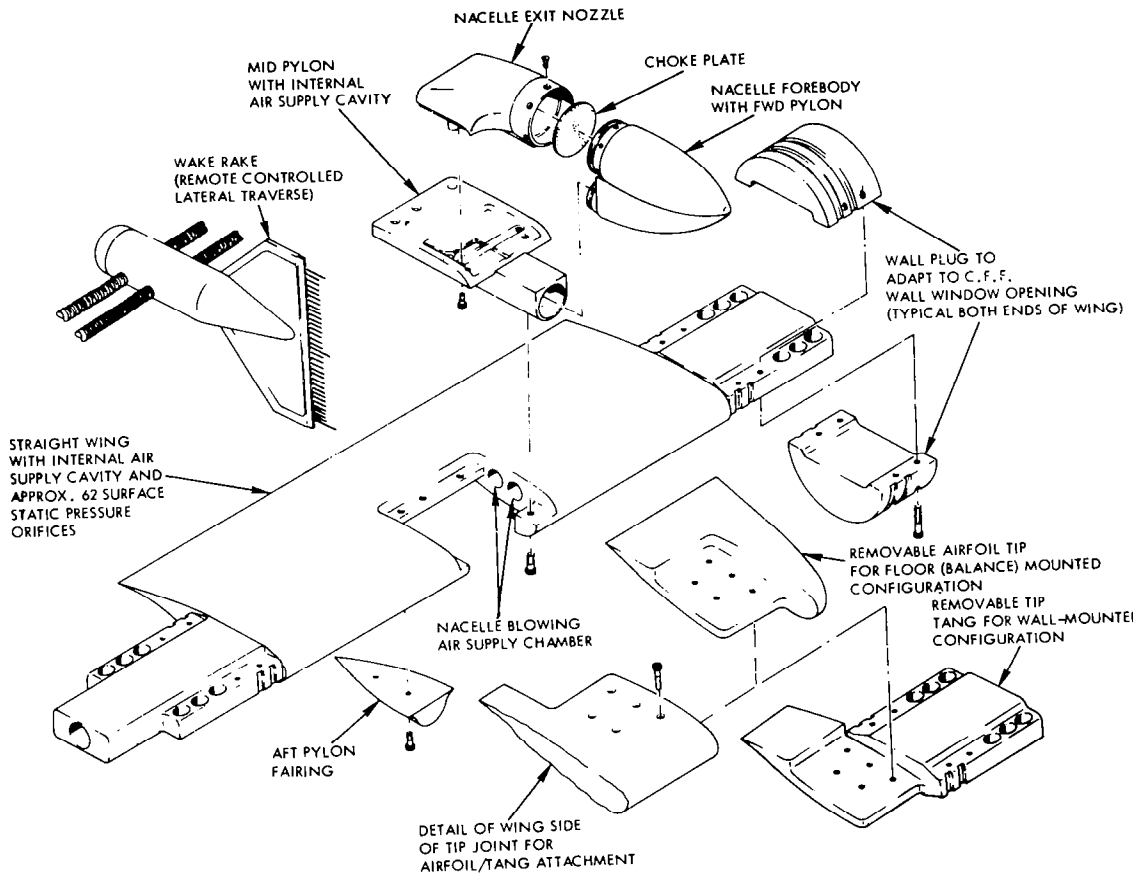


Figure 5. Exploded view of basic test model arrangement

4.1.1 Test Configurations - A front view of a 2-D model configuration mounted in the tunnel is presented in Figure 6. As the model is viewed in this photograph, nozzle supply air is ducted in from the right-hand side, while pressure tubes are routed out the left-hand side. The traversing wake rake can be seen in the background.

An example of a 3-D model configuration, shown in Figure 7, represents the long-nacelle, intermediate-size D-duct installation mounted on the same wing as shown in the previous photo (Figure 6). However, a smoother, aerodynamic tip replaced the tang on the outboard side, and a fuselage half-body covered the root section. Note, also, that for 3-D testing the model was mounted on the tunnel floor rather than horizontally on the wall. The gap between the fuselage half-body and the floor is sealed with a soft, thin strip of foam rubber. Extensive filleting smoothed out the intersections between the nacelle and the wing, and between the wing and the fuselage.

4.1.2 Wing-Body Design Details - The basic components of the fuselage half-body along with key dimensions are sketched in Figure 8. The elliptical nose and aftbody sections are common for both wing installations. Separate centerbodies are provided to allow for differences in filleting requirements at the wing-body junction. A 1.27 cm (0.5 in.) slab section separates the fuselage mid-body from the tunnel floor; this spacer approximately equals the boundary layer thickness in the test section.

The airfoil used in the design of the straight wing planform is defined in Figure 9. It is a supercritical section with 16 percent thickness and a design lift coefficient of 0.6. The design drag divergence Mach number for the clean wing case was 0.74. To develop the swept wing, it initially appeared desirable to physically sweep the straight wing and then to extend and recontour the tip. This would have resulted in an extended streamwise chord with larger wing and scrubbing area. An alternative approach was used by scaling down the straight wing by the cosine of the sweep angle ($25^{\circ}$), so that the swept-wing streamwise chord and area were identical to the

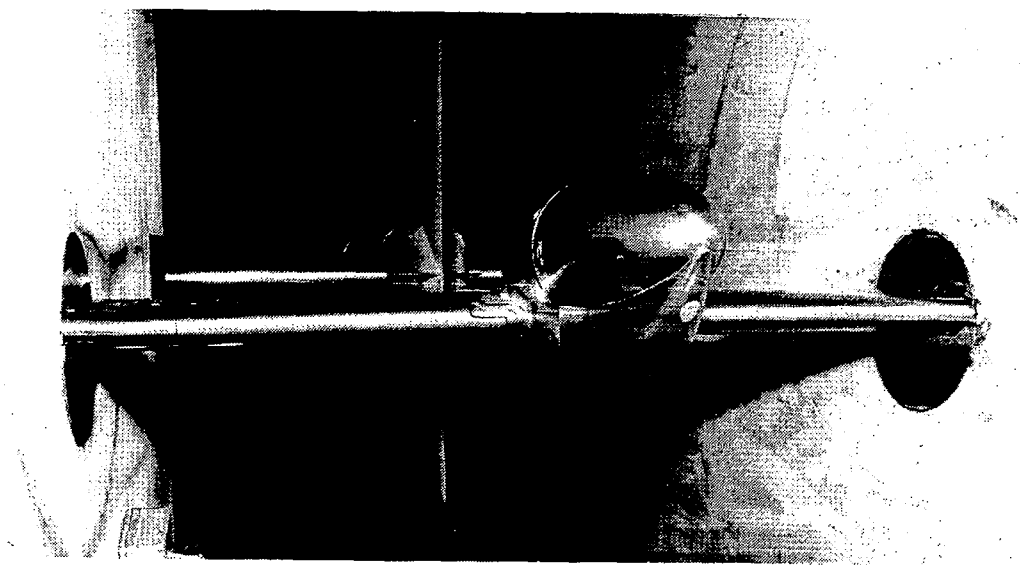

Figure 6. Two-dimensional pressure model and traversing wake rake mounted in CFF

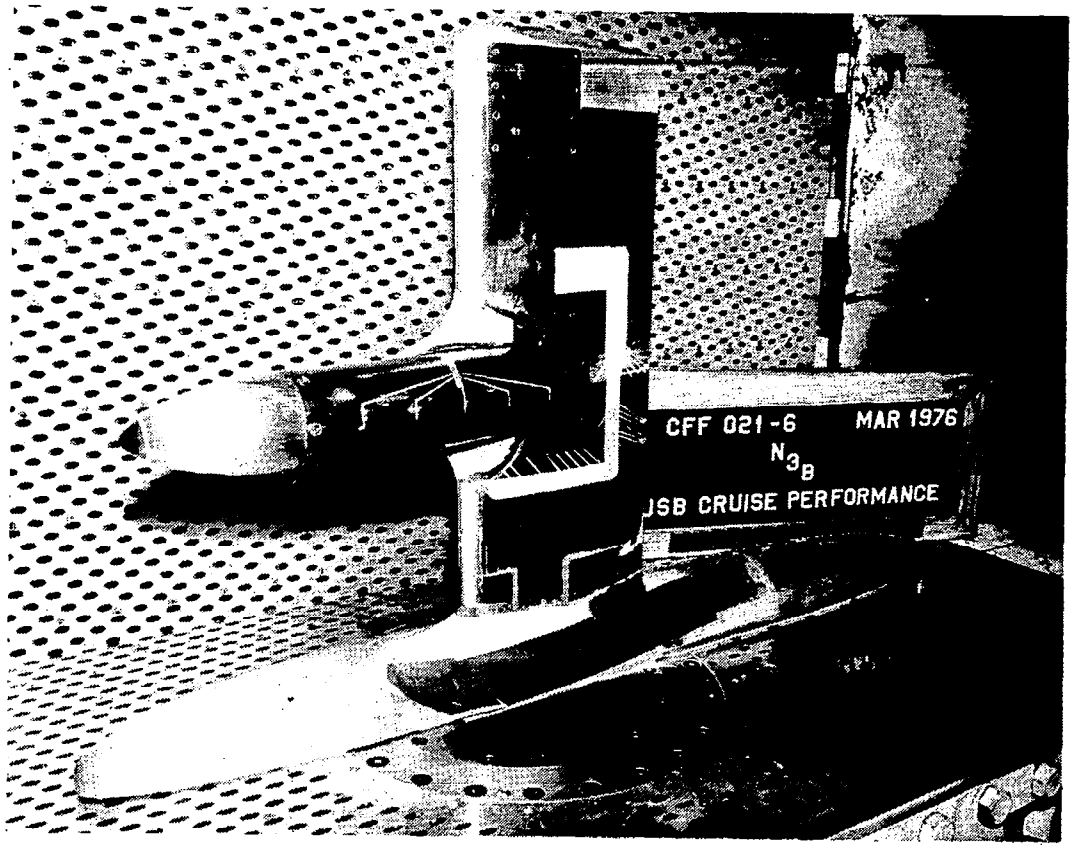


Figure 7. Three-dimensional force model mounted in CFF

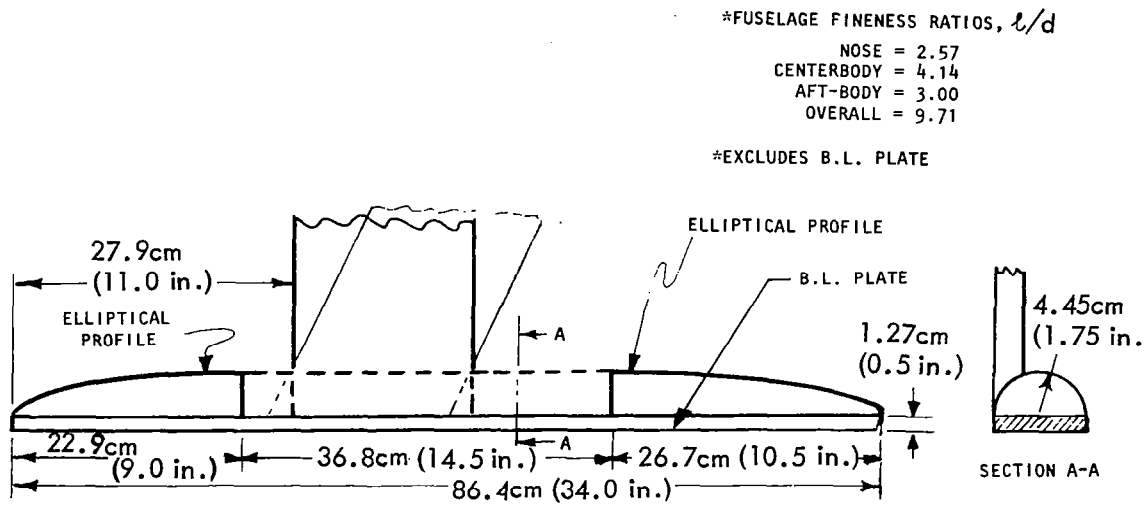


Figure 8. Force model fuselage with provision for mounting either straight wing or swept wing

USB CRUISE PROGRAM

| x/c | $z/c_u$ | $z/c_l$ |
|---|---|---|
| .00000 | .00000 | .00000 |
| .00241 | .00960 | -.01351 |
| .00961 | .02045 | -.02404 |
| .02153 | .03035 | -.03245 |
| .03806 | .03915 | -.03986 |
| .05904 | .04670 | -.04685 |
| .08427 | .05310 | -.05336 |
| .11349 | .05860 | -.05941 |
| .14645 | .06344 | -.06491 |
| .18280 | .06755 | -.06986 |
| .22221 | .07101 | -.07368 |
| .26430 | .07394 | -.07613 |
| .30866 | .07631 | -.07750 |
| .35486 | .07806 | -.07766 |
| .40245 | .07905 | -.07619 |
| .45099 | .07940 | -.07217 |
| .50000 | .07889 | -.06585 |
| .54901 | .07750 | -.05696 |
| .59755 | .07520 | -.04684 |
| .64514 | .07190 | -.03641 |
| .69134 | .06740 | -.02649 |
| .73570 | .06190 | -.01773 |
| .77779 | .05560 | -.01032 |
| .81720 | .04859 | -.00455 |
| .85355 | .04110 | -.00051 |
| .88651 | .03346 | .00189 |
| .91573 | .02600 | .00293 |
| .94096 | .01887 | .00295 |
| .96194 | .01274 | .00217 |
| .97847 | .00765 | .00124 |
| .99039 | .00395 | .00022 |
| .99759 | .00140 | -.00045 |
| 1.00000 | .00080 | -.00080 |

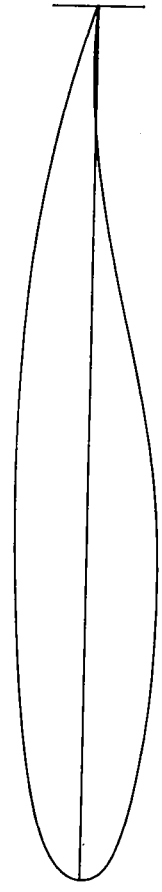

Figure 9. Straight wing airfoil ordinates and section layout

corresponding values for the straight wing. The streamwise section thickness was thereby reduced to 14.5 percent.

The straight wing planform is laid out in Figure 10. In the lower part of the figure, the fuselage half-body is depicted by the dashed lines in its normal position for 3-D testing. The removable tip shape and break-point are illustrated by dashed lines in the upper part of the figure. Locations for five rows of static pressure taps are also illustrated. Rows A, B, and C are positioned to obtain jet and nacelle interference effects, while row D is outside the interference region and row E is positioned to obtain fuselage interference. Figure 11 shows the chordwise positions for the pressure tubes in each of the designated rows.

The planform for the swept wing is laid out in Figure 12 so that the corresponding information shown for the straight wing in Figure 10 is presented. Distribution of pressure tube rows is distinctly different from that carried out on the straight wing due to the provision for a dual nacelle arrangement. Rows A and A' are situated along the nacelle exhaust centerlines, while rows B and C' are between the two nacelles and between the inboard nacelle and the fuselage. Row C is just outboard of the outer engine. Chordwise positions for the pressure taps are presented in Figure 13.

4.1.3 Model Component Summary - Before describing the design details of the nacelles and miscellaneous components, the program will be briefly scoped by presenting a summary of the hardware requirements. At the completion of model fabrication, a photograph (Figure 14) was made to include as nearly as possible the sum total of model components for the experimental program. The swept wing with D-duct nacelle, missing from the picture, is represented by a wooden replica made up for the smoke tunnel and is shown at the lower left. The variable camber flaps are just behind this model, and a number of the wing fillets are laid out to the right. Most of the components in the photograph are identifiable by sight. Some of those that may not be, however, are the numerous pylon spacers in the upper left-hand corner, which were used for matching the various nacelles with the basic, underslung pylon when testing at

USB CRUISE PROGRAM

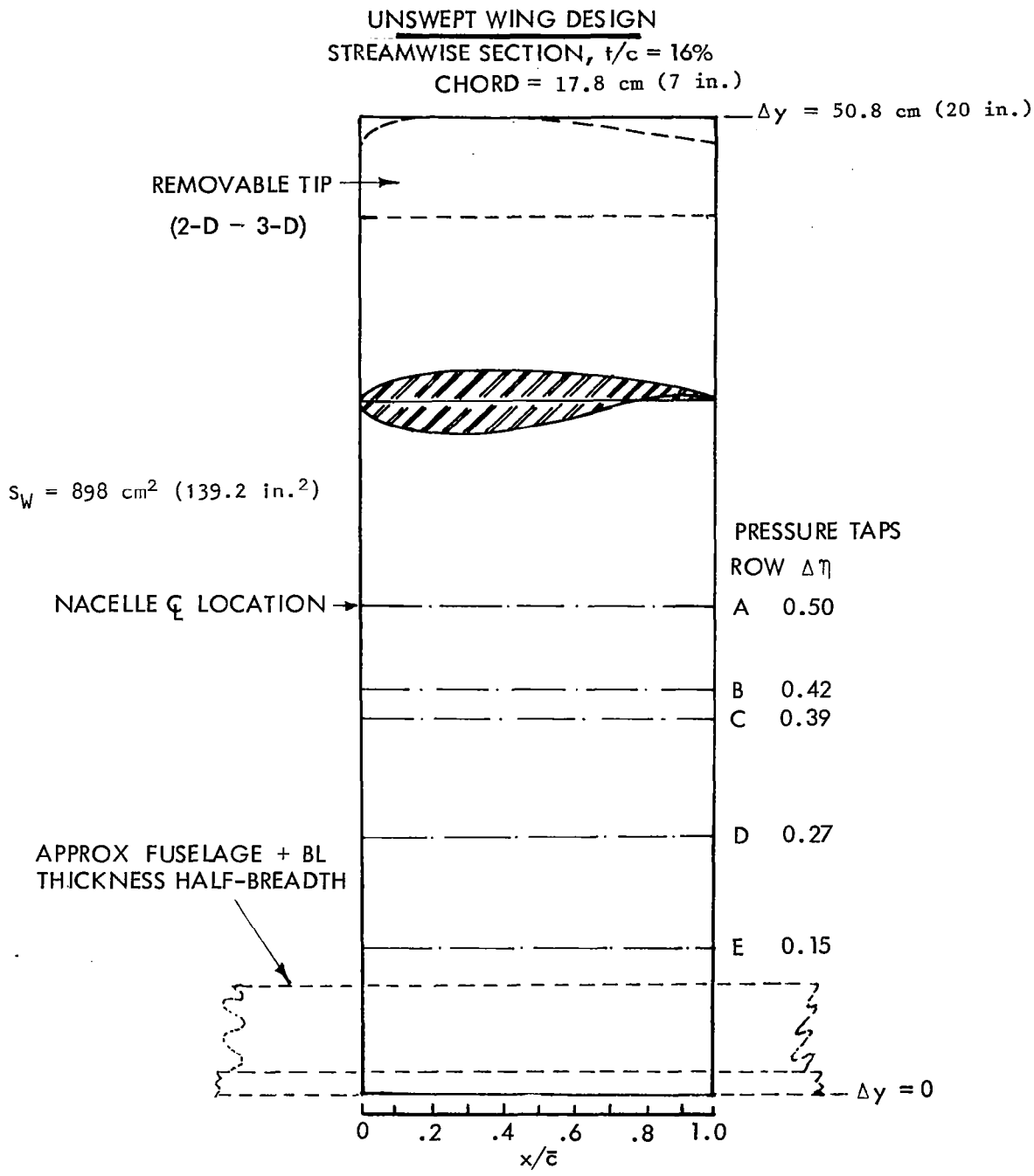


Figure 10. Straight wing planform and instrumentation layout

USB CRUISE PROGRAM

| ROW A | | ROW B | | ROW C | | ROWS D AND E | |
|---|---|---|---|---|---|---|---|
| UPPER | LOWER | UPPER | LOWER | UPPER | LOWER | UPPER | LOWER |
| 0.65 | -- | 0.01 | 0.025 | 0.01 | 0.05 | 0.01 | 0.05 |
| 0.70 | | 0.02 | 0.050 | 0.02 | 0.20 | 0.05 | 0.20 |
| 0.75 | | 0.05 | 0.10 | 0.05 | 0.40 | 0.10 | 0.40 |
| 0.80 | | 0.10 | 0.20 | 0.10 | 0.60 | 0.15 | 0.60 |
| 0.85 | | 0.15 | 0.30 | 0.15 | 0.80 | 0.20 | 0.80 |
| 0.90 | | 0.20 | 0.40 | 0.20 | | 0.30 | |
| 0.95 | | 0.25 | 0.50 | 0.30 | | 0.45 | |
| 1.00 | -- | 0.30 | 0.60 | 0.40 | | 0.55 | |
| | | 0.35 | 0.70 | 0.45 | | 0.60 | |
| | | 0.40 | 0.80 | 0.50 | | 0.70 | |
| | | 0.45 | 0.90 | 0.55 | | 0.80 | |
| | | 0.50 | | 0.60 | | 0.90 | |
| | | 0.55 | | 0.70 | | 1.00 | |
| | | 0.60 | | 0.80 | | | |
| | | 0.65 | | 0.90 | | | |
| | | 0.70 | | 0.95 | | | |
| | | 0.80 | | 1.00 | | | |
| | | 0.95 | | | | | |
| | | 1.00 | | | | | |

Figure 11. Chordwise pressure tube locations for straight wing measured in $x/\bar{c}$ from leading edge

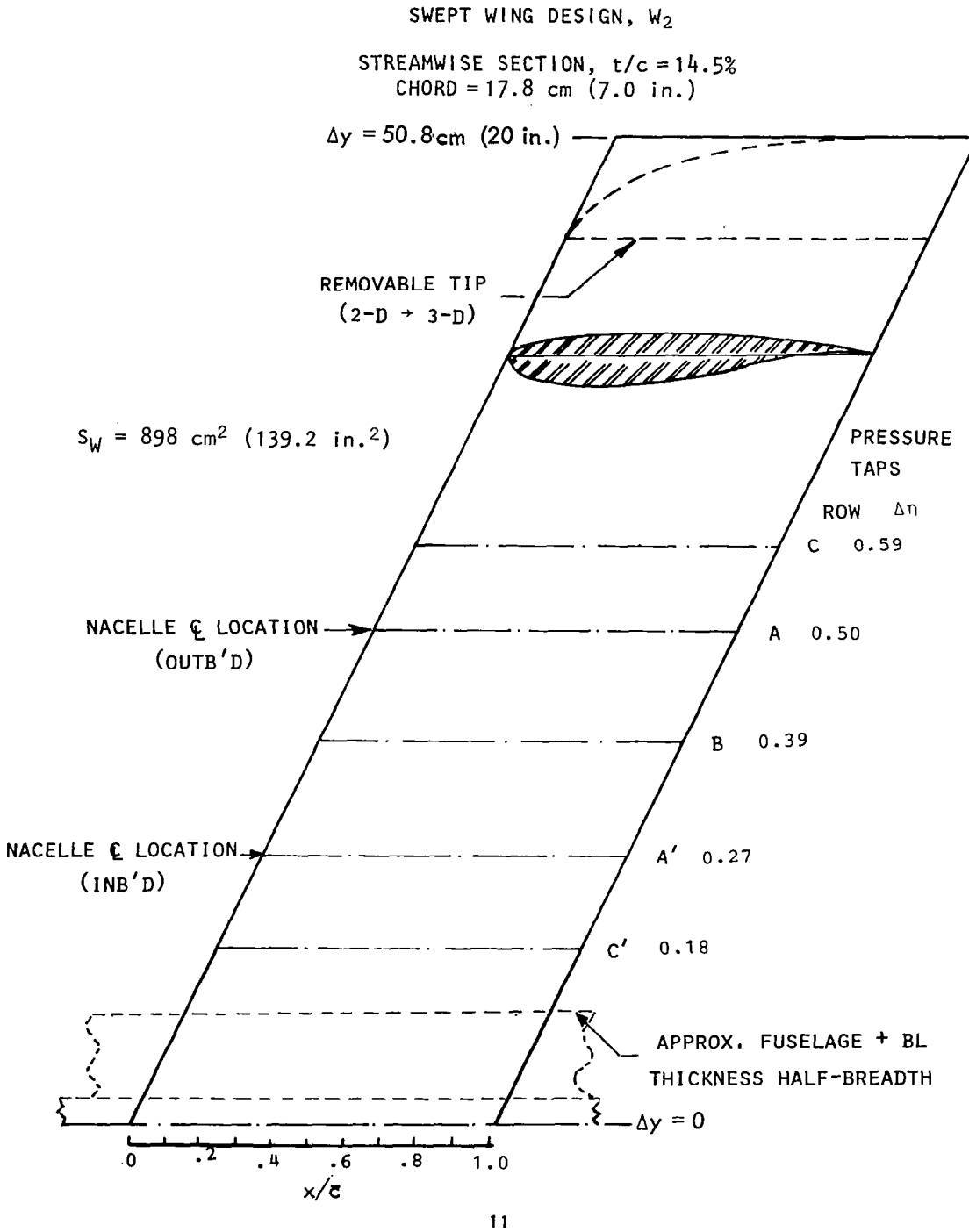


11

Figure 12. Swept wing planform and instrumentation layout

USB CRUISE PROGRAM

| ROWS A AND A' | | ROWS B AND B' | | ROWS C AND C' | |
|---|---|---|---|---|---|
| UPPER | LOWER | UPPER | LOWER | UPPER | LOWER |
| 0.65 | -- | 0.01 | 0.025 | 0.01 | 0.05 |
| 0.70 | | 0.02 | 0.05 | 0.02 | 0.20 |
| 0.75 | | 0.05 | 0.10 | 0.05 | 0.40 |
| 0.80 | | 0.10 | 0.20 | 0.10 | 0.60 |
| 0.85 | | 0.15 | 0.30 | 0.15 | 0.80 |
| 0.90 | | 0.20 | 0.40 | 0.20 | |
| 0.95 | | 0.25 | 0.50 | 0.30 | |
| 1.00 | | 0.30 | 0.60 | 0.40 | |
| | | 0.35 | 0.70 | 0.45 | |
| | | 0.40 | 0.80 | 0.50 | |
| | | 0.45 | 0.90 | 0.55 | |
| | | 0.50 | | 0.60 | |
| | | 0.55 | | 0.70 | |
| | | 0.60 | | 0.80 | |
| | | 0.65 | | 0.90 | |
| | | 0.70 | | 0.95 | |
| | | 0.80 | | 1.00 | |
| | | 0.90 | | | |
| | | 0.95 | | | |
| | | 1.00 | | | |

Figure 13. Chordwise pressure tube locations for swept wing measured in $x/\bar{c}$ from leading edge

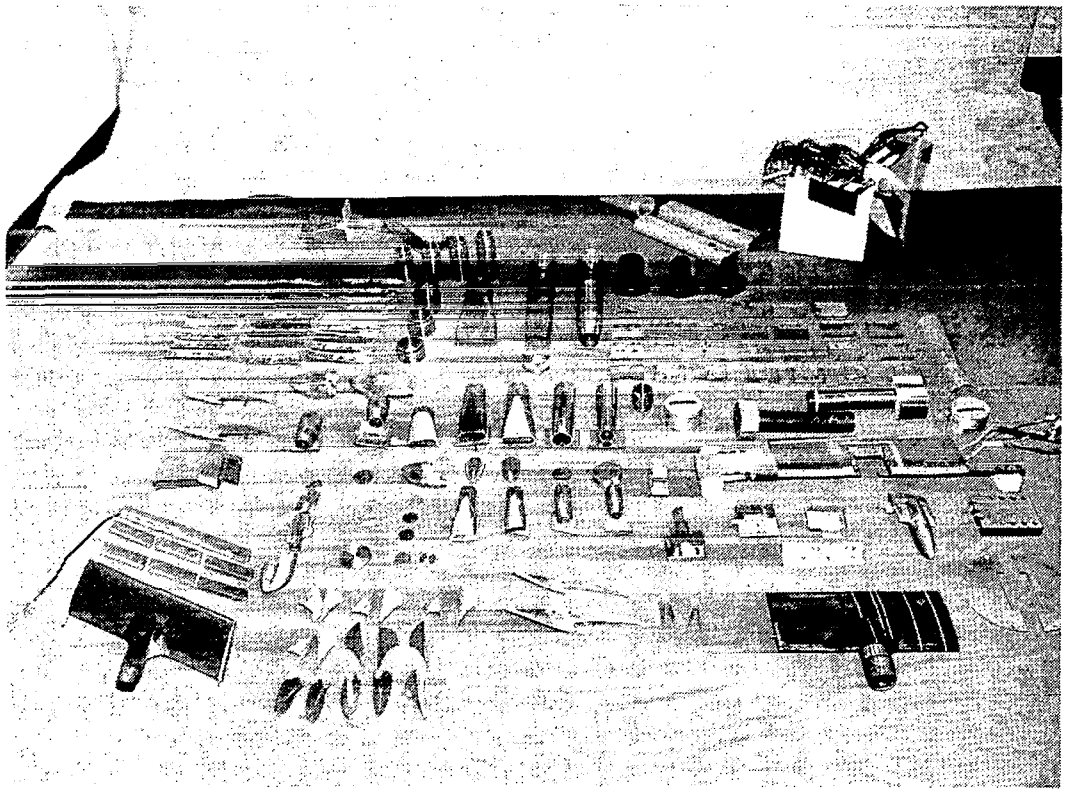

Figure 14. Model parts and associated test hardware

different chordwise discharge positions. The small, square plates in the upper right-hand part of the picture are the pads which mate various nozzles to the wing at the different chordwise positions described above. In the far background, from left to right, are the nozzle calibration rake and the traversing wake rake.

A table, shown in Figure 15, has been prepared to summarize the various model components, the number required, and the symbol designations. The symbol designations are used herein for defining configurations in run schedules, and plot labels. Where practical, the designations selected were the first letters of the component names. For instance, F is for fuselage, W for wing, P for pylon, C for cowl (forebody), and N for nozzle. Subscripted numbers identify different variations of a given configuration type.

4.1.4 Integrated Nacelles and Mounting Details - Basically two different kinds of integrated nacelles were tested in the high-speed experimental program; the long nacelles which accommodated nozzles with low boattail angles and short nacelles for which the afterbody boattail angles were considerably higher. In general, the short nacelle configurations are differentiated from the larger nacelles by the subscript letter, E. Figure 16 shows a long, intermediate nacelle as it would appear mounted on the straight wing. The internal flow paths and location of the choke plate are illustrated by dashed lines. For the sake of comparison, the short nacelle forebody is shown in the same figure. Both forebodies and pylon forward sections have identical contours.

In Figure 17, the same nozzle-wing assembly is illustrated, but a flow-through forebody has been substituted. A solid wooden pylon section ($P_{11}$) was fabricated to fair into the standard wing block ($B_4$). One of the more important purposes for this configuration was to provide a comparison with the faired-over forebody at flow-through pressure ratio to evaluate effects of inlet flow.

| COMPONENT TYPE | COMPONENT DESCRIPTION | NO. REQD. | NEW | EXISTING | DESIG-NATION |
|---|---|---|---|---|---|
| FUSELAGE | Nose | 1 | X | | $N_1$ |
| | Afterbody | 1 | X | | $A_1$ |
| | Center Section for High Existing Wing | 1 | X | | $F_1$ |
| | Center Section for High New Wing | 1 | X | | $F_2$ |
| WING | Straight Wing | 1 | | X | $W_1$ |
| | Swept Wing ($\Lambda = 25^o$) | 1 | X | | $W_2$ |
| | Straight Wing Tip Fairing | 1 | X | | $T_1$ |
| | Swept Wing Tip Fairing | 1 | X | | $T_2$ |
| | Instrumented T.E. for Swept Wing | 1 | X | | $E_1$ |
| | Segmented Flap for Swept Wing | 1 | X | | $S_1$ |
| | Straight Clean Wing Fairing Block | 1 | | X | $B_1$ |
| | Swept Clean Wing Fairing Blocks | 2 | X | | $B_2, B_3$ |
| | Straight Wing Nozzle Mounting Block | 1 | | X | $B_4$ |
| | Swept Wing Nozzle Mounting Blocks | 3 | X | | $B_5, B_6, B_7$ |
| PYLON | Straight Wing Short Pylon for Pipe Nacelles | 1 | X | | $P_1$ |
| | Straight Wing Long Pylon for Pipe Nacelles | 2 | X | | $P_2, P_3$ |
| | Swept Wing Short Pylon for Pipe Nacelles | 1 | X | | $P_4$ |
| | Swept Wing Long Pylon for Pipe Nacelles | 2 | X | | $P_5, P_6$ |
| | Straight Wing Short Pylon for Faired Nacelles | 1 | | X | $P_7$ |
| | Straight Wing Long Pylon for Faired Nacelles | 1 | X | | $P_8$ |
| | Swept Wing Long Pylon for Faired Nacelles | 2 | X | | $P_9, P_{10}$ |
| | Straight Wing Pylon for Flo-Thru Nacelles | 1 | X | | $P_{11}$ |
| | Straight Wing Long Pylon for Streamline Nacelles | 1 | X | | $P_{12}$ |
| | Swept Wing Long Pylon for Streamline Nacelles | 1 | X | | $P_{13}$ |
| | Straight Wing Pylon for Integr. Pipe Nacelles | 1 | X | | $P_{14}$ |
| | Swept Wing Pylon for Integr. Pipe Nacelles | 1 | X | | $P_{15}$ |
| NACELLE | Short Faired Forebody for Straight Wing | 1 | | X | $C_1$ |
| | Long Faired Forebody for Straight Wing | 1 | X | | $C_2$ |
| | Long Faired Forebody for Swept Wing | 2 | X | | $C_3, C_4$ |
| | Flow-Thru Forebody for Straight Wing | 1 | X | | $C_5$ |
| | Streamline Forebody for Straight Wing | 1 | X | | $C_6$ |
| | Streamline Forebody for Swept Wing | 1 | X | | $C_7$ |
| | Upstream Pipe Forebody for Large Nacelle | 1 | X | | $C_8$ |
| | Upstream Pipe Forebody for Intermediate Nacelle | 1 | X | | $C_9$ |
| NOZZLE | Large D-Duct Nozzle Pipe Mounted | 1 | X | | $N_1$ |
| | Intermediate Long Circular Nozzle, Wing & Pipe Mounted | 1 | X | | $N_2$ |
| | Intermediate Long D-Duct Nozzle, Wing & Pipe Mounted | 1 | X | | $N_3$ |
| | Intermediate Long High AR Nozzle, Wing & Pipe Mounted | 1 | X | | $N_4$ |
| | Intermediate Very High AR Nozzle, Wing & Pipe Mounted | 1 | X | | $N_5$ |
| | Small Streamline Nacelle Nozzle, Straight Wing | 1 | X | | $N_6$ |
| | Small Streamline Nacelle Nozzle, Swept Wing | 1 | X | | $N_7$ |

Figure 15. Summary of model and test hardware components (Sheet 1)

| COMPONENT TYPE | COMPONENT DESCRIPTION | NO. REQD. | NEW | EXISTING | DESIG-NATION |
|---|---|---|---|---|---|
| NOZZLE (cont'd) | Small D-Duct Nacelle Nozzle, Swept Wing | 2 | X | | $N_8^1$ & $N_8^2$ |
| | Large Circular Nozzle, Pipe Mounted | 1 | X | | $N_9$ |
| | Large Very High AR Nozzle, Pipe Mounted | 1 | X | | $N_{10}$ |
| | Small Circular Nozzle, Swept Wing | 1 | X | | $N_{11}$ |
| | Small High AR Nozzle, Swept Wing | 1 | X | | $N_{12}$ |
| | Small Very High AR Nozzle, Swept Wing | 1 | X | | $N_{13}$ |
| | Intermediate Short Circular Nozzle, Discharge at 20% C | 1 | | X | $N_{1_E}$ |
| | Intermediate Short Circular Nozzle, Discharge at 35% C | 1 | | X | $N_{2_E}$ |
| | Intermediate Short D-Duct Nozzle, Discharge at 35% C | 1 | | X | $N_{3_E}$ |
| | Intermediate Short High AR Nozzle, Discharge at 35% C | 1 | | X | $N_{4_E}$ |
| | Intermediate Long D-Duct Nozzle Extension | 3 | X | | $X_1, X_2, X_3$ |
| | Intermediate Long Circular Nozzle Flow Deflector | 1 | X | | $D_1$ |
| | Large Spacers to Position Pipe Nozzles | 3 | X | | $L_1, L_2, L_3$ |
| | Intermediate Spacers to Position Pipe Nozzles | 3 | X | | $L_4, L_5, L_6$ |
| | Transition Adapter for Pipe Area Change | 1 | X | | $L_7$ |
| | Constant Area Adapter for Pipe Nozzle | 1 | X | | $L_8$ |
| | Choke Plates for Small Nozzles | 2 | X | | $K_5, K_6$ |
| | Choke Plate for Intermediate Nozzles | 1 | | X | $K_7$ |
| | Choke Plate for Large Nozzles | 1 | X | | $K_8$ |
| INSTRUMENTATION | 3 Rows Additional Pressure Taps, Straight Wing | 30 | X | | $R_1, R_2, R_3$ |
| | 3 Rows Basic Pressure Taps, Straight Wing | 61 | | X | $R_4, R_5, R_6$ |
| | 6 Rows Pressure Taps, Swept Wing | 91 | X | | $R_7 - R_{12}$ |
| | Nozzle Afterbody Pressure Taps (5/Nozzle) | 20 | | X | $R_{13} - R_{16}$ |
| | Nozzle Afterbody Pressure Taps (5/Nozzle) | 70 | X | | $R_{17} - R_{30}$ |
| | Duct Plenum Pressure Taps (1/Wing Block) | 1 | | X | $pt_1$ |
| | Duct Plenum Pressure Taps (1/Wing Block) | 2 | X | | $pt_2, pt_3$ |
| | 57 Tube Calibration Rake for All Nozzles | 1 | X | | $Q_1$ |
| | 214 Tube Wake Rake for Drag Measurements | 2 | X | | $J_1$ |
| | Orifice Pressure Taps for Flow Measurements | 3 | | X | $pt_4, pt_5$ |
| TEST HARDWARE | Double Wall Upstream Pipe for Large Nozzles | 1 | X | | $Z_1$ |
| | Motor Driven Traverse for Wake Rakes | 1 | X | | $Y_1$ |
| | Wall Fitting for Straight & Swept Wings, Upper End | 1 | X | | $V_1, V_2$ |
| | Straight & Swept Wing-to-Floor Balance Adapters | 1 | X | | $ba_1, ba_2$ |
| | Floor Porosity Disc for Both Wings | 1 | X | | $pd_1$ |
| | Basic Wall Plates for Straight Wing | 2 | | X | $wp_1, wp_2$ |
| | Basic Wall Plates for Swept Wing | 2 | X | | $wp_3, wp_4$ |
| | Orifice Assembly & Air Supply Piping | 1 | | X | $as_1$ |
| | Orifice Plate for Intermediate & Small Nozzles | 1 | | X | $O_1$ |
| | Orifice Plate for Large Nozzles | 1 | X | | $O_2$ |

Figure 15. Summary of model and test hardware components (Sheet 2)

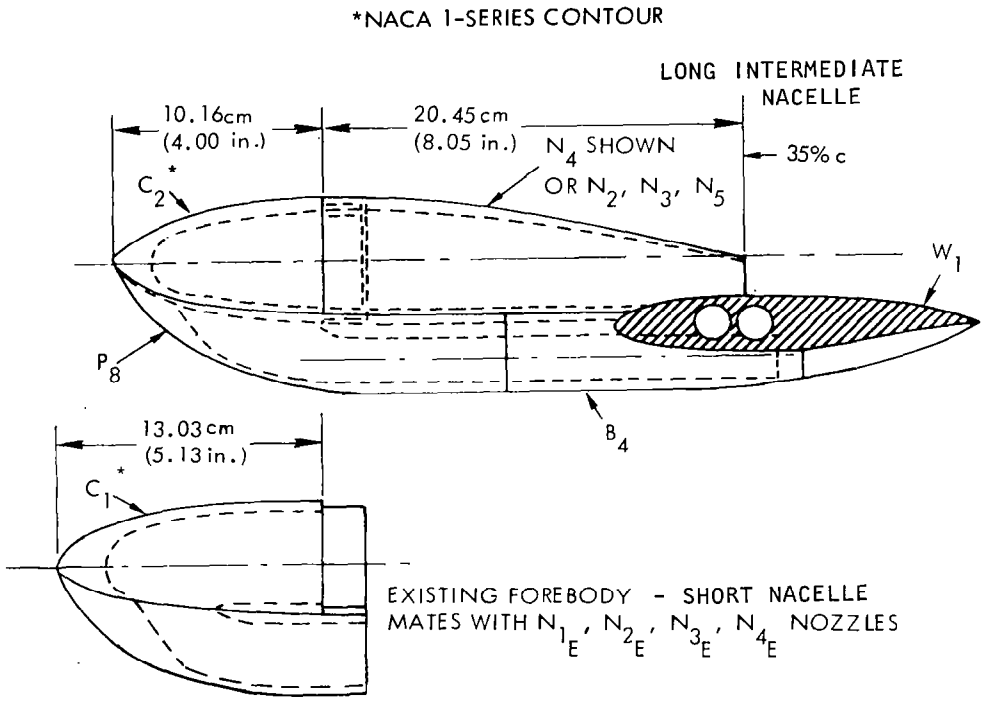


Figure 16. Nacelle general arrangement for straight wing

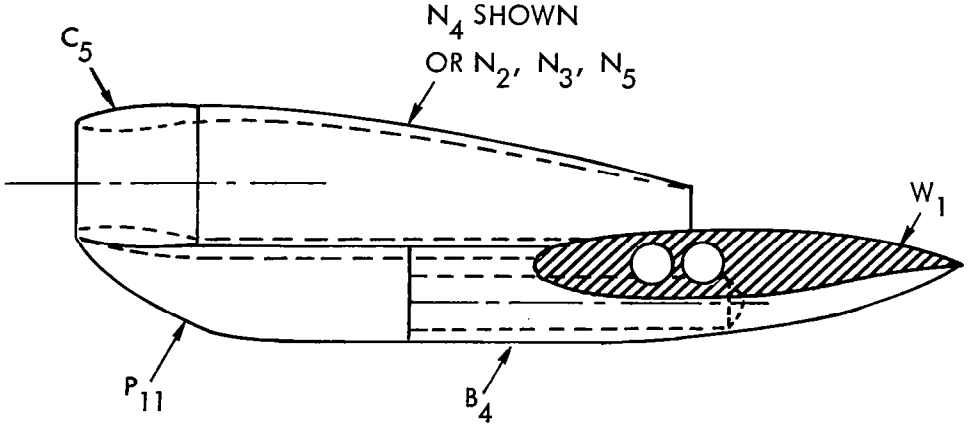


Figure 17. Flow-through nacelle mounted on straight wing

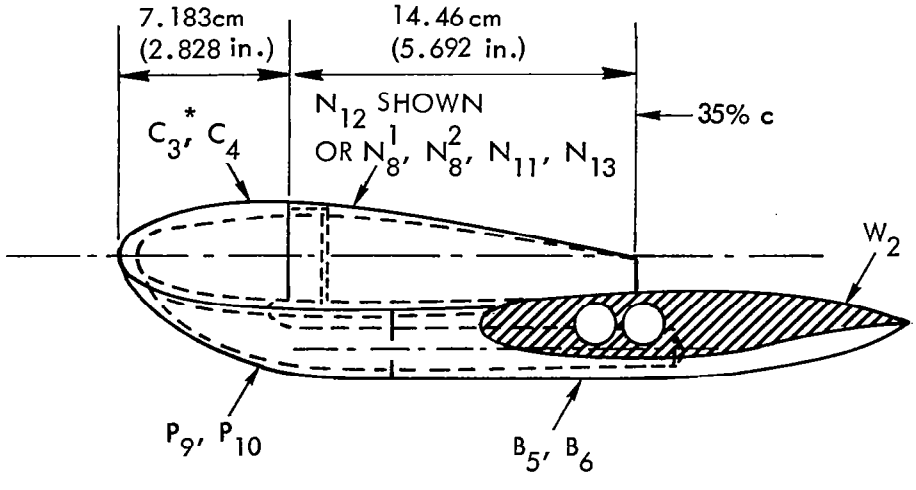


*NACA 1-SERIES CONTOUR

Figure 18. Nacelle general arrangement for swept wing

A typical swept-wing nacelle installation is illustrated in Figure 18. It is basically a scaled-down version of the long nacelle installation for the straight wing shown in Figure 16. The size of the nozzle exit area is only half that of the straight-wing installation, however, so that the dual engine installation on the swept wing has the same thrust as that of the single engine installation on the straight wing.

Upstream pipe nacelles were designed in two sizes: an intermediate-size nozzle equal to that of the standard straight wing configuration, and a large nozzle which was twice the standard size. These two nacelle types are illustrated in Figure 19. For the large nacelle, forebody contouring at the pipe/nacelle juncture is required, while the small nacelle is essentially the same diameter as the pipe. Just ahead of the forebody mating juncture, one-inch slots are distributed around the pipe circumference for boundary layer removal. Tunnel operating conditions provide a natural aspiration of this system for exhausting to the atmosphere. With the slots providing approximately 50% porosity, not all the boundary layer is removed, although the lowest energy portion of it is effectively eliminated. Forebody spacers, designated by "L" numbers as shown in the figure, provide for the adjustment of nozzle discharge position to various desired chordwise locations.

4.1.5 Nozzle Design Details - The design of a typical USB test nozzle is illustrated in Figure 20. Here is shown nozzle $N_4$, an intermediate long nozzle with an aspect ratio of 4. All nozzles, except for streamline nozzle $N_6$, are circular in cross-section where they join the nacelle forebody. Moving aft from this point, the transition is gradually made to the desired nozzle exit shape. In the cases of all higher aspect ratio nozzles, their upper, outer corners are rounded by quarter-circles whose radii are exactly equal to the nozzle height. Nozzle aspect ratios which are quoted, however, are based on equivalent rectangular widths (i.e., nozzle widths) which, when multiplied by nozzle heights, will give actual nozzle areas. To provide for separating the effects of internal roof angle from external boattail angle, a section with constant flow area was incorporated into the nozzle exit. (This applied to all nozzles except those with an "E" designation in the subscript.)

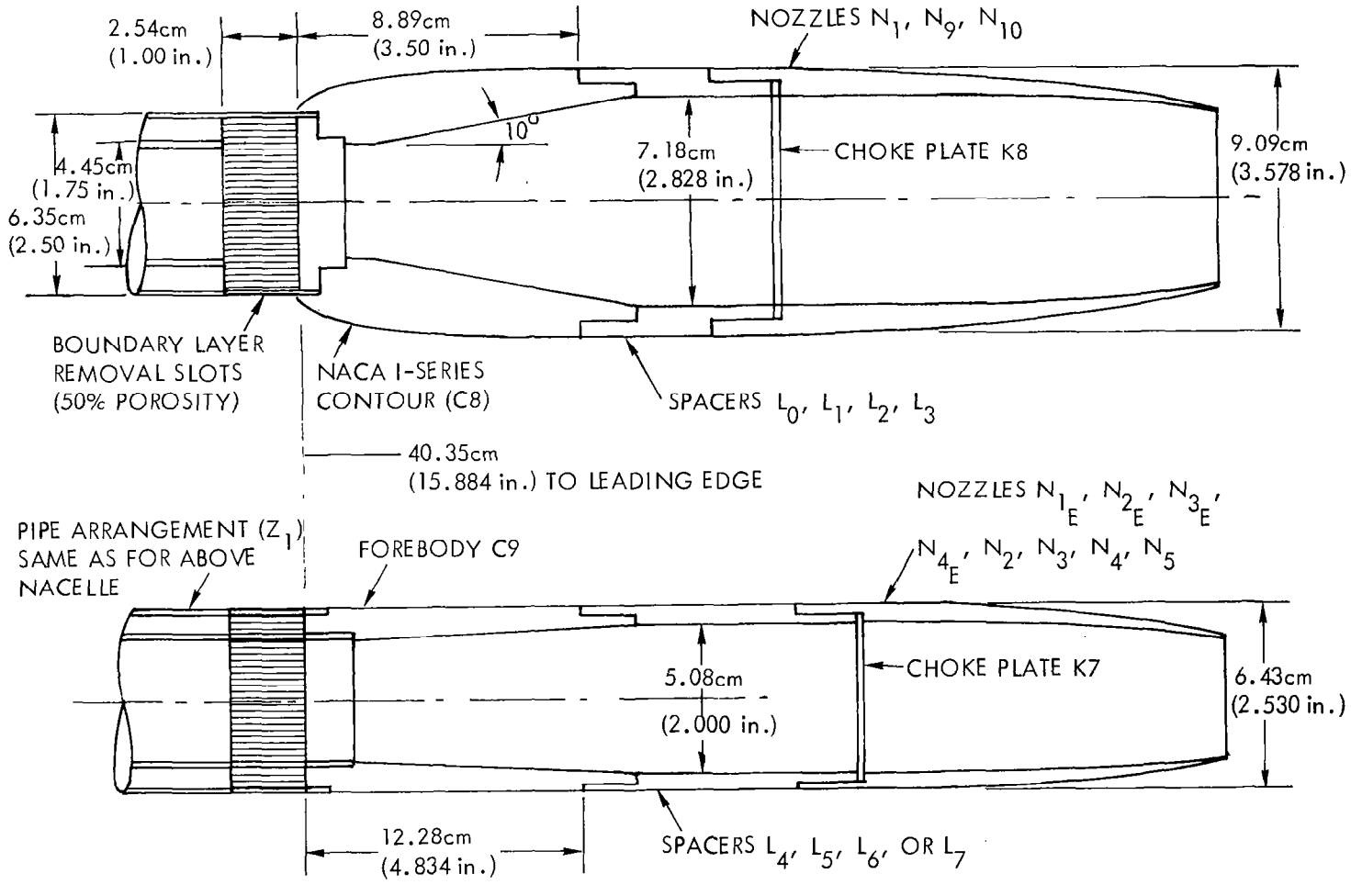


Figure 19. Upstream pipe nacelle details

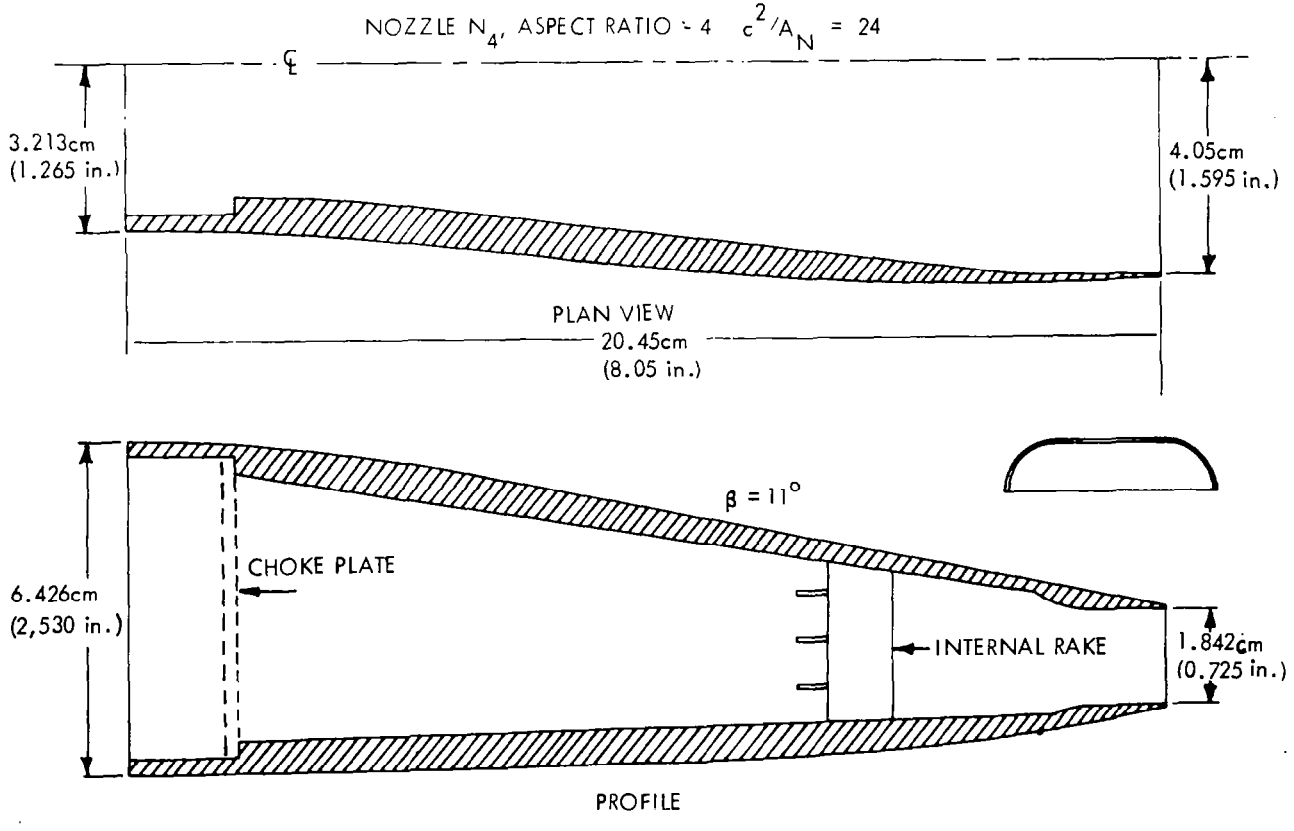


Figure 20. Typical nozzle design

In all cases, these sections were preceded by generous radii contours to promote the smoothest possible flow profiles. The length of each section was set at one-half the nozzle hydraulic diameter.

The design philosophy associated with developing the nozzle configurations emphasized minimizing the boattail angles. With the fixed vertical position of the nacelle forebody, boattails angles increased prohibitively with exit width-to-height ratio when using a simple, circular-arc profile. To circumvent this problem, a combination of circular arcs and straight lines were used to generate the nozzle external contours. Typically, the maximum boattail angle was reduced from $18^{\circ}$ to $12.5^{\circ}$ for the large, high aspect ratio (6.0) nozzle ($N_5$ or $N_{10}$)with this approach. To generate the contour, a circular arc was used to transition from the nacelle maximum diameter to the desired afterbody boattail angle, which was then held constant to the nozzle discharge station. An additional design constraint was to maintain an arc radius-to-nacelle diameter ratio of at least 5.0 when making the circular-arc transition. This procedure not only reduced the boattail angle, but placed the critical flow turning process well ahead of the wing-jet interference region. Since the circular nozzles had inherently low boattail angles, simple circular-arc profiles were used in generating afterbody contours for these designs. Other exceptions to the use of this approach were the four "E" (superscript) nozzles, which had simple circular-arc afterbodies.

An eyebrow-type deflector was designed for the D-duct nozzle $N_3$. It was simply a sheet-metal shroud which fitted over the nozzle exit and whose purpose was to provide an effective jet deflection angle of $15^{\circ}$ (downward) at the nozzle exit.

Three total pressure probes were mounted inside the nozzles as shown to provide reference total pressures. (The "E" nozzles used only one probe.) These reference pressures were calibrated against integrated nozzle exit total pressures obtained from an area weighted rake and then used to set test pressure ratios.

Key dimensions for all the test nozzles are presented in the table of Figure 21. Four primary variables were used to establish the matrix of test nozzles. These were relative size, aspect ratio, discharge location, and boattail angle. Relative size was expressed by the parameter $c^2/A_N$, which relates the square of the wing chord to the nozzle area. Three relative sizes, 12, 24 and 48, were included in the program. Nozzle aspect ratios varied from 1.25 (circular) to 6.0. Chordwise discharge positions varied from 10 to 50 percent, with 35% being the baseline value. For the nozzles designed with the combination circular-arc, straight-line contours, boattail angles ranged from 6 to 13 degrees. Boattail angles for the "E" nozzles, however, ranged from 16 to 36 degrees. The wings to which each of the nozzles is matched and the applicable mounting arrangements are also presented in the table.

Each of the nozzles were instrumented with static pressure tubes along their upper, outer centerlines. Locations of these surface orifices are provided in Figure 22. Existing "E" nozzles had six tubes, while the long nozzles had only five. In both cases, the distributions were essentially linear except as dictated by hardware design constraints.

4.1.6 Streamlined Nacelle Design Details - Although the streamlined nacelle is a special case of an integrated nacelle, a different design approach was used. The streamline nacelle shown in Figure 23 was developed for the straight wing operating at a cruise angle-of-attack of 2.6 degrees. Using the nozzle location of 35% chord as a reference point, a streamtube, the shape of the D-duct nozzle, was traced forward to a point well in front of the wing. A circular streamtube with cross-sectional area equal to that desired for the nacelle was then superimposed on the centroid of the D-duct and traced aft to the starting point.

The nacelle length was selected to give the forebody a reasonable fineness ratio while holding the afterbody boattail angle to around 12 degrees. (The boattail angle is actually only about $6^o$ relative to the freestream flow.) The forebody was developed around the centroid of the

## USB CRUISE PROGRAM

| GEOMETRIC | | RELATIVE SIZE | ASPECT RATIO | DISCHARGE LOCATION | BOATTAIL ANGLE | NOZZLE LENGTH | | MAXIMUM DIAMETER | | NOZZLE AREA | | WINGS | | MOUNTING | |
|---|---|---|---|---|---|---|---|---|---|---|---|---|---|---|---|
| NO. | NOZZLE DESCRIPTION / PARAMETER | $c^2/A_N$ | AR | x/ℓ | β~ DEG | cm | (in) | cm | (in) | $cm^2$ | $(in^2)$ | STRAIT | SWEPT | PIPE | WING |
| $N_1$ | LARGE D-DUCT, LONG | 12 | 2.5 | 0.1 - 0.5 | 9.0 | 28.915 | 11.384 | 9.088 | 3.578 | 26.923 | 4.173 | X | | X | |
| $N_2$ | INTERMED. CIRCL., LONG | 24 | 1.25 | 0.35 | 5.90 | 20.447 | 8.050 | 6.426 | 2.530 | 13.464 | 2.087 | X | X | X | X |
| $N_3$ | INTERMED. D-DUCT, LONG | 24 | 2.5 | 0.35 | 9.0 | 20.447 | 8.050 | 6.426 | 2.530 | 12.935 | 2.005 | X | | X | X |
| $N_4$ | INTERMED. HIGH AR, LONG | 24 | 4.0Δ | 0.35 | 11.0 | 20.447 | 8.050 | 6.426 | 2.530 | 13.464 | 2.087 | X | | X | X |
| $N_5$ | INTERMED. VERY HI-AR, LONG | 24 | 6.0Δ | 0.35 | 12.5 | 20.447 | 8.050 | 6.426 | 2.530 | 13.464 | 2.087 | X | | X | X |
| $N_6$ | SM. STRMLIN. D-DUCT, LONG | 48 | 2.5 | 0.35 | 9.00* | 14.458 | 5.692 | 4.544* | 1.789* | 6.729 | 1.043 | X | | | X |
| $N_8^1$ | SM. INBD. D-DUCT, LONG | 48 | 2.5 | 0.20 | 9.50 | 11.791 | 4.642 | 4.544 | 1.789 | 6.729 | 1.043 | | X | | X |
| $N_8^2$ | SM. OUTBD. D-DUCT, LONG | 48 | 2.5 | 0.20 | 9.50 | 11.791 | 4.642 | 4.544 | 1.789 | 6.729 | 1.043 | | X | | X |
| $N_9$ | LARGE CIRCULAR, SHORT | 12 | 1.25 | 0.1 - 0.5 | 12.00 | 28.915 | 11.384 | 9.088 | 3.578 | 26.923 | 4.173 | X | X | X | |
| $N_{10}$ | LARGE VERY HI-AR, LONG | 12 | 6.0Δ | 0.1 - 0.5 | 12.50 | 28.915 | 11.384 | 9.088 | 3.578 | 26.923 | 4.173 | X | | X | |
| $N_{11}$ | SMALL CIRCL., SHORT | 48 | 1.25 | 0.10 | 12.00 | 10.013 | 3.942 | 4.544 | 1.789 | 6.729 | 1.043 | | X | | X |
| $N_{12}$ | SMALL HI-AR, LONG | 48 | 4.0 | 0.35 | 11.00 | 14.458 | 5.692 | 4.544 | 1.789 | 6.729 | 1.043 | | X | | X |
| $N_{13}$ | SMALL VERY HI-AR, LONG | 48 | 6.0 | 0.50 | 11.00 | 17.125 | 6.742 | 4.544 | 1.789 | 6.729 | 1.043 | | X | | X |
| $N_{1E}$ | INTERMED. CIRCL., SHORT | 24 | 1.25 | 0.20 | 16.78 | 9.629 | 3.791 | 6.426 | 2.530 | 12.813 | 1.986 | X | | | X |
| $N_{2E}$ | INTERMED. CIRCL., SHORT | 24 | 1.25 | 0.35 | 16.78 | 12.296 | 4.841 | 6.426 | 2.530 | 12.813 | 1.986 | X | | | X |
| $N_{3E}$ | INTERMED. D-DUCT, SHORT | 24 | 2.5 | 0.35 | 24.52 | 12.296 | 4.841 | 6.426 | 2.530 | 13.464 | 2.087 | X | | | X |
| $N_{4E}$ | INTERMED. HI-AR, SHORT | 24 | 4.0Δ | 0.35 | 35.88 | 12.296 | 4.841 | 6.426 | 2.530 | 13.464 | 2.087 | X | | | X |

Δ THESE ASPECT RATIOS ARE EXPRESSED FOR EQUIVALENT RECTANGULAR NOZZLE CROSSECTIONS

* APPROXIMATELY EQUIVALENT DIMENSIONS FOR NON-CIRCULAR, NON-SYMMETRIC NACELLES

Figure 21. Key dimensions for nozzles in test matrix

USB CRUISE PROGRAM

| NEW NOZZLES, x/l | EXISTING NOZZLES, x/l |
|---|---|
| 0.186 | 0.369 |
| 0.353 | 0.479 |
| 0.559 | 0.582 |
| 0.745 | 0.699 |
| 0.932 | 0.807 |
| - | 0.903 |

NOTES: (1) x IS DISTANCE MEASURED AFT FROM NACELLE JOINT.

(2) l IS NOZZLE LENGTH.

(3) EXISTING NOZZLES ARE DESIGNATED WITH "E" SUBSCRIPTS.

Figure 22. Nozzle pressure tube locations along nacelle upper surface

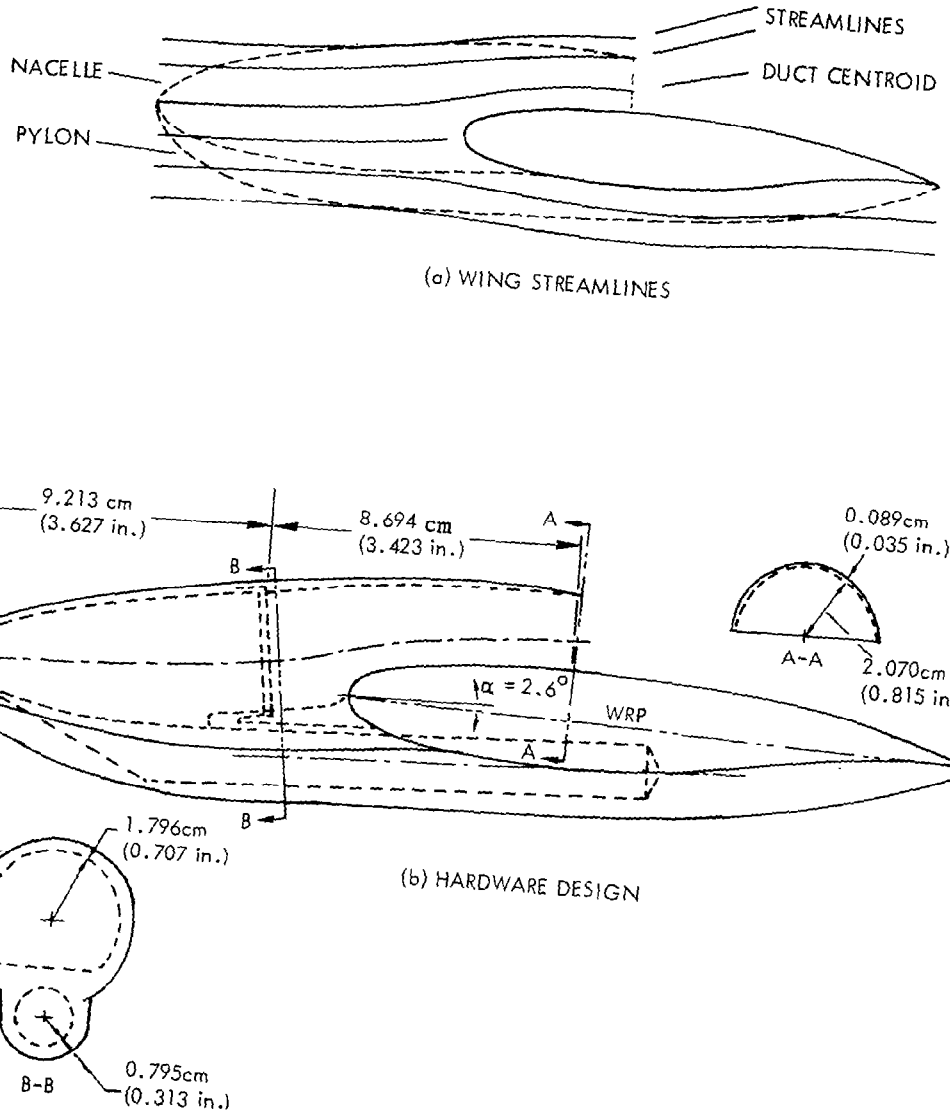


Figure 23. Cruise design for a streamlined USB nacelle on a straight wing

D-duct using NACA 1-series coordinates developed to the radii of the initial circular streamtube. The afterbody transition section was faired between the outer boundaries of the circular and D-duct streamtubes. The pylon was begun with a NACA 1-series fairing which transitioned into a semi-circular cross-section at maximum height. Because of the droop of the forward part of the nacelle, the pylon height was considerably less than for the other configurations (i.e., nonstreamlined). The choke plate section could not be maintained in a circular shape due to interference with the air supply duct. Section B-B of Figure 23 shows the shape of the internal duct section near the choke plate. The modified choke plate was designed with the same flow area as those used with the standard nozzles having the same discharge area.

4.1.7 Pylon-Mounted Nacelle Details - As used here, the term "pylon-mounted nacelles" refers to those nacelles mounted above the wing at a sufficient height so that no portion of the exhaust efflux scrubs the wing surface. Figures 24 and 25 are sketches of the upper-surface pylons used in conjunction with pylon-mounted circular nacelles on the swept wing. Figure 24 shows the nacelle positioned at one-half nozzle width (surface-to-surface) above the wing, while Figure 25 shows the nacelle located at one nozzle height, the maximum height planned for the initial tests. The shaping of the pylon followed from the application of general streamlining techniques. The camber line for the pylon/wing junction was developed with a thick (viscous), infinitely-swept wing program. The use of this program is justified on the basis of the "flatness" of the finite-wing span-loading as indicated by results from a vortex-lattice program. The camber was decreased in a vertical direction in proportion to $1/(\text{height/chord})^2$ to define camber at the nacelle/pylon juncture. A 6-percent section thickness form was then wrapped around the two camber lines with a linear variation in pylon-section shape between the two juncture-stations. Straight-wing pylon designs were designed with the same section thickness form, but without camber; the vertical planform (or side view) is essentially the same as that shown for the swept-wing pylons. A typical pylon-mounted nacelle installation, mounted in the tunnel, is shown in Figure 26.

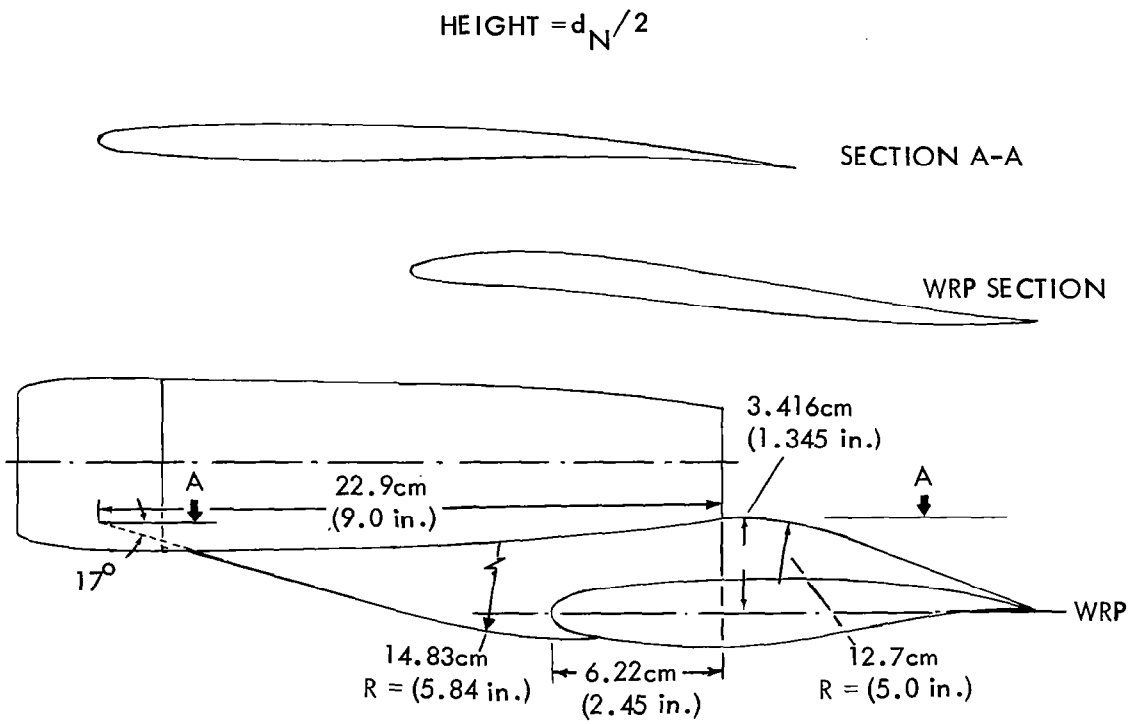


Figure 24. Short pylon mounted circular nozzle on swept wing

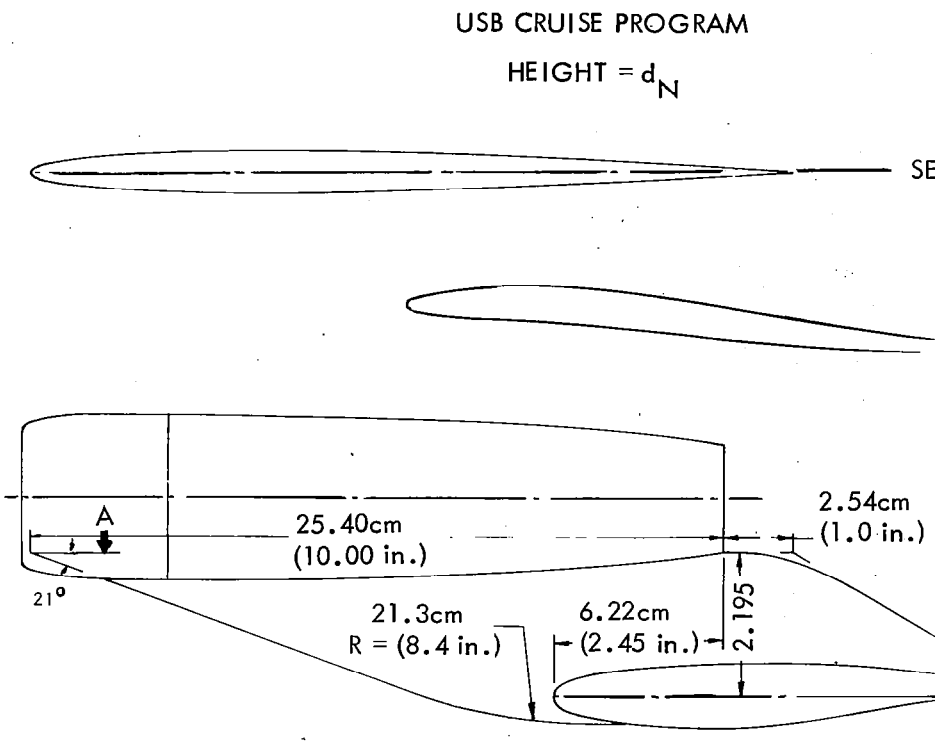


Figure 25. Long pylon mounted circular nozzle on swept w


Figure 26. Pylon mounted flow-through nacelle on swept wing in wind tunnel

4.1.8 Variable Camber Design Details - The variable-camber features, as incorporated into the $25^{\circ}$ swept wing, are shown in Figure 27. A breakpoint was incorporated into the wing at 80% chord so that various trailing edges could be substituted as desired. In addition to the basic airfoil trailing-edge angle, flaps were fabricated for $\pm 5^{\circ}$ incremental variations. This angle variation was selected from studies of potential wing spanloadings with an attached, vectored jet. Each of the flaps was divided into three sections so that the camber could be changed directly behind the nacelle, or nacelles,and so that wing geometric twist could be incorporated effectively if desired.

4.1.9 Wing Fillet Design - To smooth out the intersections between the nacelle and wing, and between wing and fuselage, a set of fillet shapes were developed. The use of fillets represented an attempt to aerodynamically blend the various nacelle contours with the wing on an equal basis. The cruise performance changes would then largely reflect basic geometric differences in nozzle designs. The following discussion applies primarily to the swept-wing fillet design approach, as this presents the more difficult contouring problem.

There are two aerodynamic effects to be considered in the design of a fillet for a particular airfoil-body juncture. First, the wing section shape must be modified to account for the wing reflection in the body or nacelle. This was done by considering the wing to be "kinked" at the body or nacelle centerline. Second, the wing crest suction pressures should be reduced to allow for body overpressures. In the wing-fuselage reflection, the "kink" effect causes the leading-edge suction peak to reduce and the suction level aft of the crest to increase. Therefore, the design philosophy for the root section was to produce an airfoil with a higher suction peak than that of the basic section, followed by a reduced crest pressure level. Basically the same philosophy applied to the outboard side of the nacelle wing intersections.

The reflection on the inboard side of the nacelle produces an effect opposite to that just discussed, in that the suction peak of the leading-edge is higher than that of the clean wing, while the pressure peaks on the aft

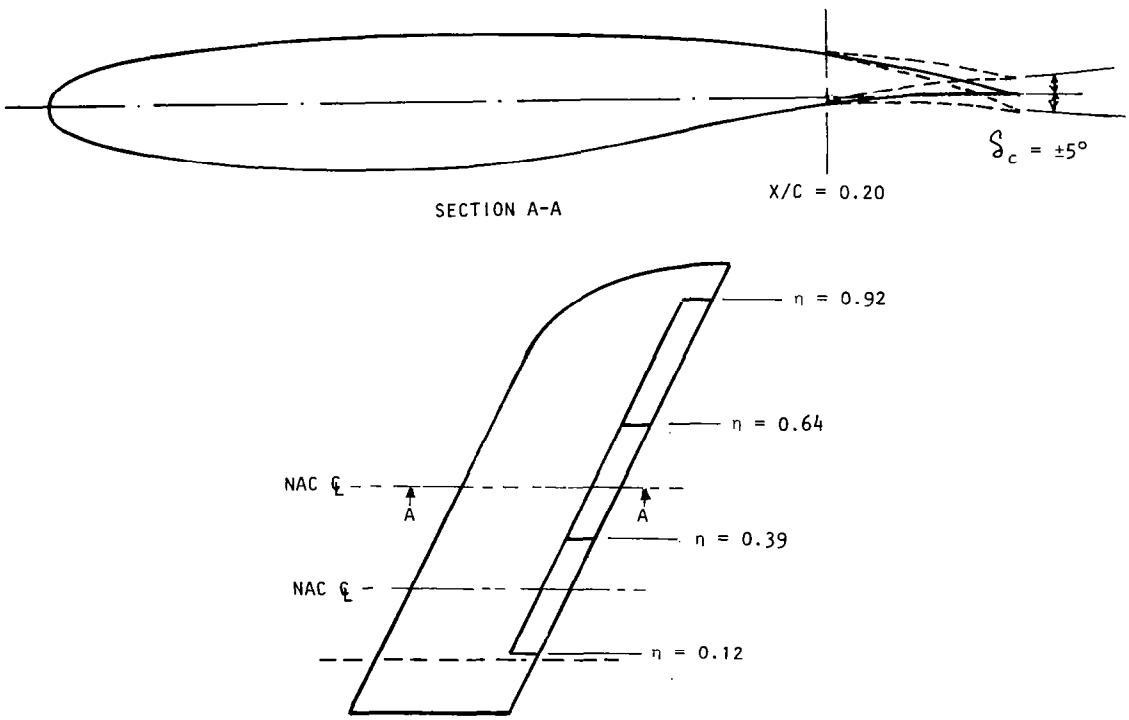


Figure 27. Details of variable camber for swept wing

section are reduced. The higher leading-edge peak promotes a strong terminating shock with excessive drag and possibly vortex formations along the inboard side of the nacelle. Furthermore, the nacelle overpressures can produce a higher crest suction level, thereby reducing the drag-rise Mach number. From these considerations, the design philosophy of the fillet on the inboard side of the nacelle was to reduce the leading edge pressure peaks as well as the crest suction level.

The resulting modified airfoil sections are compared with the clean wing section in Figure 28. The geometric features are that the leading-edge radius is considerably larger on the wing-fuselage and outboard nacelle-wing sections. The inboard nacelle wing section has a small leading-edge radius and a drooped leading-edge camber line, as would be expected with the suppression of the leading-edge suction peak. Both sections have a reduced thickness/chord ratio associated with the reduction in crest suction.

In general, the planform modifications associated with the fillet design are illustrated in Figure 29. The spanwise extent of the fillets was dictated by the location of pressure orifice rows. In actual practice, the fillets often were not extended aft quite as far as shown because of the extreme thinness of the material near the airfoil crest. A good example of a fillet installation is provided by the dual D-duct installation shown in Figure 30. Only the major portions of the fillets, as illustrated by the white areas in the photo, were made up in preparation for the tests. After these were bonded in place, the remaining parts of the fillets were formed with wax.

## 4.2 Nozzle Calibration Hardware

To determine the true installation effect, it was necessary to determine isolated nozzle performance accurately. This was done by means of a special calibration program performed in the Lockheed Low Speed Wind Tunnel.

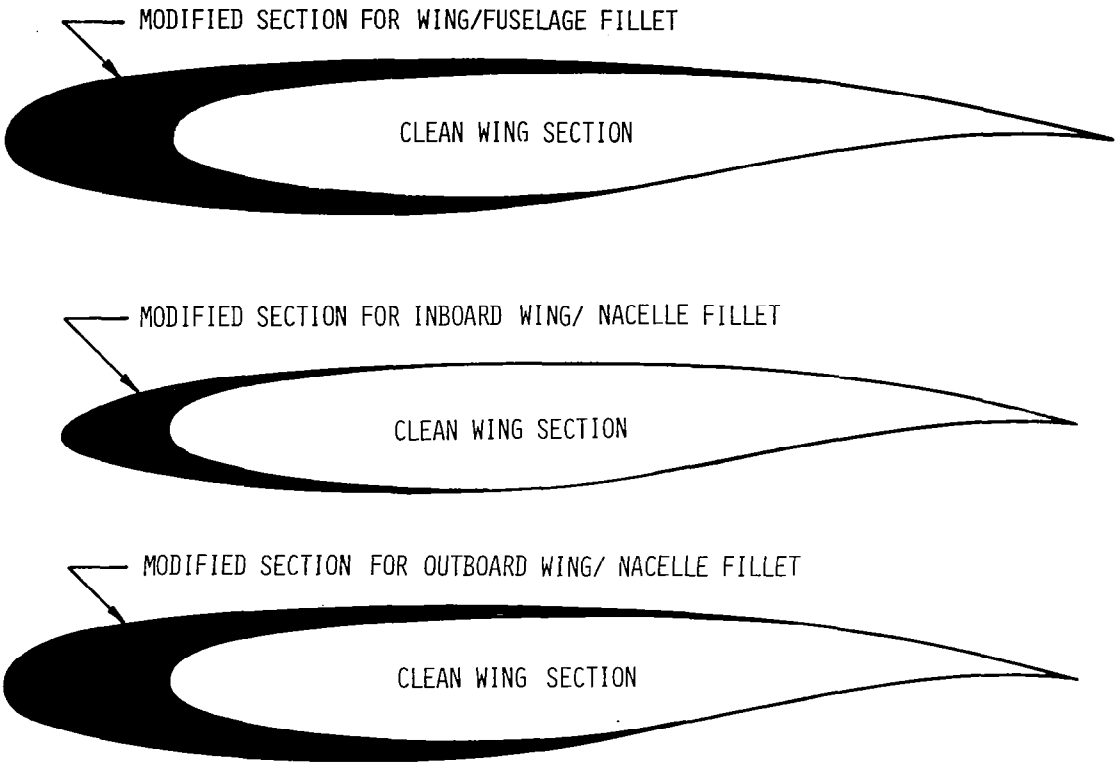


Figure 28. Comparison of clean wing and modified section geometry

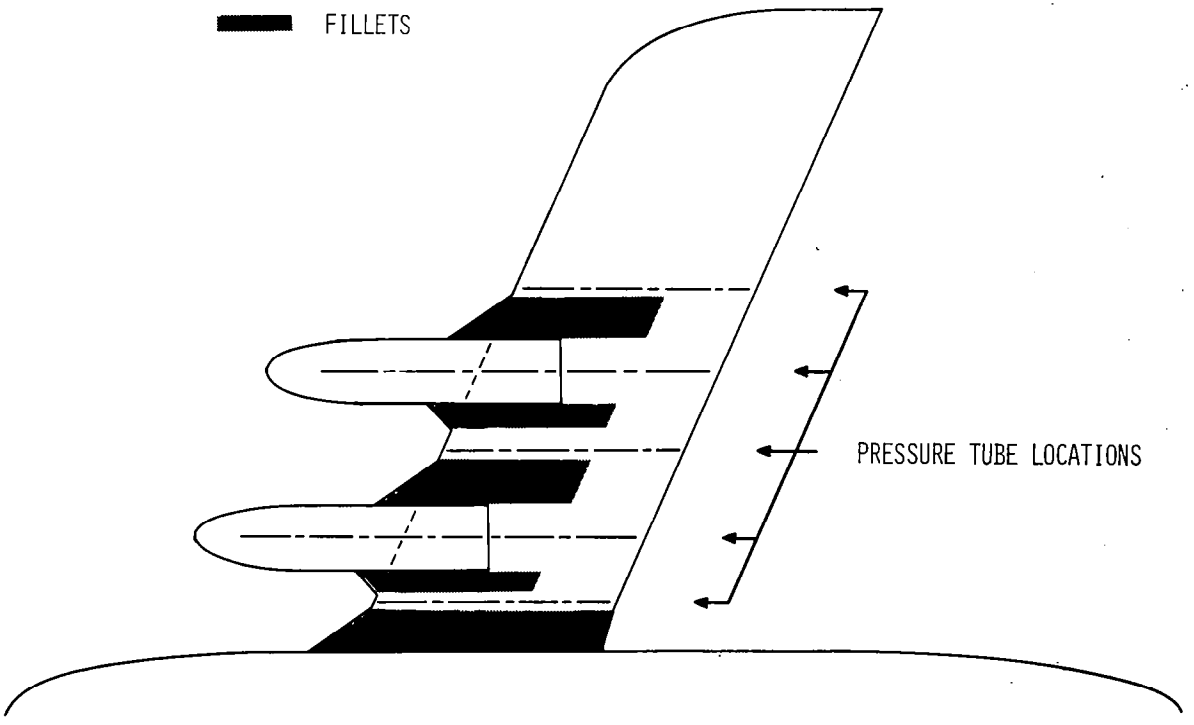


Figure 29. Swept wing fuselage/nacelle planform with fillets

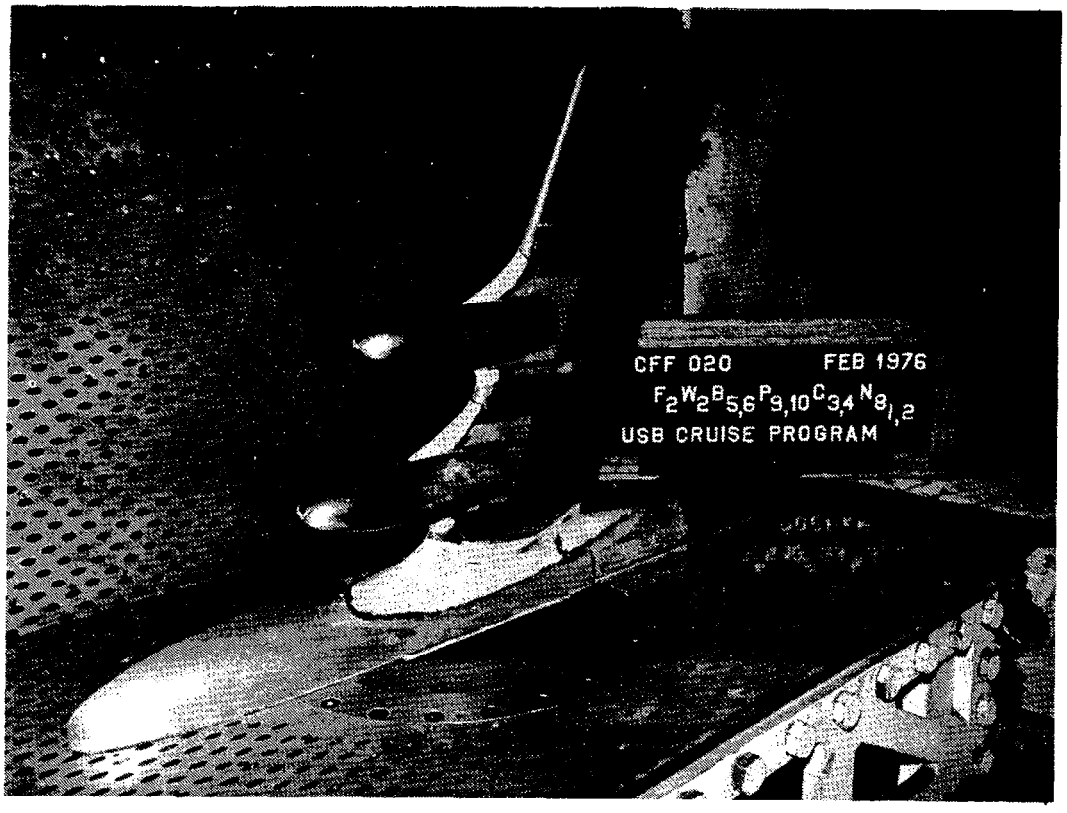


Figure 30. Fillet arrangement on dual D-duct installation in wind tunnel

4.2.1 Calibration Rig Details - A sketch of the calibration rig setup is presented in Figure 31. The rig is completely metric with a flexible supply hose which bridges the balance and connects to a calibrated orifice assembly for airflow measurement.

4.2.2 Calibration Rake - The calibration rake was designed to obtain accurate integrated average total pressures from a wide range of nozzle exit shapes. It could be positioned so that a circular nozzle was surveyed with a modified cruciform pattern, or it could be arranged so that a rectangular nozzle could be surveyed with the equivalent of one horizontal and three vertical rakes. The rake, shown in Figure 32, had a total of 57 probes, but the average nozzle used only about half of those available.

4.2.3 Calibration Rig Tunnel Setup - The complete rig with a circular nozzle is shown mounted in the tunnel test section in Figure 33(a). A closeup photograph showing the manner in which the rake is arranged for a typical case is presented in Figure 33(b).

## 4.3 CFF Instrumentation

4.3.1 CFF Test Section - Wind-on-test conditions in the CFF test section were measured by CEC force balance pressure transducers used in conjunction with CEC servo-amplifiers to provide a precise measurement of the atmospheric pressure, stagnation pressure, and test section static pressure to 0.05% of the 172.37 $N/cm^2$ (250 psi) capacity. These transducers allow determination of the test section Mach number to an accuracy of $\pm 0.002$ at the highest stagnation pressure.

Measurements of the static pressures on the airfoil surfaces and the wake rake pressures were made using electronically actuated pressure scanning valves. The full-scale range of the quarter percent accuracy Statham transducers in the valves was selected to provide maximum accuracy for the wind tunnel conditions tested. Internal total pressure near the model exit was measured by a separate Statham high-pressure transducer.

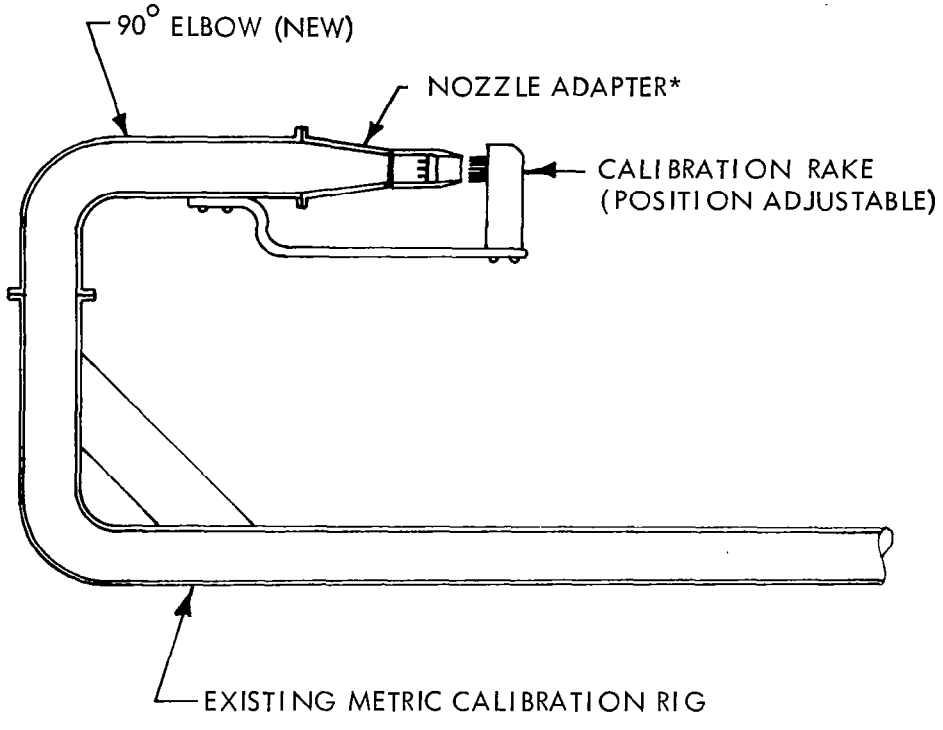


*THREE ADAPTERS ARE REQUIRED TO FIT ALL TEST NOZZLE SIZES

Figure 31. Nozzle calibration rig setup, low speed wind tunnel

USB CRUISE PROGRAM

TOTAL NUMBER OF PROBES = 57

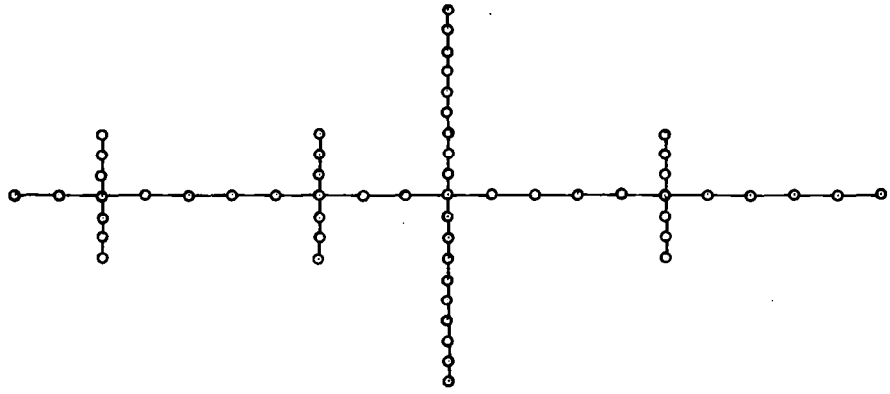

TYPICAL VERTICAL SPACING = .318 cm (1/8 in.)

TYPICAL HORIZONTAL SPACING = .635 cm (1/4 in.)

Figure 32. Nozzle calibration rake probe pattern

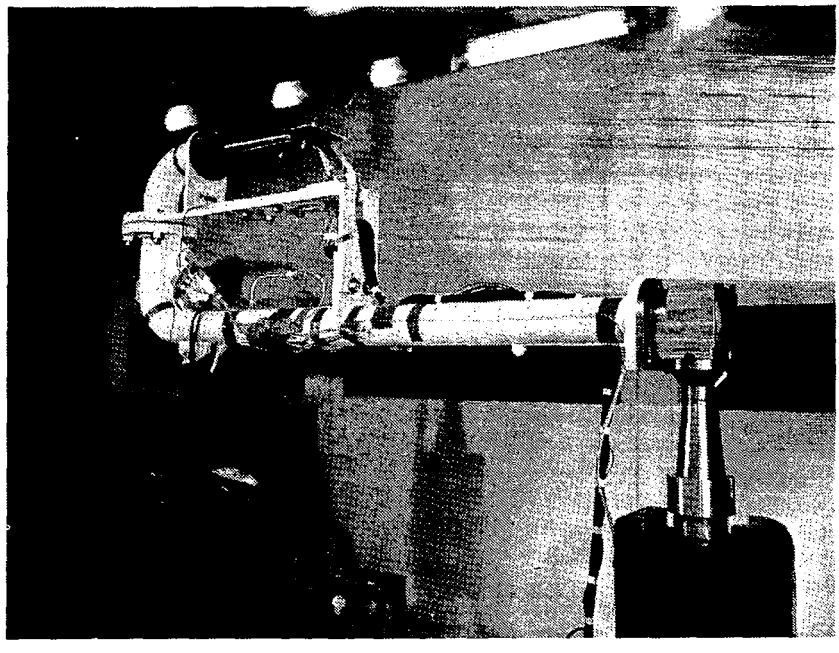

(a)

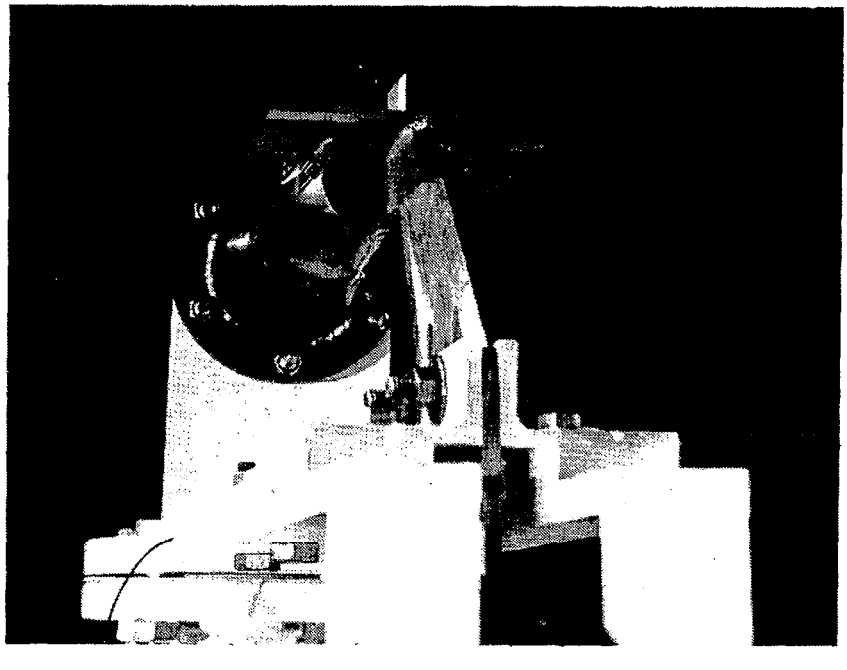

(b)

Figure 33. Nozzle calibration rig and nozzle exit rake arrangement

Raw pressure data were recorded on magnetic tape, using the CFF high-speed data acquisition system. The data acquisition system consists of a Lockheed **Electronics** Company MAC-16 computer and associated peripheral equipment. The raw data were reduced to coefficient form with a CDC 1700 computer.

Angle of attack was measured with a calibrated potentiometer operated by the angle-of-attack drive mechanism.

A matrix of 82 static pressure orifices in the tunnel side wall was used to investigate test section blockage corrections due to the powered model configurations. The relative locations of these pressure orifices are shown in Figure 34.

4.3.2 CFF Balance - The CFF floor-mounted balance was used for all force testing of the semi-span models. This 5-component balance is capable of measuring lift, drag, pitching moment, rolling moment, and yawing moment of the model. High-pressure air was provided to the model by means of an internal bellows arrangement.

4.3.3 Internal Flow Measurement - A schematic diagram of the model internal flow system is presented in Figure 35. Airflow going into the system was measured by the orifice assembly which was calibrated to read airflow as a function of the pressure decrement between Stations 1 and 2, and the airstream temperature. A check on these measurements was obtained by means of the relationship between corrected airflow and total pressure at Station 4 generated during the calibration.

4.3.4 Traversing Wake Rake - Since it was considered desirable to determine the downstream total pressure patterns for a variety of upper surface blown configurations including pylon arrangements, a large, traversing wake rake was fabricated. Figure 36 shows the basic features of the design that was selected for the USB program. Oriented vertically, it had 214 probes

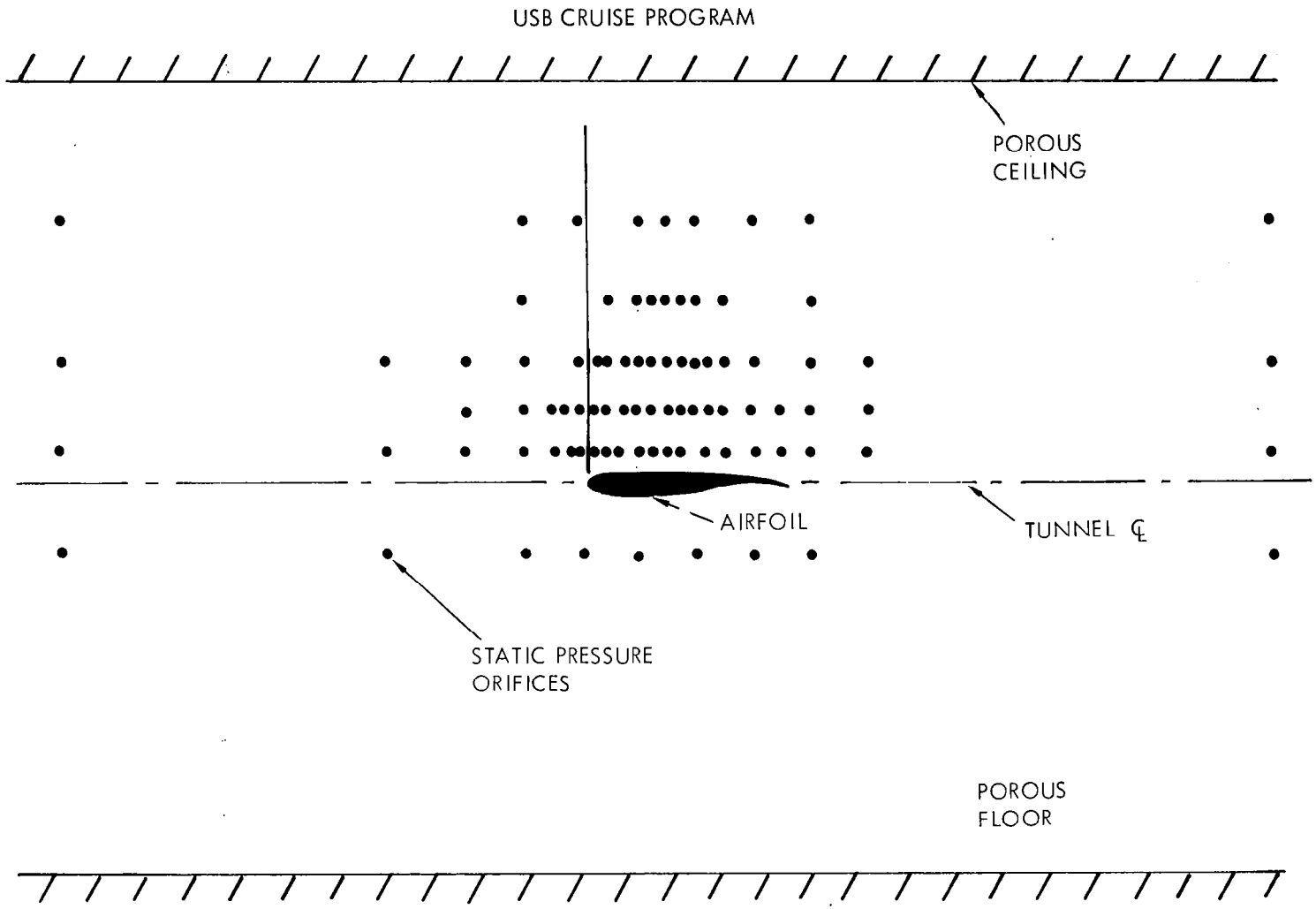


Figure 34. Tunnel side wall orifice locations

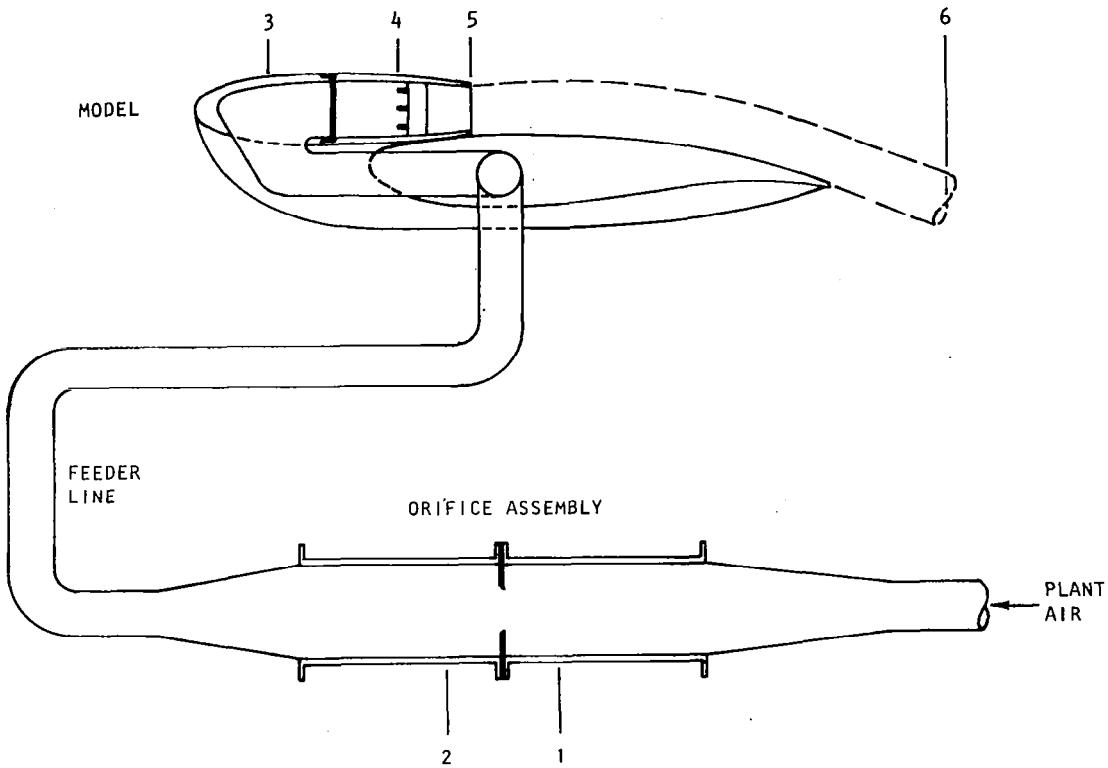


Figure 35. Schematic of nacelle internal flow system

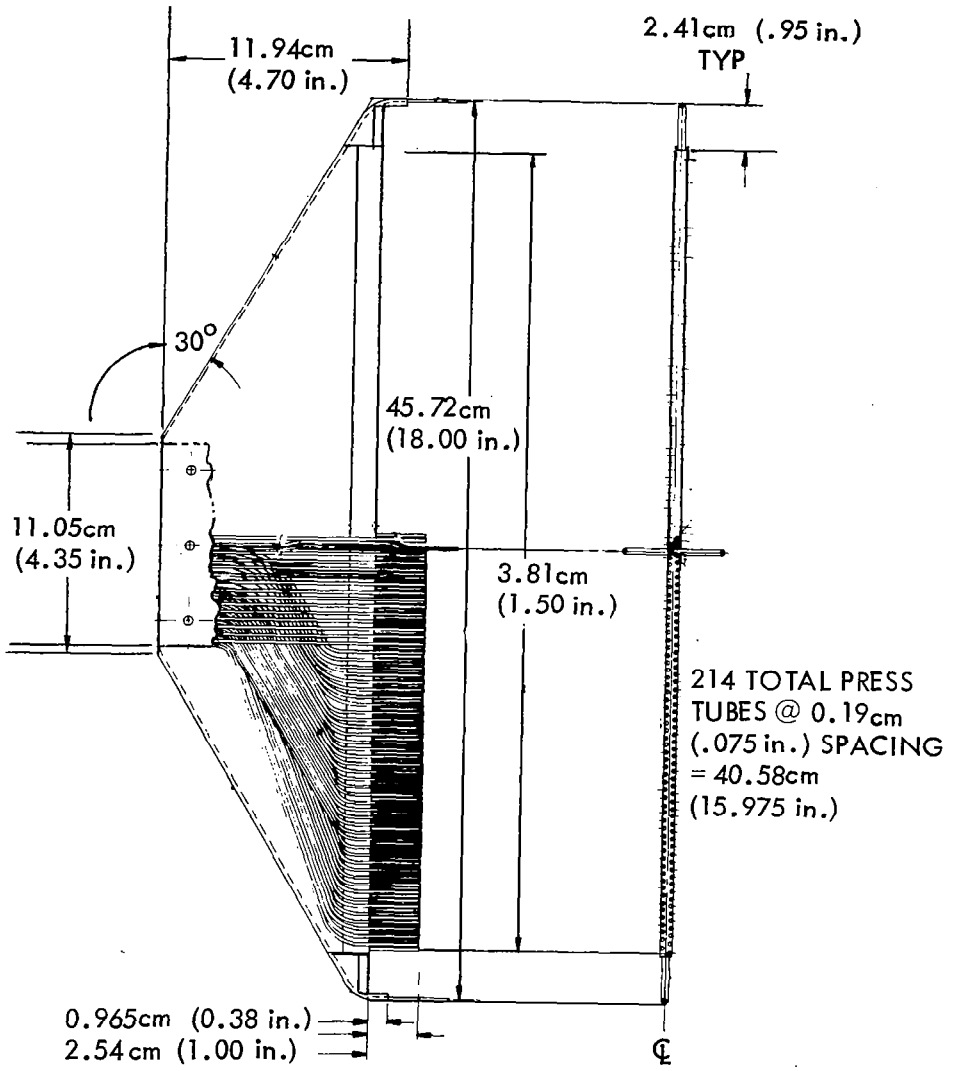


Figure 36. Total pressure probe layout for traversing wake rake

spaced at 0.19 cm (0.075 in.) intervals. To facilitate fabrication, alternate probes were slightly displaced horizontally. Five scanivalves were housed in a pod directly behind the center of the rake, so that the size of the tube bundle connecting through the tunnel wall was minimized. Two circular bars provided tracks for the transverse movement of the rake, while the traversing drive motor and gearbox installation were located just outside the tunnel wall.

## 4.4 Low Speed, High Lift Model Description

The test vehicle employed in the high-lift performance study was a short-haul type of aircraft configuration around which numerous high-lift investigations, powered and unpowered, had been previously performed. Figures 37 and 38 show the 216 cm (7-foot) span model mounted in the Lockheed-Georgia low speed wind tunnel. Powered-lift is derived from two ejector-powered nacelles with D-duct (semi-circular) nozzles exhausting over Coanda plates attached to the upper surfaces of triple-slotted flaps. A full span, high-camber Krueger-type flap provides the leading-edge stall protection. Pertinent model dimensions are given in Table I.

4.4.1 Wing - The quarter chord wing sweep is 14.92 degrees and the aspect ratio is 7.73. The basic airfoil is a Lockheed-developed section with 0.125 c thickness at the tip. The ordinates of these sections are tabulated and plotted in Table II.

4.4.2 Leading-Edge Device - The leading-edge device consisted of a full-span, Krueger-type flap closely fitted at the flap-pylon juncture. The flap reference line was deflected downward 50 degrees from the wing chordline and the gap between the flap trailing-edge and wing was sealed. This leading-edge configuration was maintained throughout the tests. The cross-sectional shape of the leading-edge flap represented a high-camber contour as reflected in the flap ordinates tabulated and plotted in Table III.

4.4.3 Trailing-Edge Flaps - The trailing-edge flap system consisted of 56 percent span, triple-slotted flaps as illustrated in Figure 39. The flap

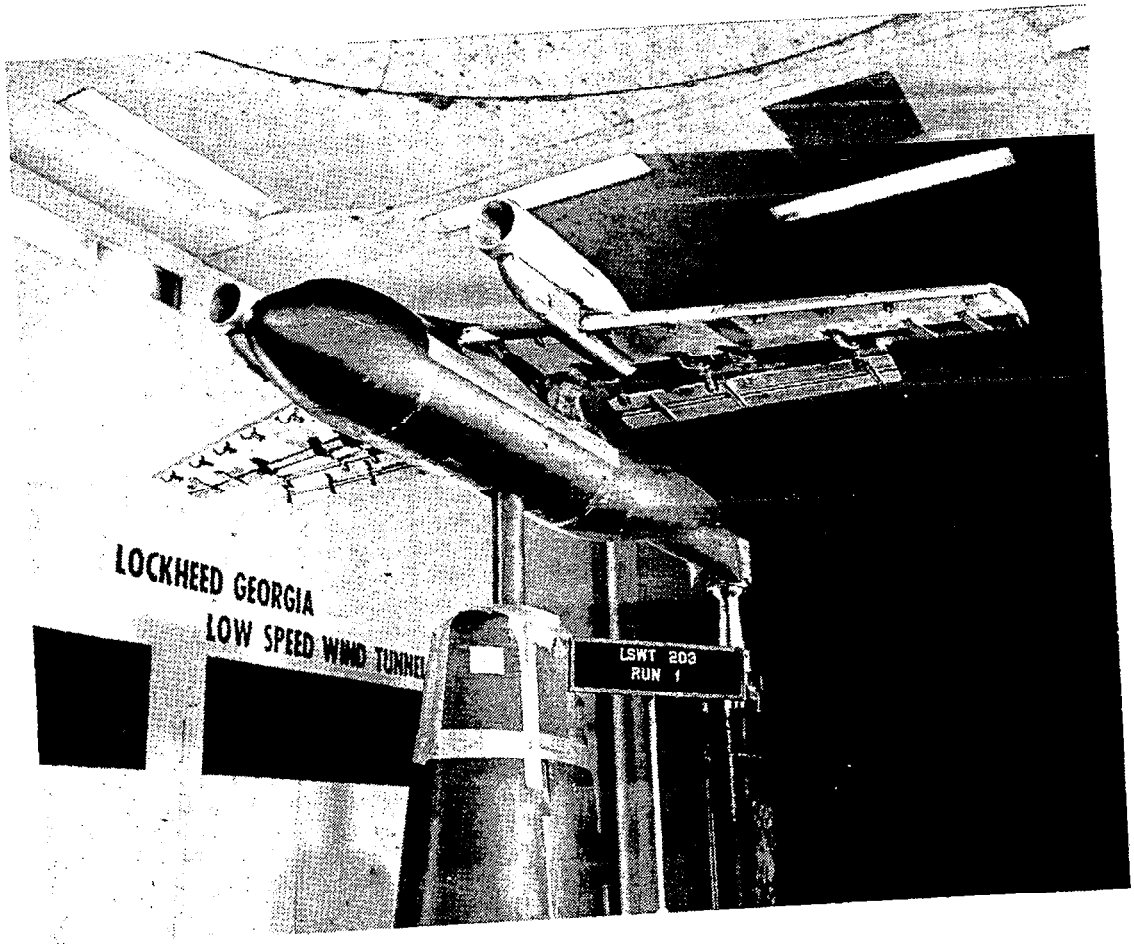


Figure 37. Low speed, high lift test model

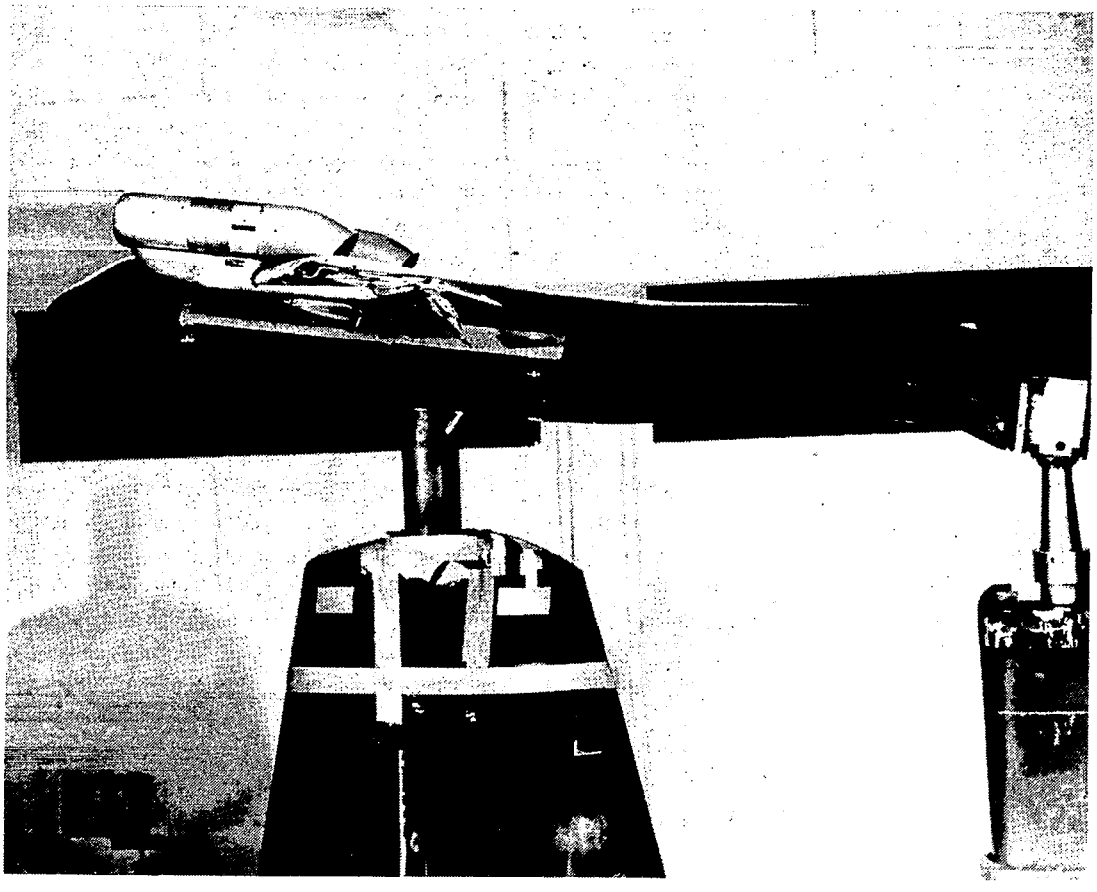

Figure 38. View of USB nozzles on low speed, high lift test model

USB CRUISE PROGRAM

TABLE I. - HIGH-LIFT MODEL DIMENSIONAL DATA

| Wing | Dimension | |
|---|---|---|
| Area, square meters (square feet) | 0.6033 | ( 6.494) |
| Span, centimeters (inches) | 216.052 | (85.026) |
| MAC length, centimeters (inches) | 28.928 | (11.387) |
| Sweep of c/4, degrees | 14.918 | |
| Taper ratio | 0.509 | |
| Aspect ratio | 7.731 | |
| Incidence, degrees | 3.0 | |
| Twist, degrees | 0 | |
| Anhedral, degrees | 0 | |
| Thickness ratio, % local wing chord | | |
| Root | 13.7 | |
| Tip | 10.5 | |
| **Leading Edge Flaps (Full Span)** | | |
| Chord length, % local wing chord | 17 | |
| Deflection angle, degrees | 50 | |
| **Trailing Edge Flaps** | | |
| Flap span, centimeters (inches) | 60.85 | (24.0) |
| Flap chord extension along engine centerline, centimeters (inches) | 10.41 | ( 4.1) |
| Flap chord extension along engine centerline, % local wing chord | 32.5 | |
| Coanda plate, % semispan | 16.3 | |
| **Fuselage** | | |
| Length, centimeters (inches) | 206.726 | (81.388) |
| Maximum frontal area, square meters (square feet) | 0.0527 | ( 0.567) |
| Maximum diameter, centimeter (inches) | 25.908 | (10.200) |
| **Nacelles** | | |
| Length, centimeters (inches) | 43.43 | (17.10) |
| Diameter, centimeters (inches) | 10.92 | ( 4.30) |
| Exit width, centimeters (inches) | 11.384 | ( 4.482) |
| Nozzle aspect ratio | 2.5 | |
| Exit area, square centimeters (square inches) | 50.90 | ( 7.889) |
| Spanwise nacelle location, % wing semi-span | 28.8 | |
| Chordwise nozzle exit location, % local chord | 35 | |

TABLE II. - WING SECTION CONTOURS OF ROOT AND TIP SECTIONS, HIGH-LIFT MODEL

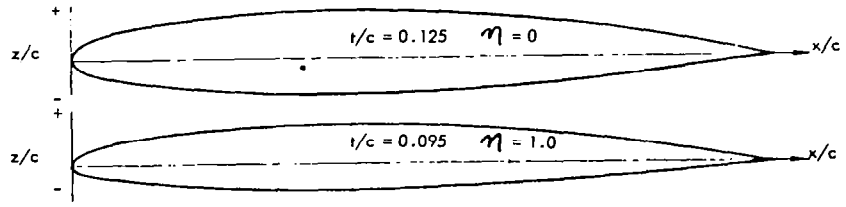


| x/c | z/c | | | |
|---|---|---|---|---|
| | Upper | | Lower | |
| | η = 0 | η = 1.0 | η = 0 | η = 1.0 |
| 0.0 | 0.0 | 0.0 | 0.0 | 0.0 |
| 0.00125000 | 0.00572317 | 0.00443440 | -0.00537467 | -0.00391100 |
| 0.00250000 | 0.00812602 | 0.00636791 | -0.00745688 | -0.00536297 |
| 0.00375000 | 0.00997585 | 0.00787970 | -0.00900261 | -0.00641807 |
| 0.00500000 | 0.01153987 | 0.00917388 | -0.01027016 | -0.00726702 |
| 0.00625000 | 0.01291596 | 0.01032104 | -0.01136523 | -0.00799216 |
| 0.00750000 | 0.01415987 | 0.01136577 | -0.01233640 | -0.00862732 |
| 0.01000000 | 0.01636764 | 0.01323777 | -0.01401720 | -0.00970796 |
| 0.01250000 | 0.01830336 | 0.01489240 | -0.01545995 | -0.01062228 |
| 0.01875000 | 0.02238220 | 0.01841221 | -0.01842389 | -0.01246779 |
| 0.02500000 | 0.02575428 | 0.02134313 | -0.02082859 | -0.01394589 |
| 0.05000000 | 0.03555018 | 0.02982411 | -0.02792389 | -0.01837053 |
| 0.07499999 | 0.04222788 | 0.03544696 | -0.03316647 | -0.02183691 |
| 0.09999990 | 0.04733324 | 0.03966150 | -0.03737882 | -0.02470893 |
| 0.14999998 | 0.05509348 | 0.04610780 | -0.04366652 | -0.02894142 |
| 0.19999999 | 0.06074440 | 0.05085341 | -0.04810718 | -0.03186756 |
| 0.25000000 | 0.06488276 | 0.05436992 | -0.05124890 | -0.03388572 |
| 0.29999989 | 0.06777489 | 0.05686748 | -0.05333706 | -0.03517465 |
| 0.34999990 | 0.06954688 | 0.05844624 | -0.05448649 | -0.03581752 |
| 0.39999998 | 0.07025450 | 0.05915145 | -0.05474475 | -0.03584716 |
| 0.44999999 | 0.06991160 | 0.05899128 | -0.05413271 | -0.03528224 |
| 0.50000000 | 0.06853825 | 0.05798045 | -0.05267122 | -0.03413878 |
| 0.54999989 | 0.06615323 | 0.05612940 | -0.05038956 | -0.03244295 |
| 0.59999990 | 0.06277531 | 0.05344871 | -0.04731639 | -0.03022005 |
| 0.64999998 | 0.05841661 | 0.04993883 | -0.04348744 | -0.02750618 |
| 0.69999999 | 0.05309385 | 0.04560722 | -0.03893371 | -0.02433011 |
| 0.75000000 | 0.04681299 | 0.04044509 | -0.03369706 | -0.02073700 |
| 0.79999989 | 0.03957576 | 0.03443734 | -0.02782363 | -0.01677852 |
| 0.84999990 | 0.03137351 | 0.02755326 | -0.02137010 | -0.01252209 |
| 0.89999998 | 0.02217282 | 0.01972492 | -0.01441823 | -0.00807286 |
| 0.94999999 | 0.01188206 | 0.01079715 | -0.00710873 | -0.00362475 |
| 0.97499990 | 0.00624426 | 0.00578988 | -0.00341987 | -0.00154595 |
| 1.00000000 | 0.0 | 0.0 | 0.0 | 0.0 |

USB CRUISE PROGRAM

TABLE III. - LEADING EDGE FLAP CONTOURS, HIGH-LIFT MODEL

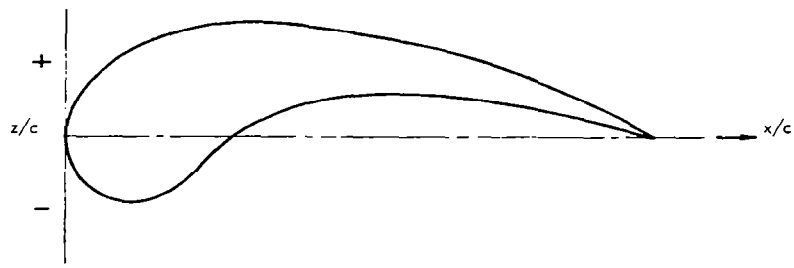


| x/c | z/c | |
|---|---|---|
| | Upper | Lower |
| 0.0 | 0.0 | 0.0 |
| 0.025 | 0.0714 | -0.0715 |
| 0.050 | 0.104 | -0.0925 |
| 0.075 | 0.1275 | -0.1078 |
| 0.100 | 0.1450 | -0.1141 |
| 0.150 | 0.1720 | -0.1113 |
| 0.200 | 0.189 | -0.0825 |
| 0.250 | 0.200 | -0.0295 |
| 0.300 | 0.202 | 0.0105 |
| 0.400 | 0.198 | 0.0552 |
| 0.500 | 0.181 | 0.0724 |
| 0.600 | 0.161 | 0.0760 |
| 0.700 | 0.134 | 0.0646 |
| 0.800 | 0.100 | 0.0475 |
| 0.900 | 0.059 | 0.0248 |
| 1.000 | 0.0 | 0.0 |

USB CRUISE PROGRAM

| TEST CONFIGURATION | FLAP ANGLE, $\delta_f$ | FLAP UPPER SURFACE ANGLE, $\delta_{fs}$ | COANDA PLATE | TAPE |
|---|---|---|---|---|
| 1 | 42.5° | 56.5° | YES | NO |
| 2 | 42.5° | 56.5° | NO | YES |
| 3 | 25.0° | 34.0 | YES | NO |
| 4 | NO FLAPS | NO FLAPS | NO | NO |
| 5 | 52.0° | 66.0 | YES | NO |

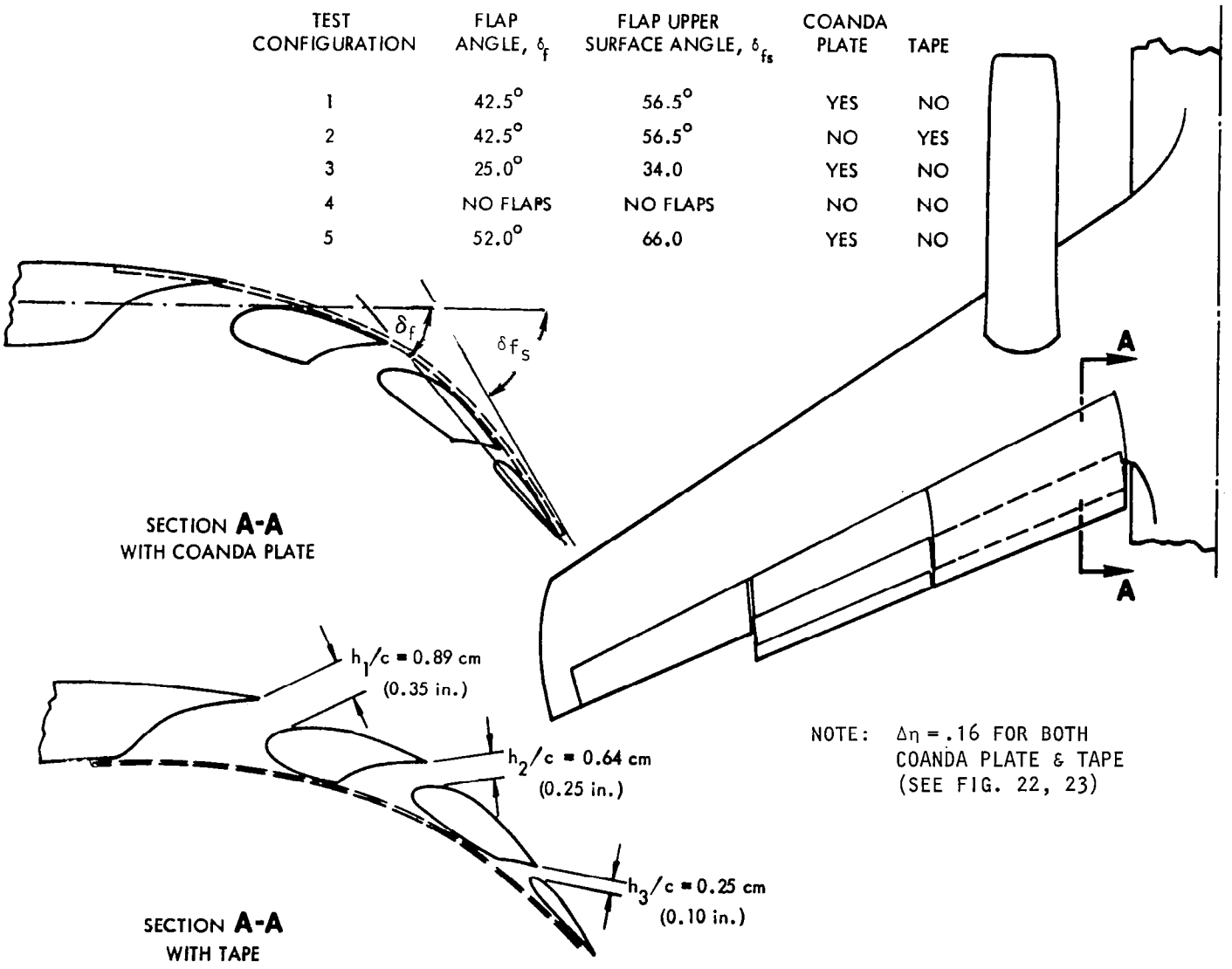


Figure 39. Trailing edge flap system design details, low speed model

gaps, also given on the figure, were held constant during the course of the investigation. A smooth, Coanda plate covered the upper-surface of the flaps immediately behind the nacelle and across a flap span of $\Delta\eta = 0.16$. For one series of test points, tape along the lower surface was employed as a substitute for the Coanda plate. In this case, also, a $\Delta\eta$ of 0.16 was covered. Three flap deflections were investigated. These were $25^{\circ}$, $42.5^{\circ}$ and $52^{\circ}$ defined in terms of the flap chord-to-wing chord angle as indicated in Figure 38; in terms of the upper-surface angle at the trailing-edge, these became $34^{\circ}$, $56.5^{\circ}$ and $66^{\circ}$, respectively.

4.4.4 Fuselage - The fuselage had a constant 25.908 cm (10.2 in.) diameter center section. Forward and aft fairings were added to give a total length of 206.726 cm (81.388 in.) and fineness ratio of 7.98. Overall contouring represents a typical transport fuselage with aft loading capability.

4.4.5 Nacelles - Installation of the nacelles on the wing is illustrated in Figure 40. Details of the nozzle design are shown in Figure 41. The nacelles were powered by pneumatically driven ejector engine simulators and each had 50.895 $cm^2$ (7.889 $in.^2$) nozzle exit area. The nozzle shape employed was a D-duct (AR = 2.5) with a discharge position at 35% chord. An internal roof angle of $30^{\circ}$ was utilized to ensure jet attachment at the maximum flap angle setting and was designed to represent the deflector mechanism employed on the Task III baseline design.

## 4.5 Instrumentation For High Lift Model

The model was mounted on the six-component pyramidal balance system in the 16' x 23' test section of the Lockheed Low Speed Wind Tunnel. Airflow to the nacelles was measured by the wind tunnel air supply orifice system. Inside the nacelles, nozzle pressures were measured by twelve total pressure probes manifolded together and routed to a single pressure transducer inside the model fuselage. Thrust level as a function of nozzle pressure ratio was obtained by removing the flaps and operating the nozzles statically.

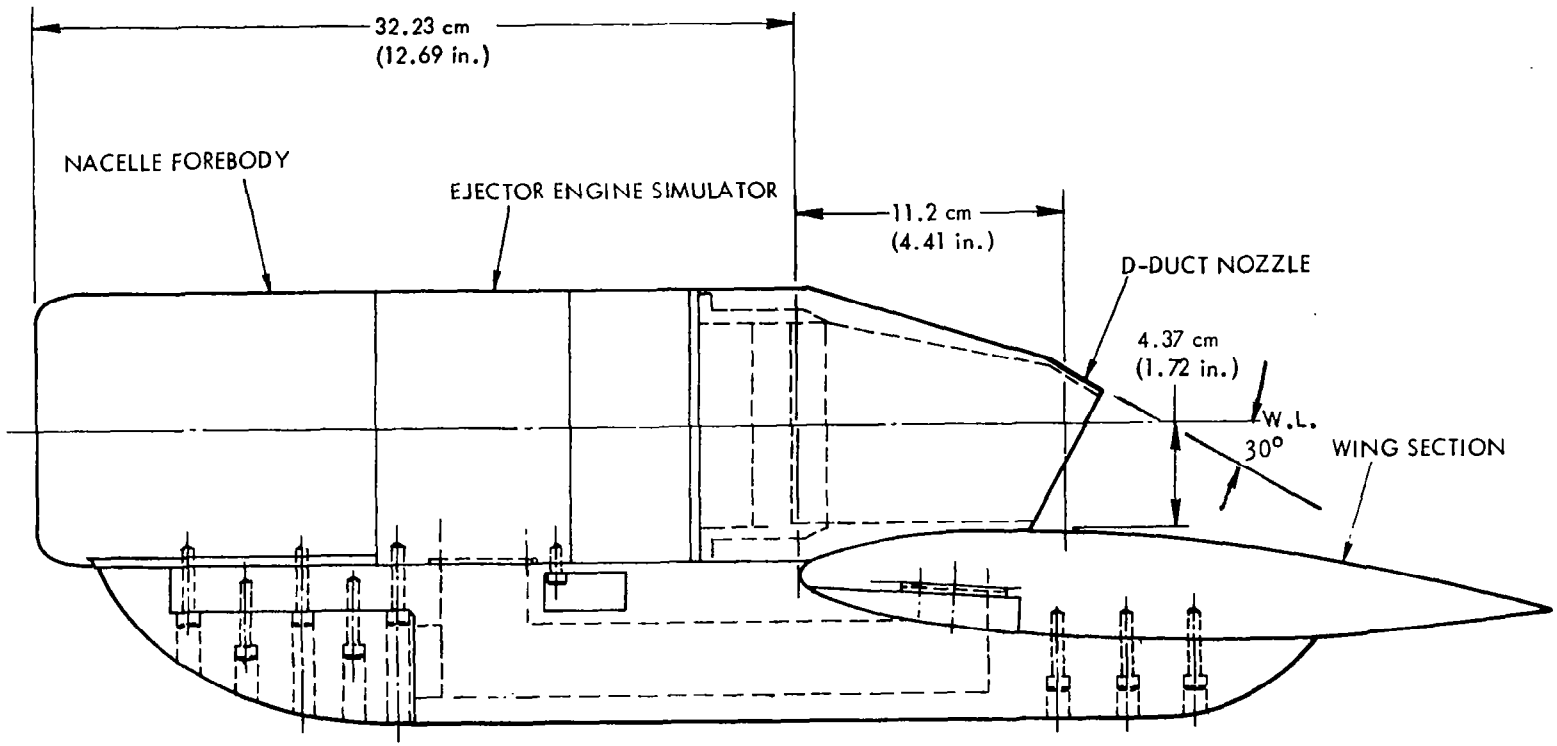


Figure 40. Nacelle installation on the wing

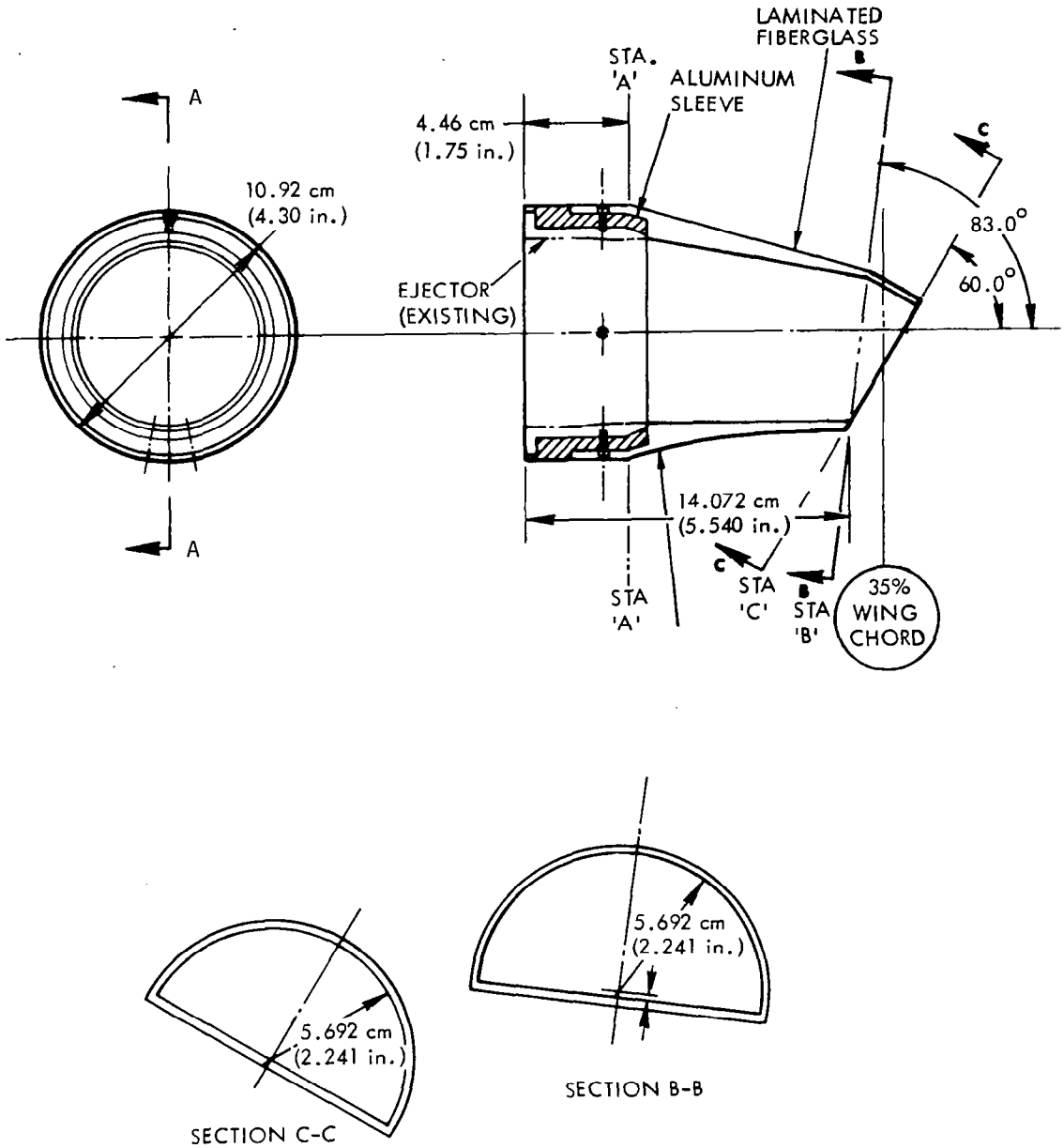


Figure 41. Nozzle design details

## 5.0 HIGH-LIFT TEST DESCRIPTION

### 5.1 Test Schedule

The run schedule for the investigation is provided in Figure 42. As noted, the tunnel dynamic pressure was held constant at 718.2 $N/m^2$ (15 psf) for all wind-on runs. This provided a test Reynolds number of $7.1 \times 10^5$ based on wing chord. Force tests were completed first, followed by flow visualization runs. In the latter cases, the model was painted black and a mixture of motor oil and titanium dioxide was applied to the wing, nacelle and flaps.

### 5.2 Test Results

5.2.1 Installed Performance of Engine Simulator - The ejector-powered nacelles were installed on the wing, with flaps removed, and tested statically. This provided the thrust coefficients given in Figure 43 based on the tunnel dynamic pressure of 718.2 $N/m^2$ (15 psf).

5.2.2 Static Performance of Nozzle-Wing-Flap System - With the flaps installed at the selected flap angles and the Coanda plate in place, static tests were conducted to determine thrust turning efficiency ($\eta_t$) and effective turning angle, $\delta_j$. These results are provided in Figure 44 in conventional polar form and as a function of nozzle pressure ratio in Figure 45. The expressions for determination of $\eta_t$ and $\delta_j$ as the vector-summation of the balanced-measured forces are given on Figure 45.

5.2.3 Wind-On Performance of Complete Model - Wind-on, high-lift performance for the three selected flap angles is given in Figures 46 through 57 in terms of lift, drag and pitching moment as a function of $C_\mu$. The drag data, as presented, are not corrected for ram drag of the inlet air flow into the ejector unit. Such a correction would amount to a $\Delta C_D$ of approximately 0.10.

USB CRUISE PROGRAM

| RUN NO. | α SCHED. | $q_\infty$ $N/m^2$ (psf) | $H_i/P_\infty$ | FLOW VIS. (OIL FLOW) | CONFIG-URATION NO. | FLAP DEFLEC-TION ANGLE, $\delta_f$ ~ DEG | COANDA PLATE | TAPE | REMARKS |
|---|---|---|---|---|---|---|---|---|---|
| 1 | 0 | 0 | 1.0 to 1.5 | NO | 1 | 42.5 | YES | NO | Static Cali-bration |
| 2 | 0 | 0 | 1.0 to 1.5 | | | | | | Static Cali-bration repeat |
| 3 | A | 718.2 (15) | 1.0 | | | | | | |
| 4 | | | 1.1 | | | | | | |
| 5 | | | 1.2 | | | | | | |
| 6 | | | 1.3 | | | | | | Void |
| 7 | | | 1.3 | | | | | | |
| 8 | | | 1.3 | | | | | | |
| 9 | | | 1.5 | | | | | | |
| 10 | | | 1.0 | | 2 | | NO | YES | |
| 11 | | | 1.2 | | | | | | |
| 12 | | | 1.3 | | | | | | |
| 13 | | | 1.5 | | | | | | |
| 14 | | | 1.3 | | | | | | |
| 15 | | | 1.0 | | 3 | 25.0 | YES | NO | |
| 16 | | | 1.2 | | | | | | |
| 17 | | | 1.3 | | | | | | |
| 18 | | | 1.5 | | | | | | |
| 19 | 0 | 0 | 1.0 to 1.5 | | 4 | 0 | | | No Flaps, Static Run |
| 20 | A | 718.2 (15) | 1.0 | | 5 | 52.0 | | | |
| 21 | | | 1.2 | | | | | | |
| 22 | | | 1.3 | | | | | | |
| 23 | | | 1.5 | | | | | | |
| 24 | 20 | | 1.5 | YES | 5 | 52.0 | | | |
| 25 | 10 | | 1.5 | | 1 | 42.5 | | | |
| 26 | 10 | | 1.3 | | 3 | 25.0 | | | |

SCHEDULE A - - 4, 0, 4, 8, 12, 16, 20, 24, 28, 30

Figure 42. Low speed, high lift model run schedule

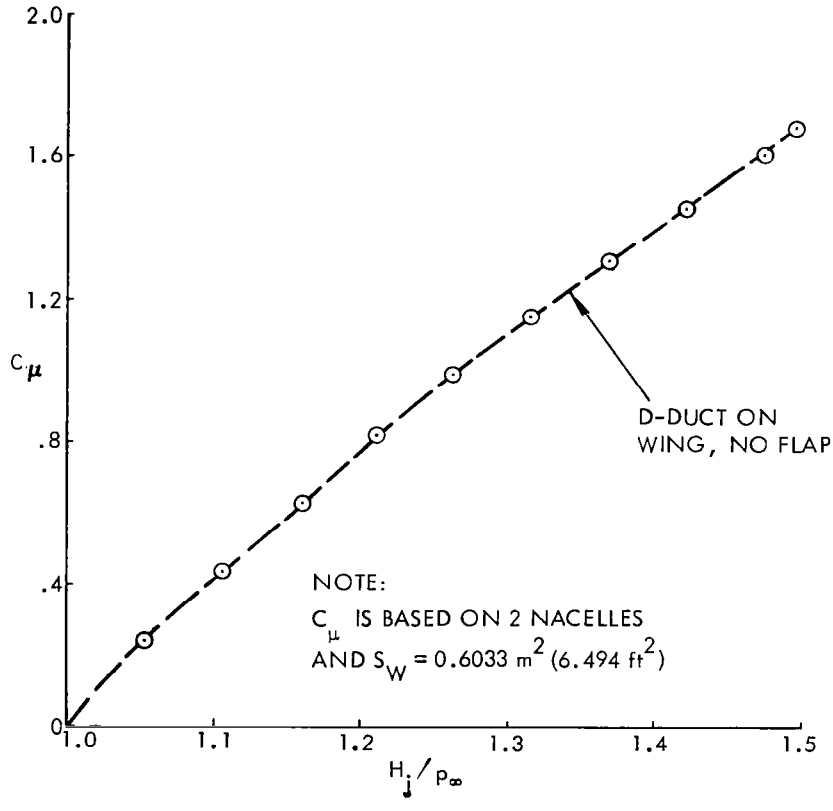


Figure 43. Low speed model thrust coefficient, $q_\infty = 718.2\ N/m^2$ (15 $lb/ft^2$)

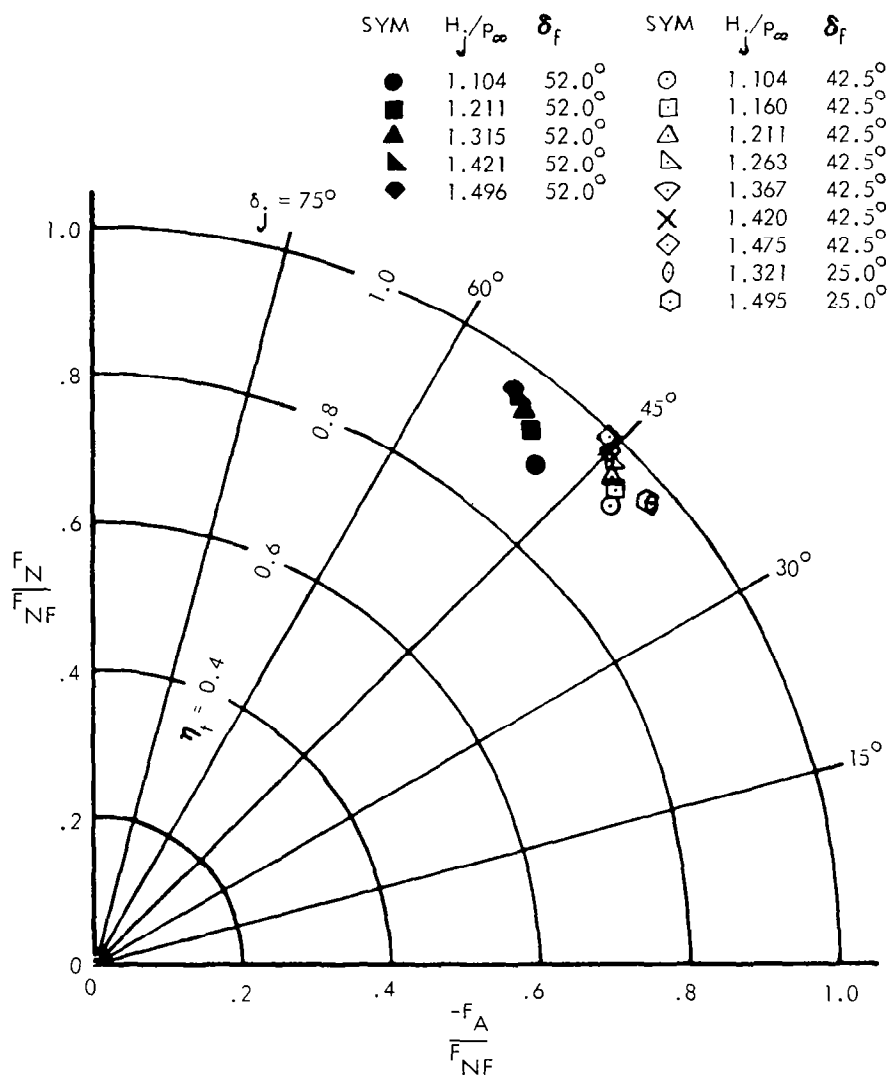


Figure 44. Low speed model static turning characteristics

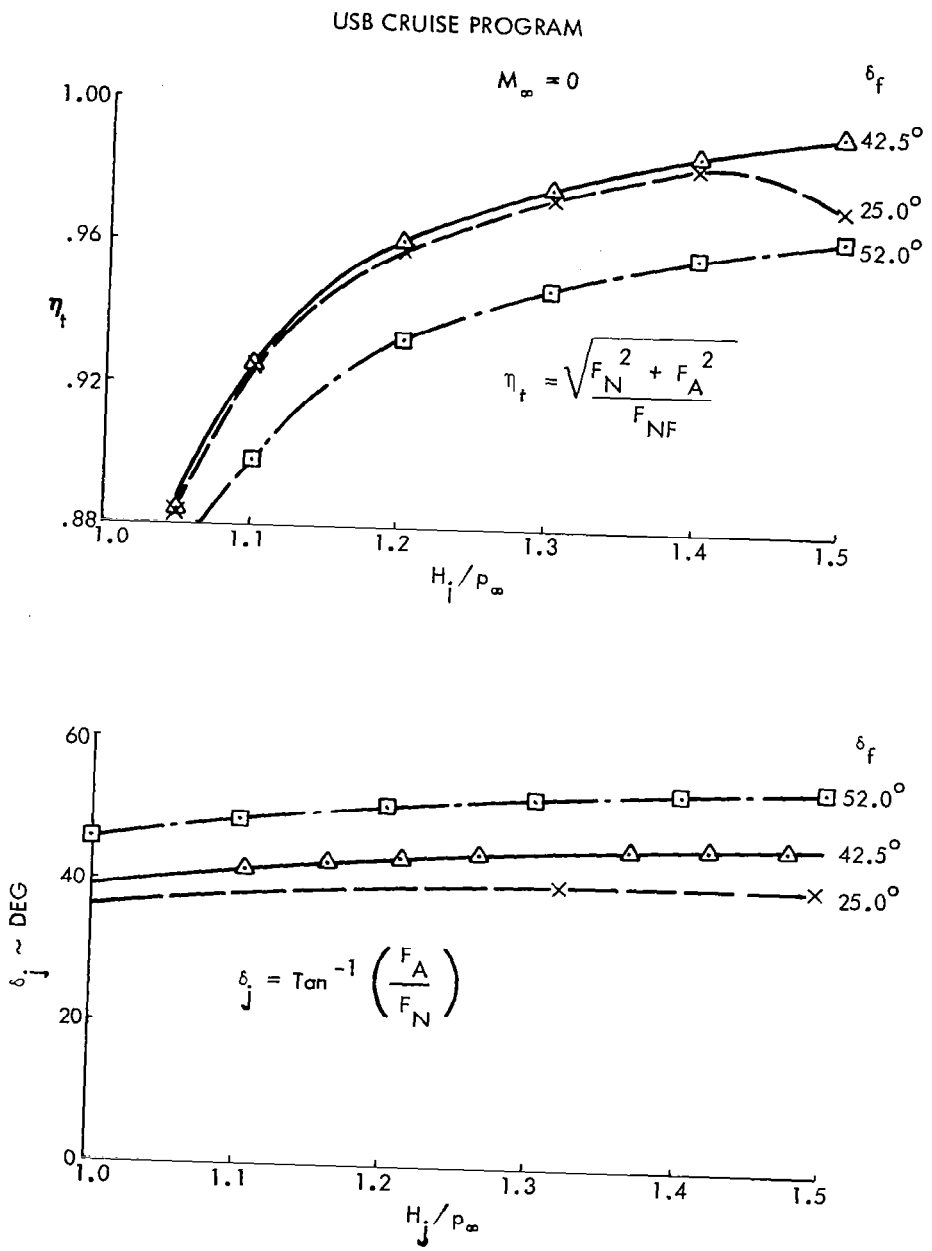


Figure 45. USB low speed model propulsion performance

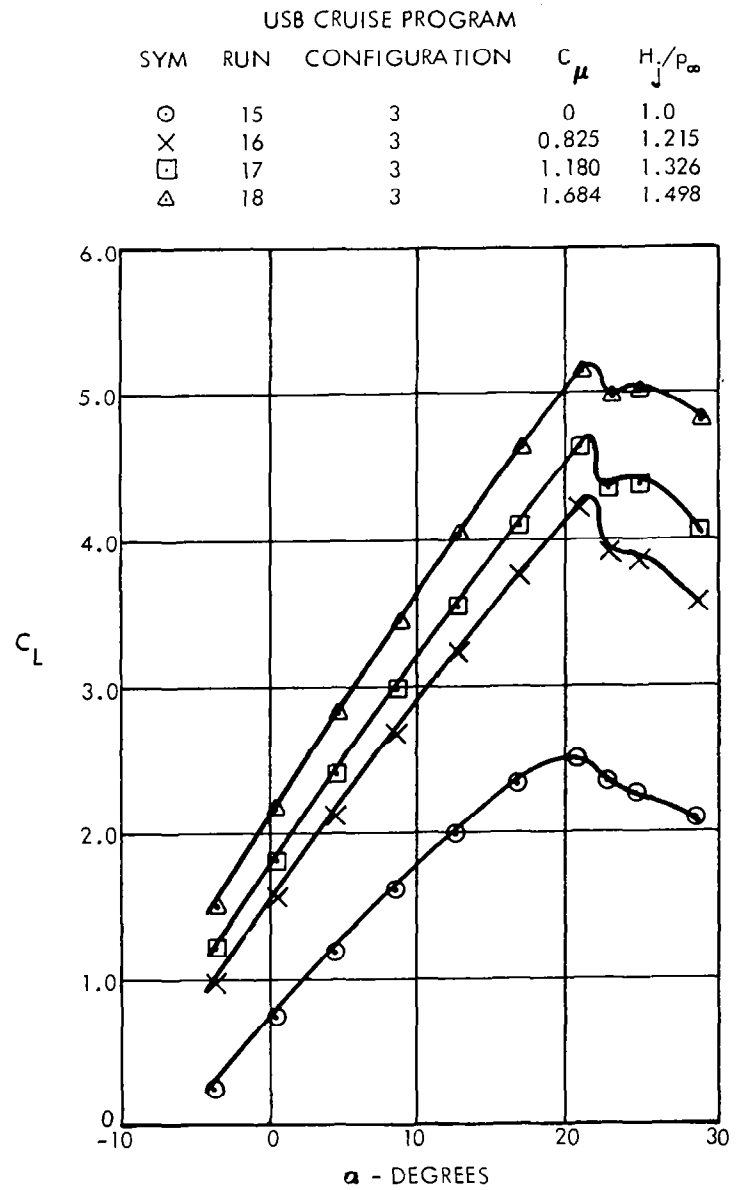


Figure 46. Variation of low speed model lift coefficient with angle of attack, $q_\infty = 718.2$ N/m$^2$ (15 lb/ft$^2$), $\delta_f = 25^o$, Coanda plate

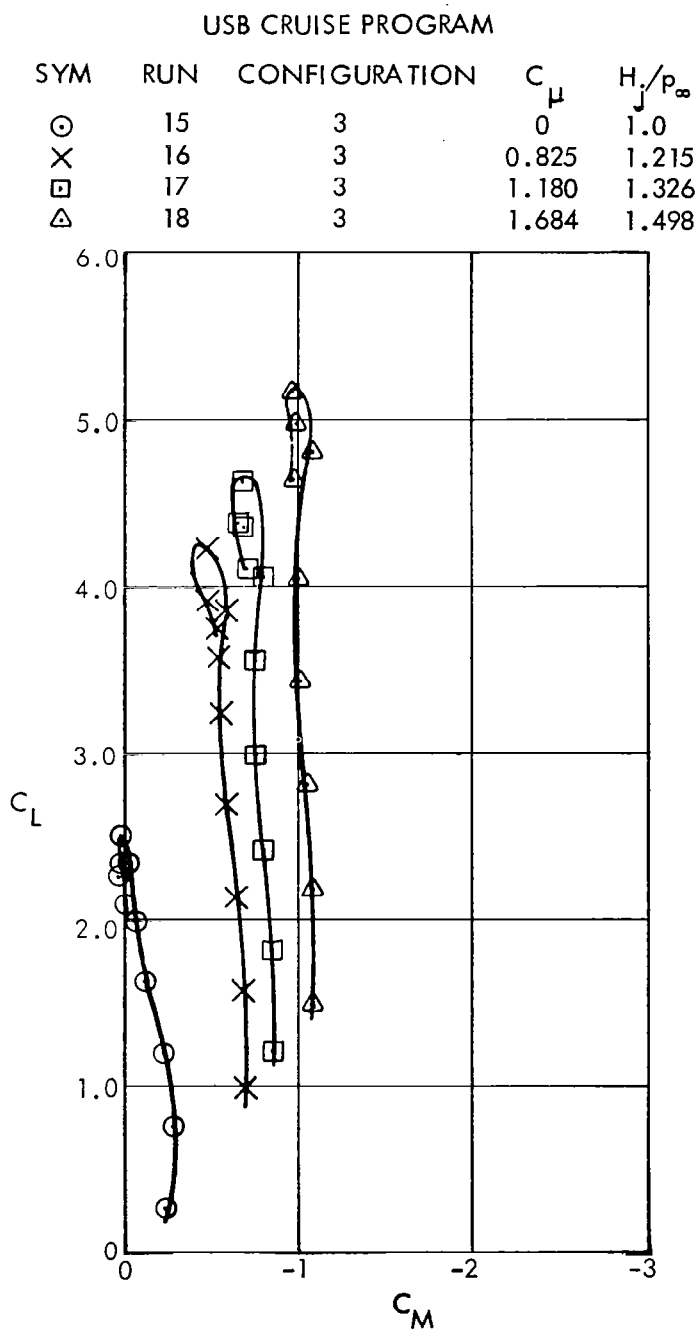


Figure 47. Variation of low speed model lift coefficient with moment coefficient, $q_\infty = 718.2$ N/m$^2$ (15 lb/ft$^2$), $\delta_f = 25^\circ$, Coanda plate

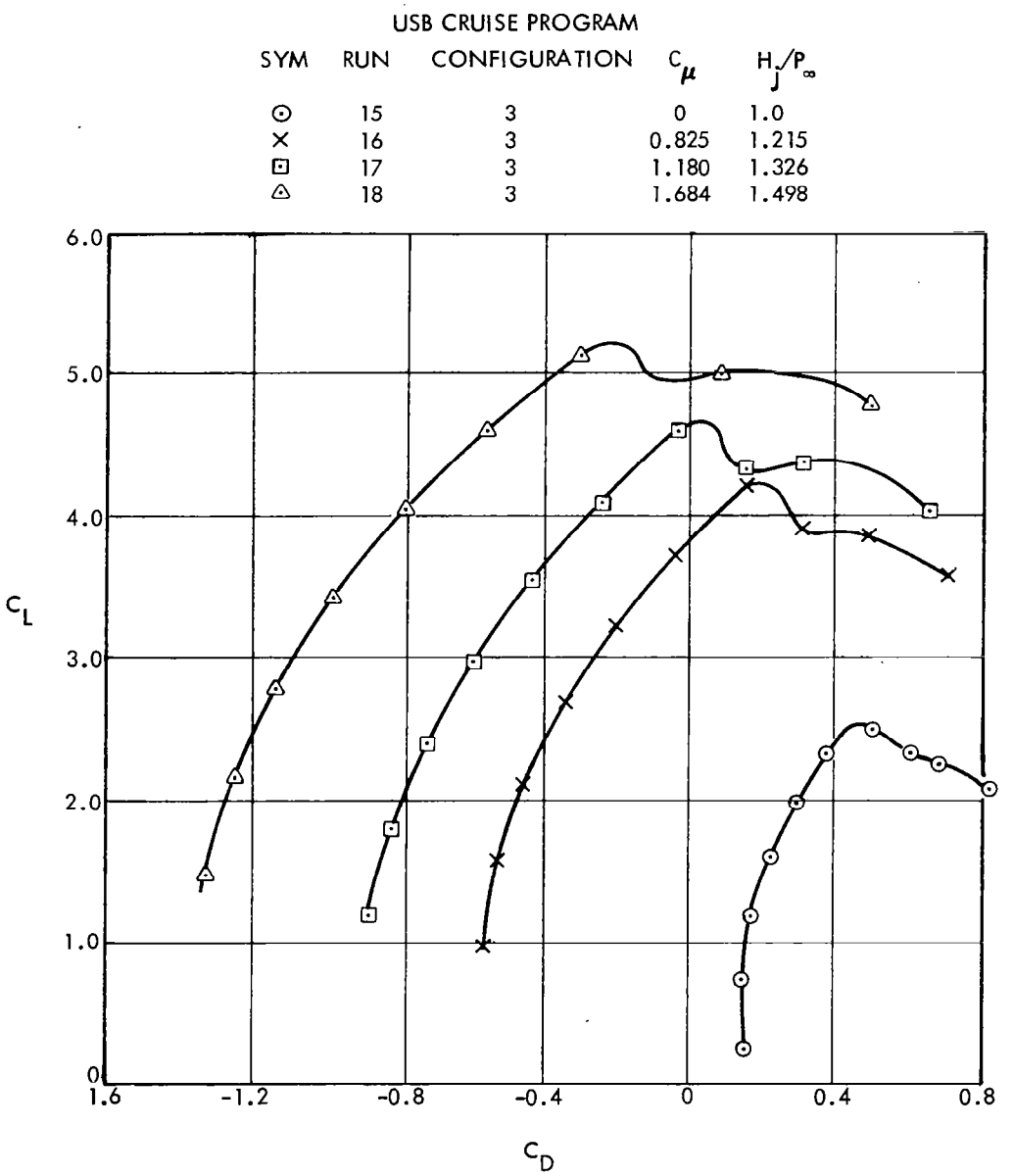


Figure 48. Variation of low speed model lift coefficient with drag coefficient, $q_\infty$ = 718.2N/m$^2$ (15 lb/ft$^2$), $\delta_f$ = 25°, Coanda plate

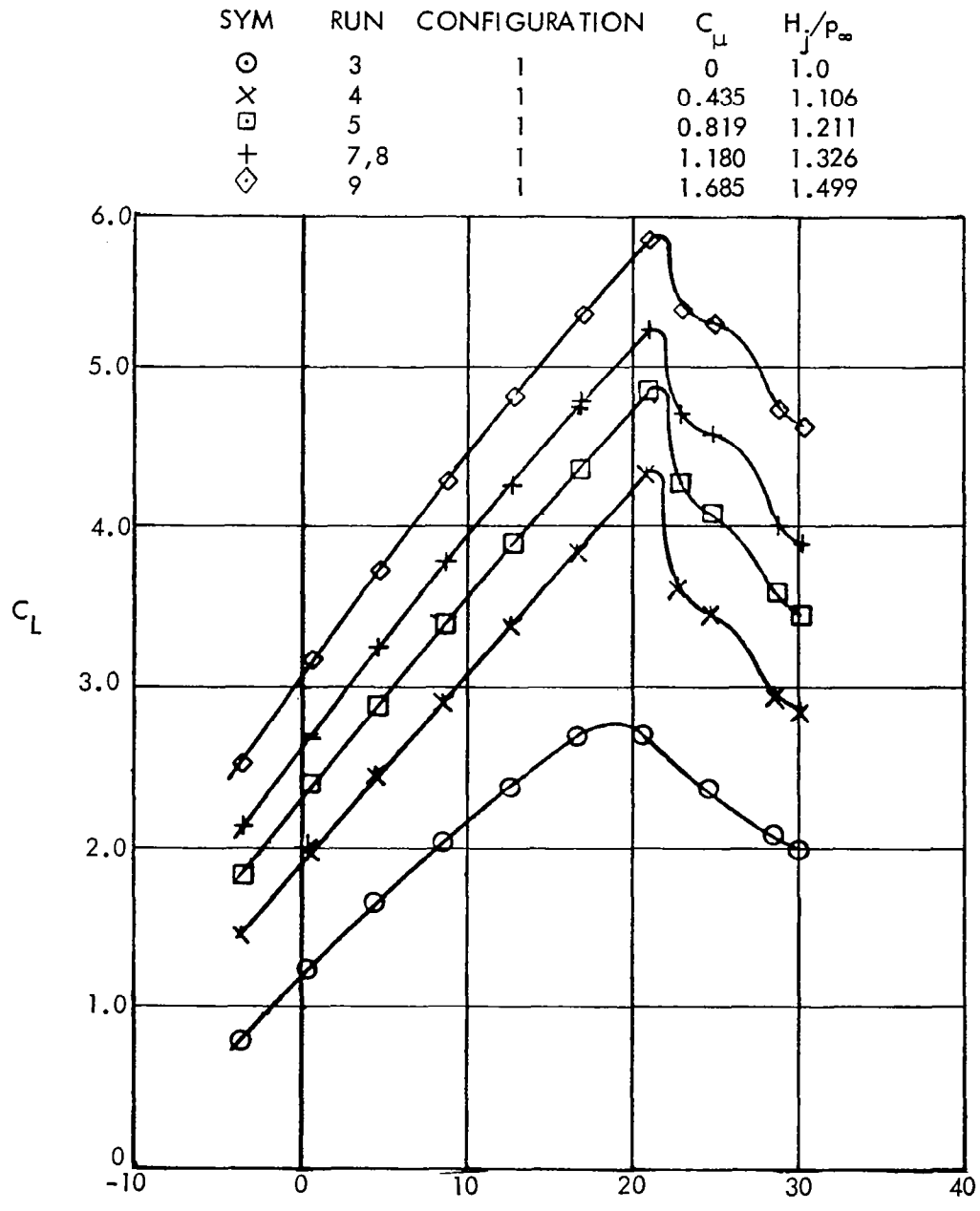


Figure 49. Variation of low speed model lift coefficient with angle of attack, $q_\infty = 718.2$ N/m$^2$ (15 lb/ft$^2$), $\delta_f = 42.5^\circ$, Coanda plate

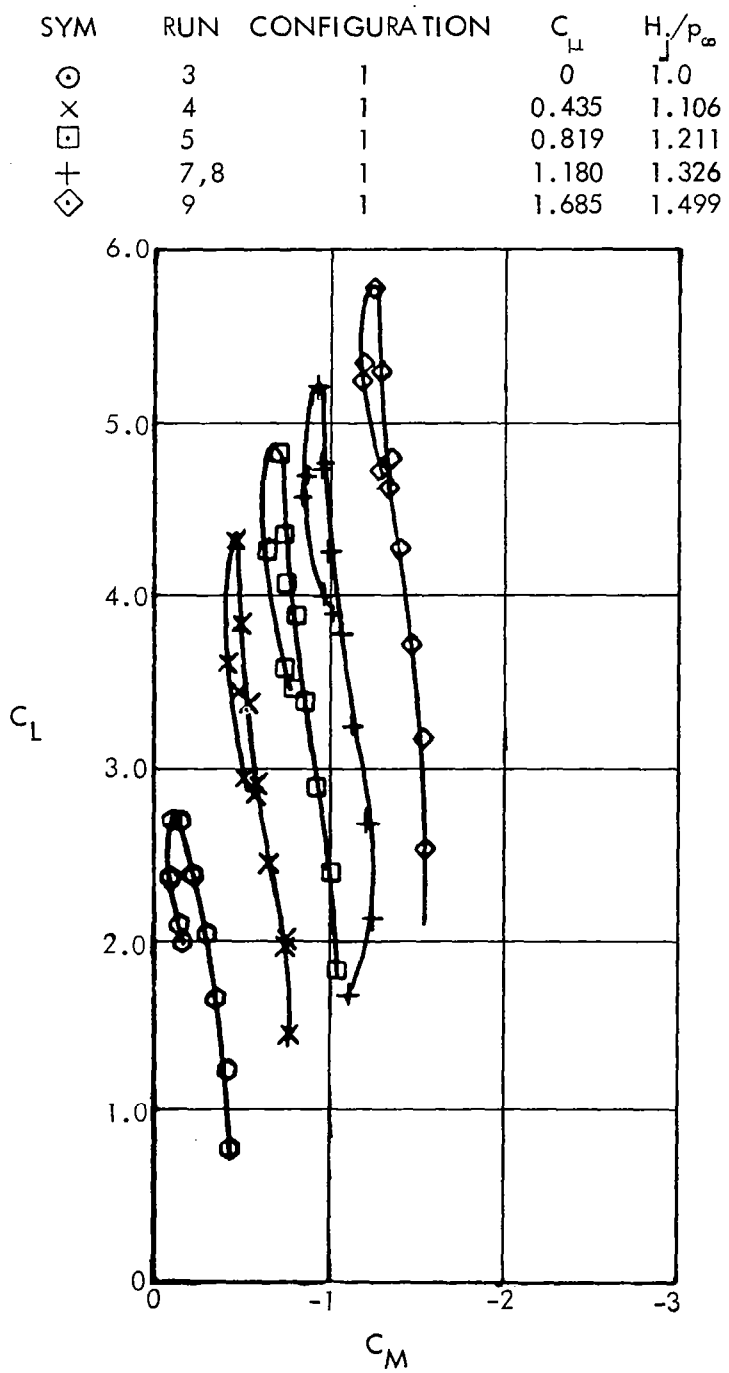


Figure 50. Variation of low speed model lift coefficient with moment coefficient, $q_\infty = 718.2\ N/m^2$ (15 $lb/ft^2$), $\delta_f = 42.5^o$, Coanda plate

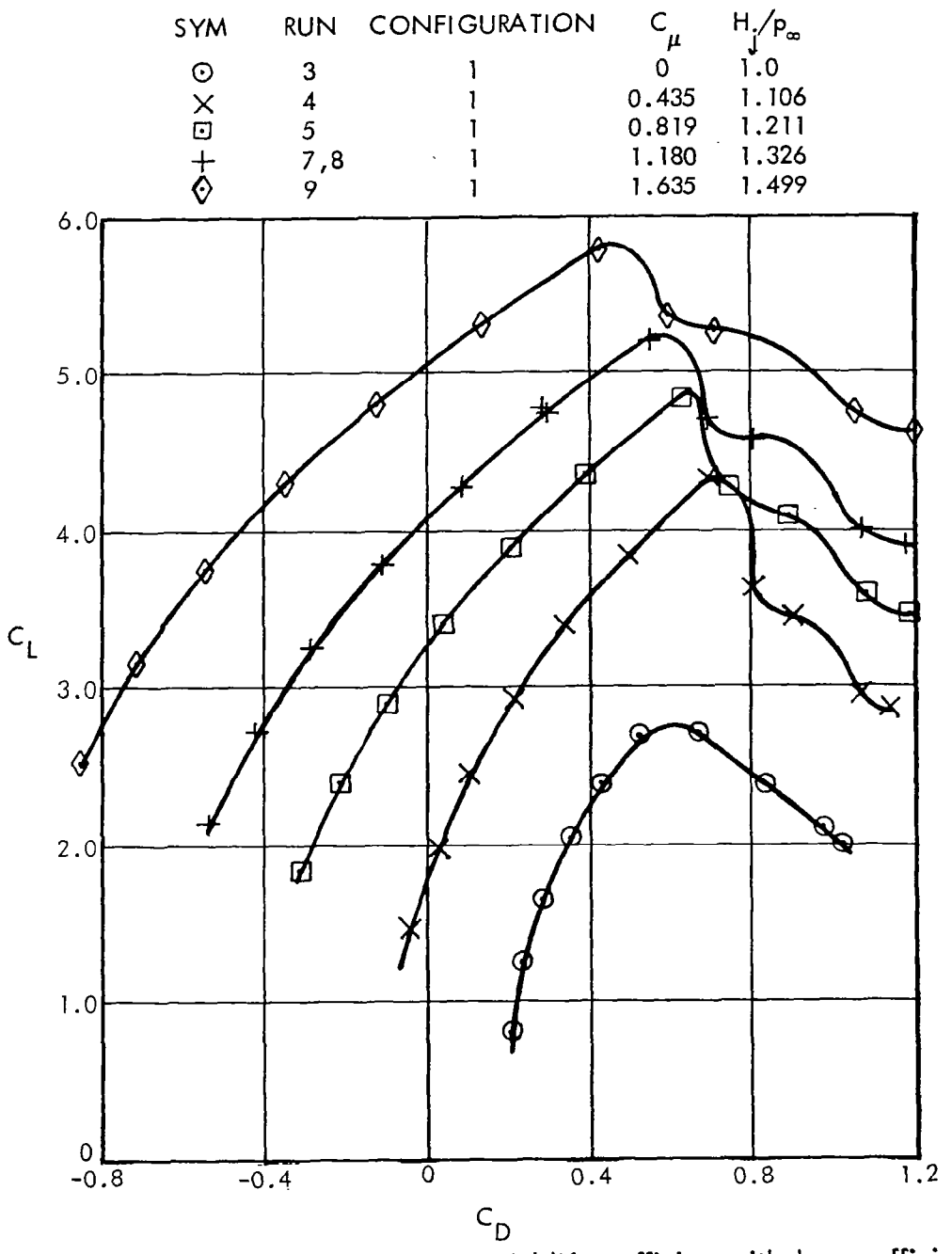


Figure 51. Variation of low speed model lift coefficient with drag coefficient, $q_\infty = 718.2$ N/m$^2$ (15 lb/ft$^2$), $\delta_f = 42.5°$, Coanda plate

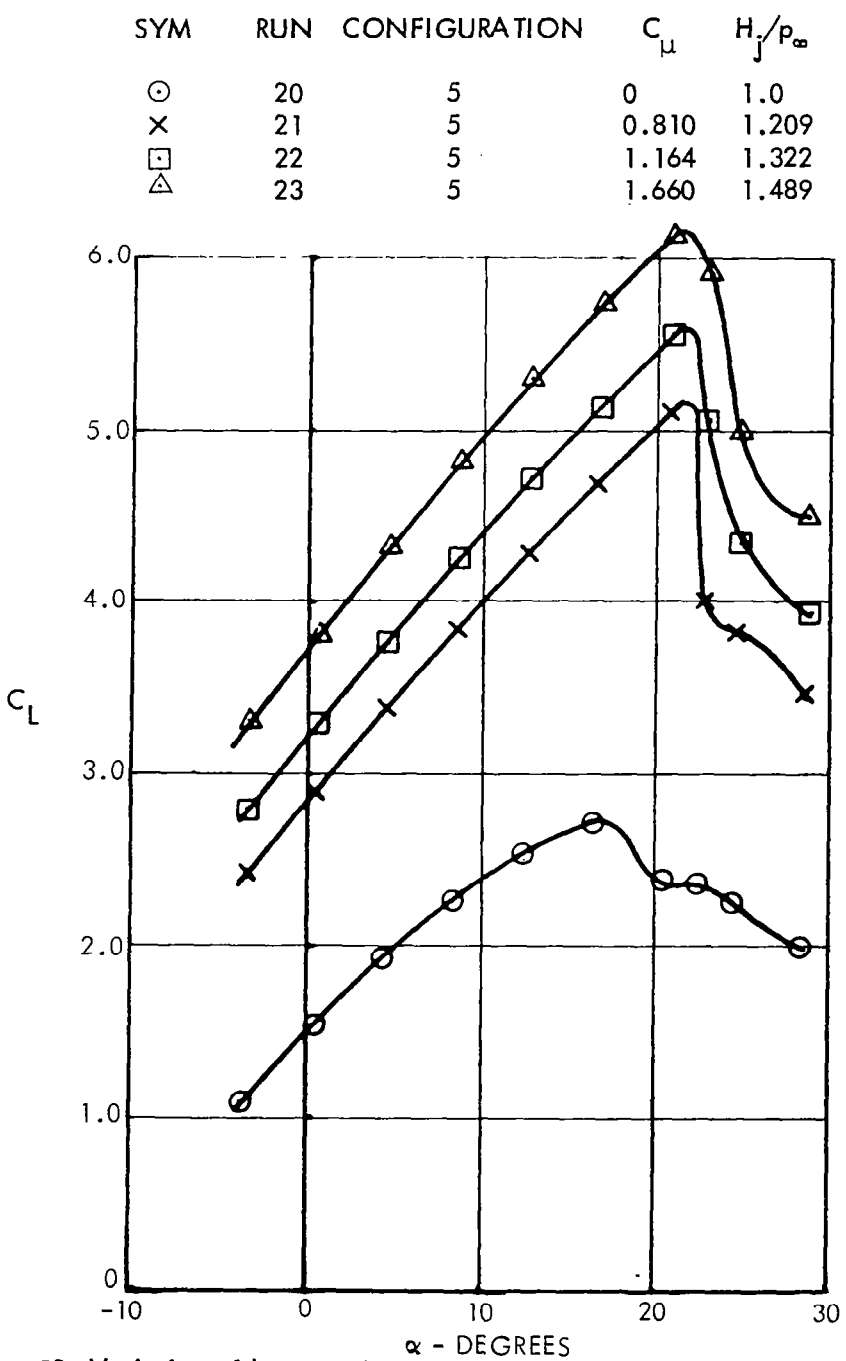


Figure 52. Variation of low speed model lift coefficient with angle of attack, $q_\infty = 718.2$ N/m$^2$ (15 lb/ft$^2$), $\delta_f = 52^\circ$, Coanda plate

| SYM | RUN | CONFIGURATION | $C_\mu$ | $H_j/P_\infty$ |
|---|---|---|---|---|
| ⊙ | 20 | 5 | 0 | 1.0 |
| × | 21 | 5 | 0.810 | 1.209 |
| ⊡ | 22 | 5 | 1.164 | 1.322 |
| △ | 23 | 5 | 1.660 | 1.489 |

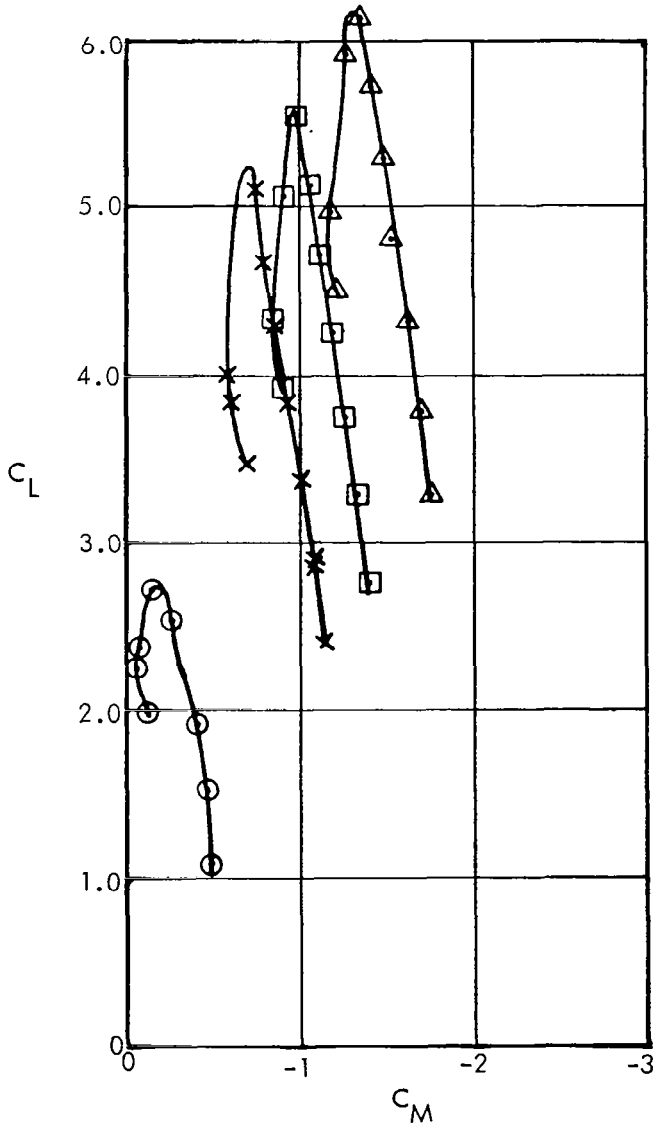


Figure 53. Variation of low speed model lift coefficient with moment coefficient, $q_\infty = 718.2$ N/m$^2$ (15 lb/ft$^2$), $\delta_f = 52^\circ$, Coanda plate

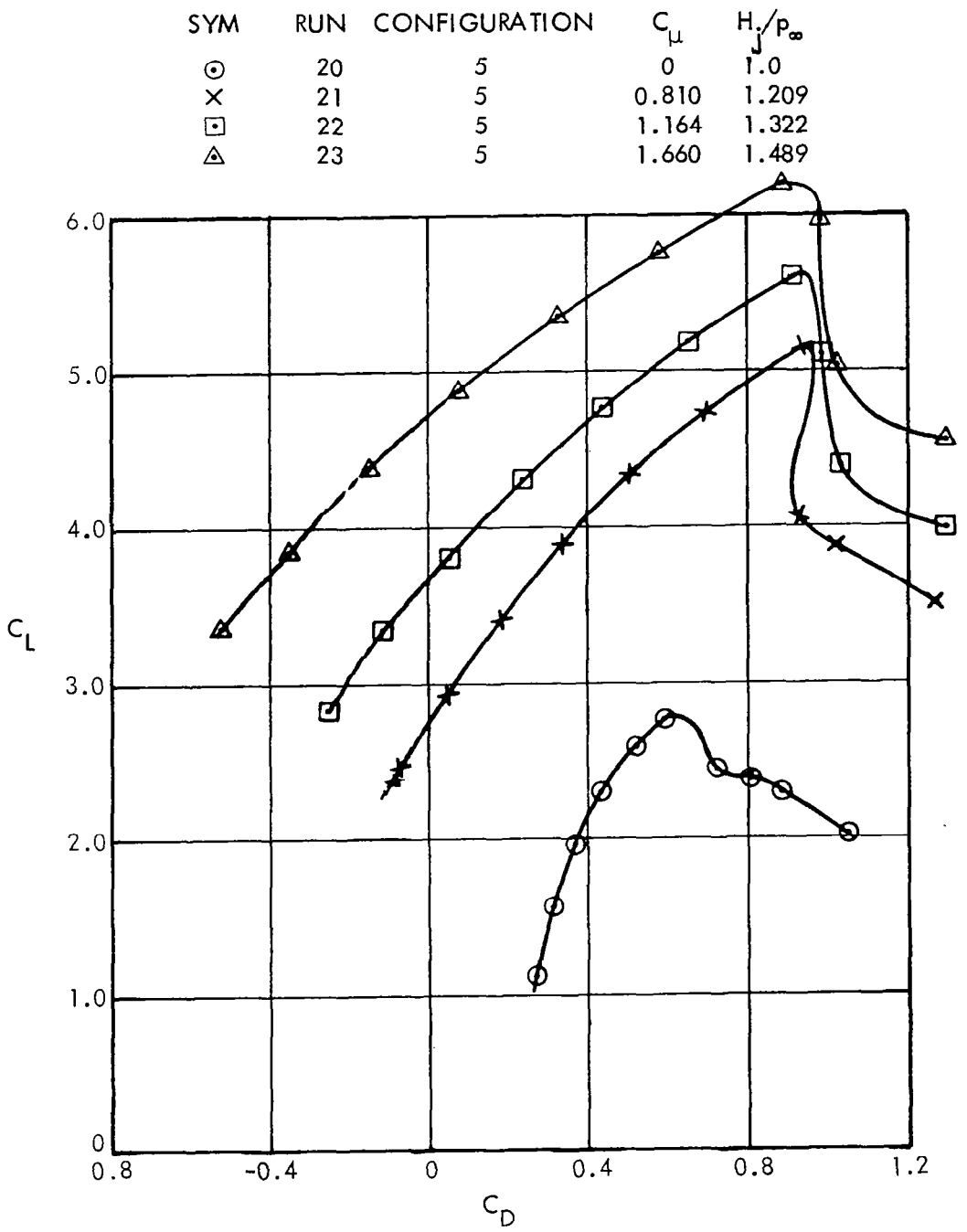


Figure 54. Variation of low speed model lift coefficient with drag coefficient, $q_\infty = 718.2$ N/m$^2$ (15 lb/ft$^2$), $\delta_f = 52^\circ$, Coanda plate

USB CRUISE PROGRAM

| SYM | RUN | CONFIGURATION | $C_\mu$ | $H_j/p_\infty$ |
|---|---|---|---|---|
| ⊙ | 10 | 2 | 0 | 1.0 |
| × | 11 | 2 | 0.815 | 1.209 |
| ⊡ | 12 | 2 | 1.180 | 1.324 |
| △ | 13 | 2 | 1.680 | 1.496 |

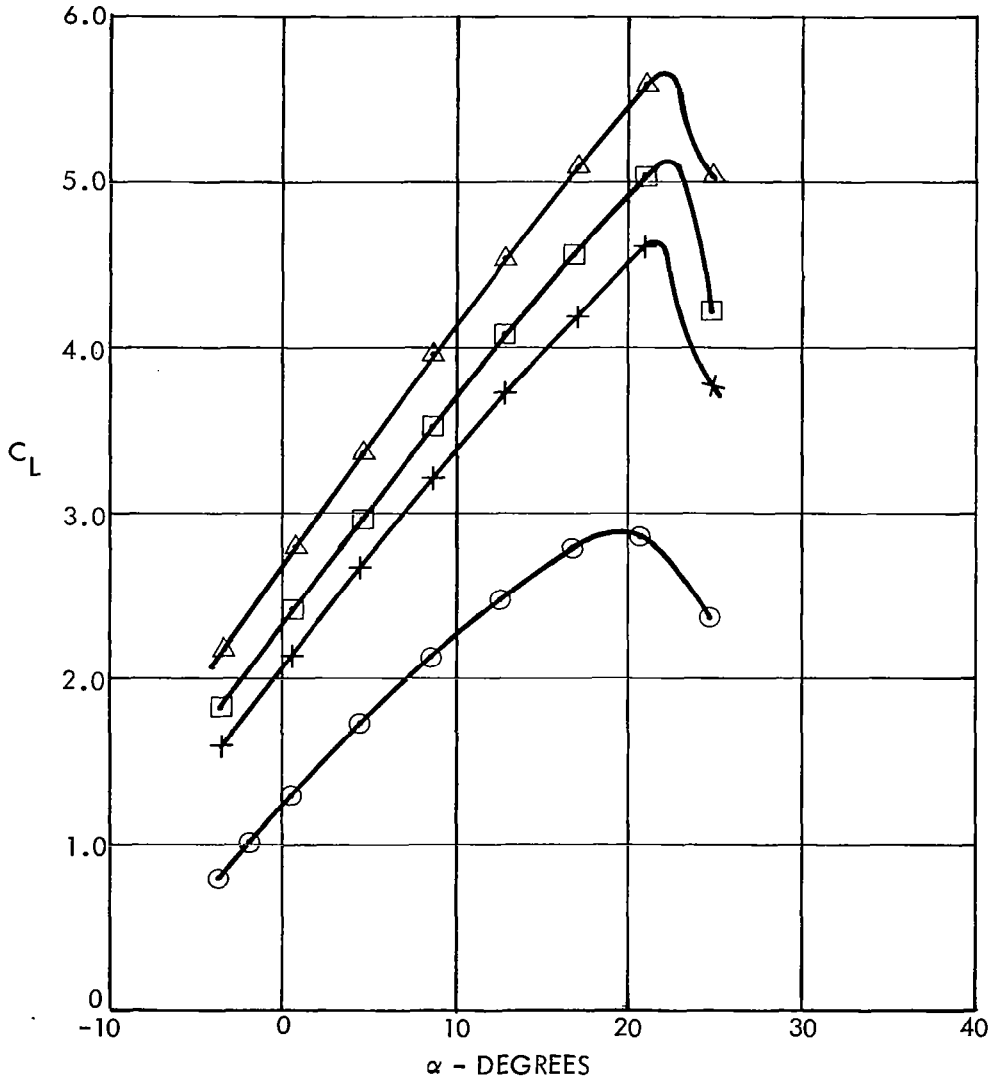


Figure 55. Variation of low speed model lift coefficient with angle of attack, $q_\infty \cong 718.2$ N/m$^2$ (15 lb/ft$^2$), $\delta_f = 42.5°$, taped slots

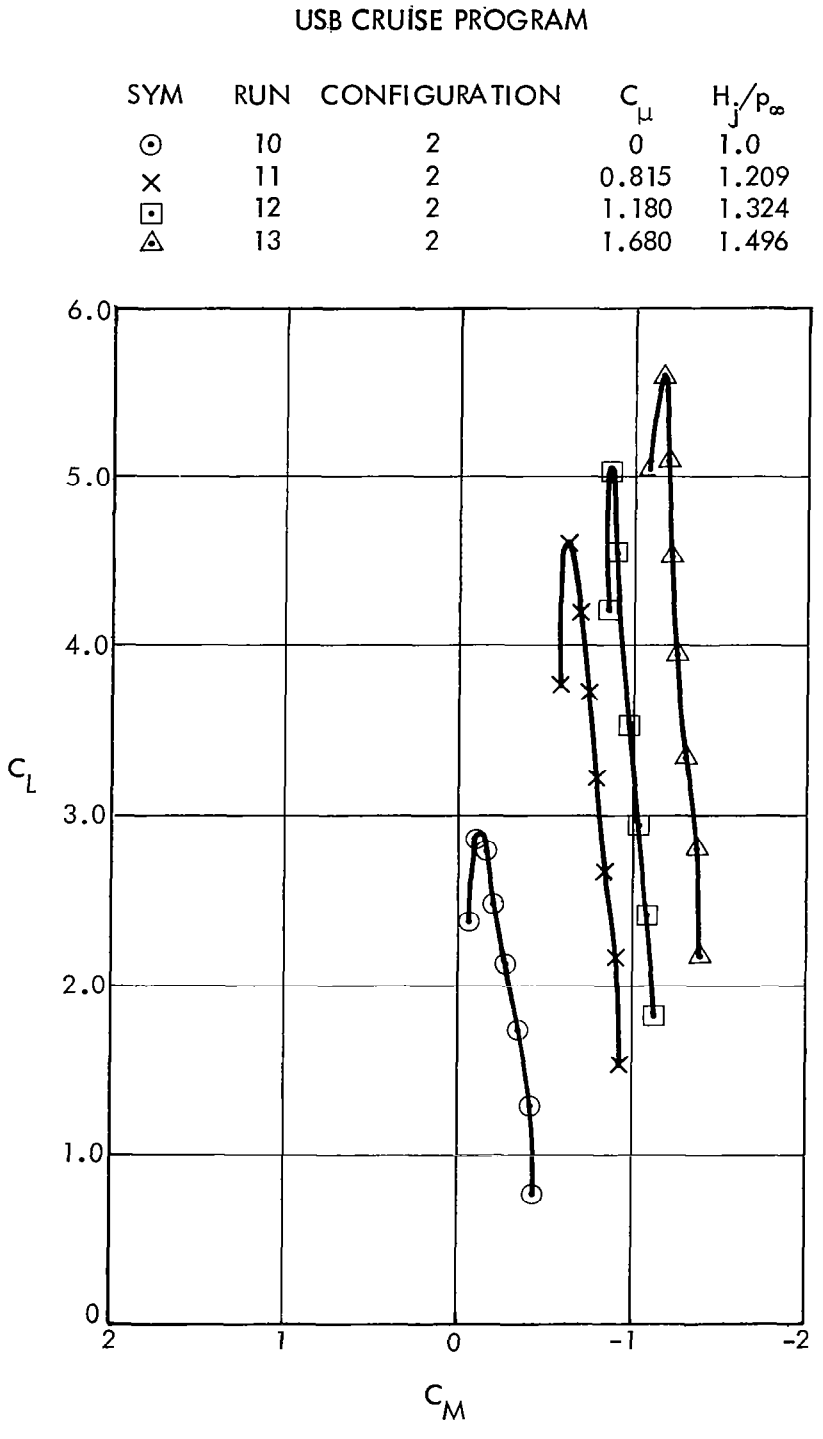


Figure 56. Variation of low speed model lift coefficient with moment coefficient, $q_\infty = 718.2$ N/m$^2$ (15 lb/ft$^2$), $\delta_f = 42.5^\circ$, taped slots

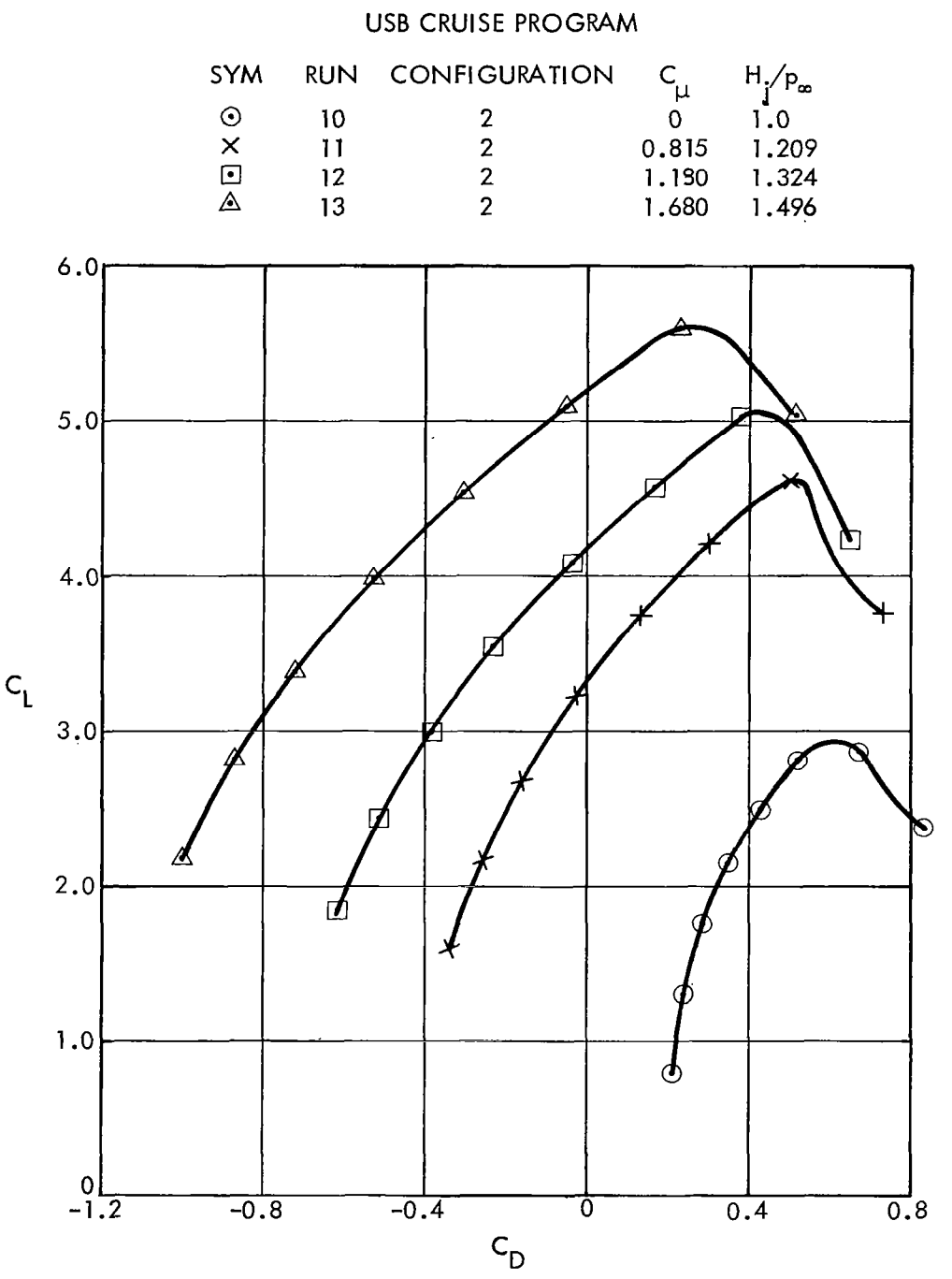


Figure 57. Variation of low speed model lift coefficient with drag coefficient, $q_\infty = 718.2$ N/m$^2$ (15 lb/ft$^2$), $\delta_f = 42.5^\circ$, taped slots

5.2.4 Flow Visualization - Oil-flow photographs of the model at several test conditions are provided in Figure 58 through 61. While a substantial number of such photographs were taken during the investigation, those shown illustrate typical flow-field behavior. No significant variations in either the wing or jet flow, such as jet detachment or extensive entrainment effects, were observed other than those indicated in the photographs provided.

## 6.0 HIGH-LIFT DISCUSSION

Powered lift test results obtained for alternate systems installed on the same model will be compared with the subject low speed, high lift data as presented in the previous section. Additionally, a comparison will be made with upper surface blowing (USB) test results from other facilities. Finally, since the objective of the tests was to verify estimated performance on the Task III aircraft design, an analysis of the test results will show the relationship between the model performance and that required by the full-scale design. In this phase of the discussion, extensive use will be made of analytical syntheses of the model and the Task III design to circumvent the geometric differences between the two. Notable in this regard are the high aspect ratio wing (10) of the Task III airplane relative to that of the model (7.7) and the four-engine arrangement of the full-scale design versus the two-engine test article.

### 6.1 High-Lift Comparison, Alternate Systems

Inasmuch as the model used in the subject tests represented a basic test vehicle utilized for a variety of powered system tests, an opportunity is afforded for direct comparisons of resulting high-lift performance. Figure 62 compares the two-engine USB-test results with data obtained on a four-engine externally-blown flap configuration. The test hardware (i.e., ejector units, trailing-edge flaps, high-camber leading-edge device) is essentially the same in both instances, except that the externally blown flap (EBF) data were obtained on a wing more highly swept (25 degrees) than the USB-wing (15 degrees). At the lower angles of attack, the four-engine EBF-system with the

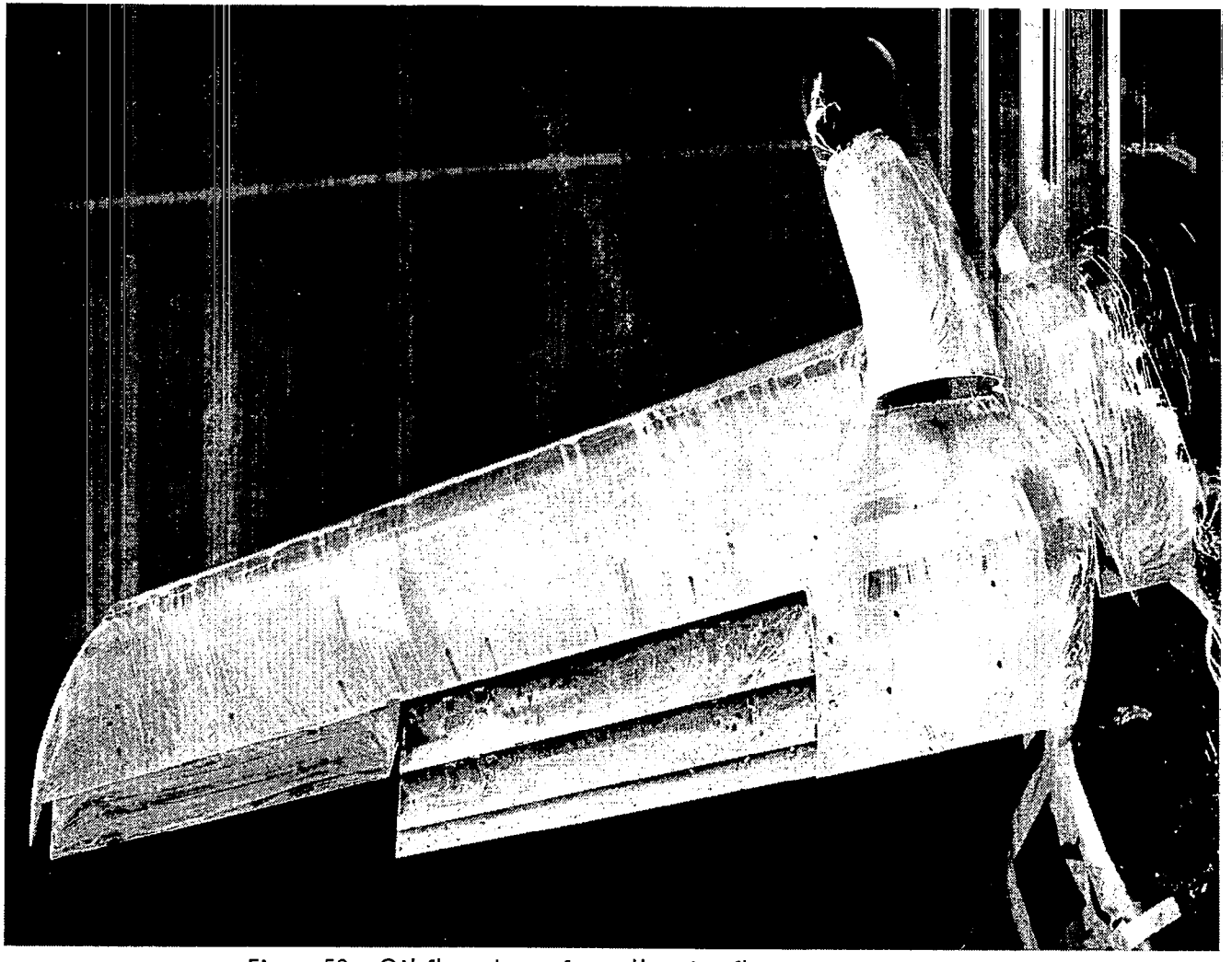

Figure 58. Oil flow photo of nacelle-wing flow pattern,
$q_\infty = 718.2\ N/m^2$ (15 $lb/ft^2$), $\alpha = 10^\circ$, $C_\mu = 0.82$, $\delta_f = 42.5^\circ$

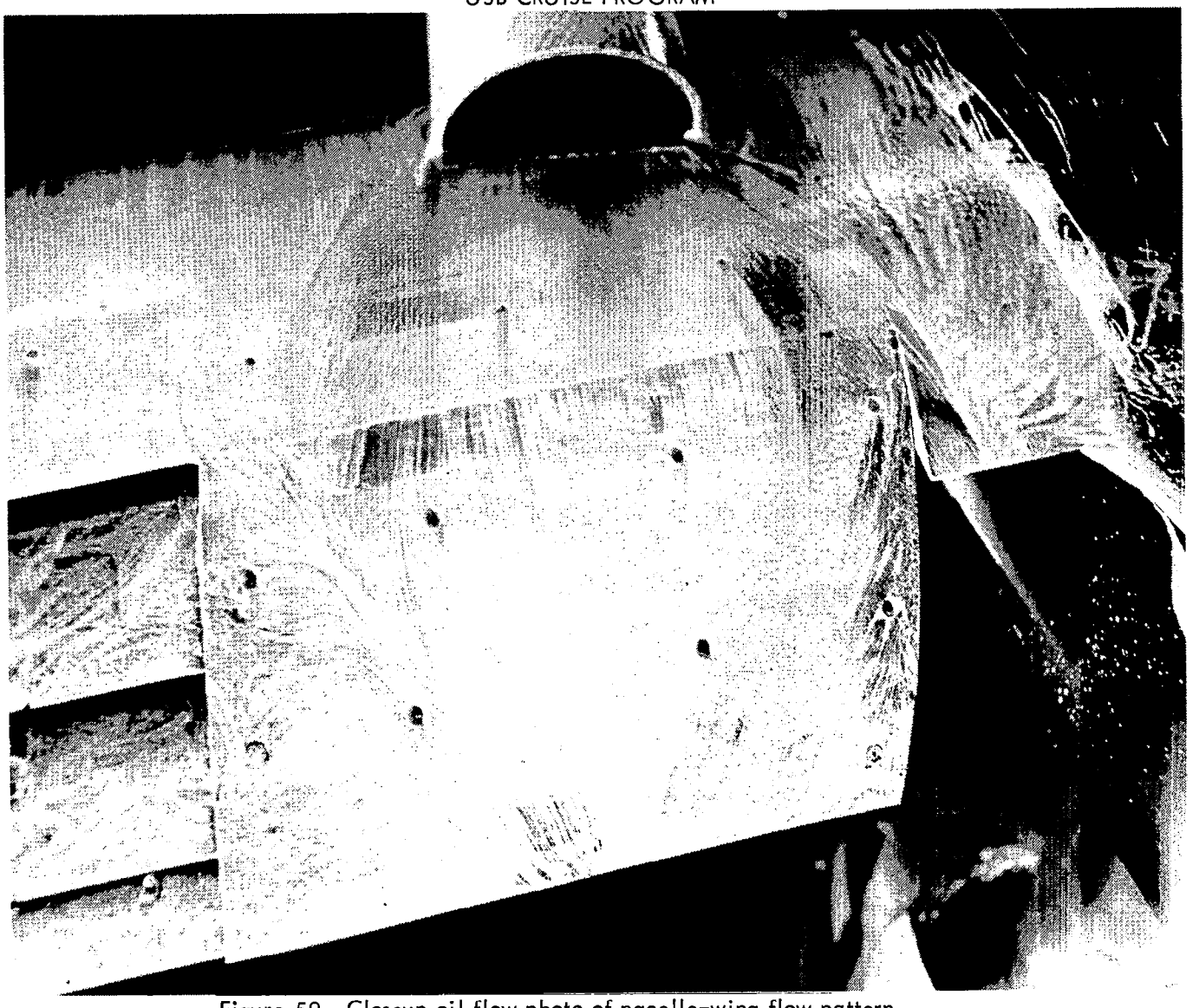

Figure 59. Closeup oil flow photo of nacelle-wing flow pattern, $q_\infty = 718.2$ N/m$^2$ (15 lb/ft$^2$), $\alpha = 10^\circ$, $C_\mu = 0.82$, $\delta_f = 42.5^\circ$

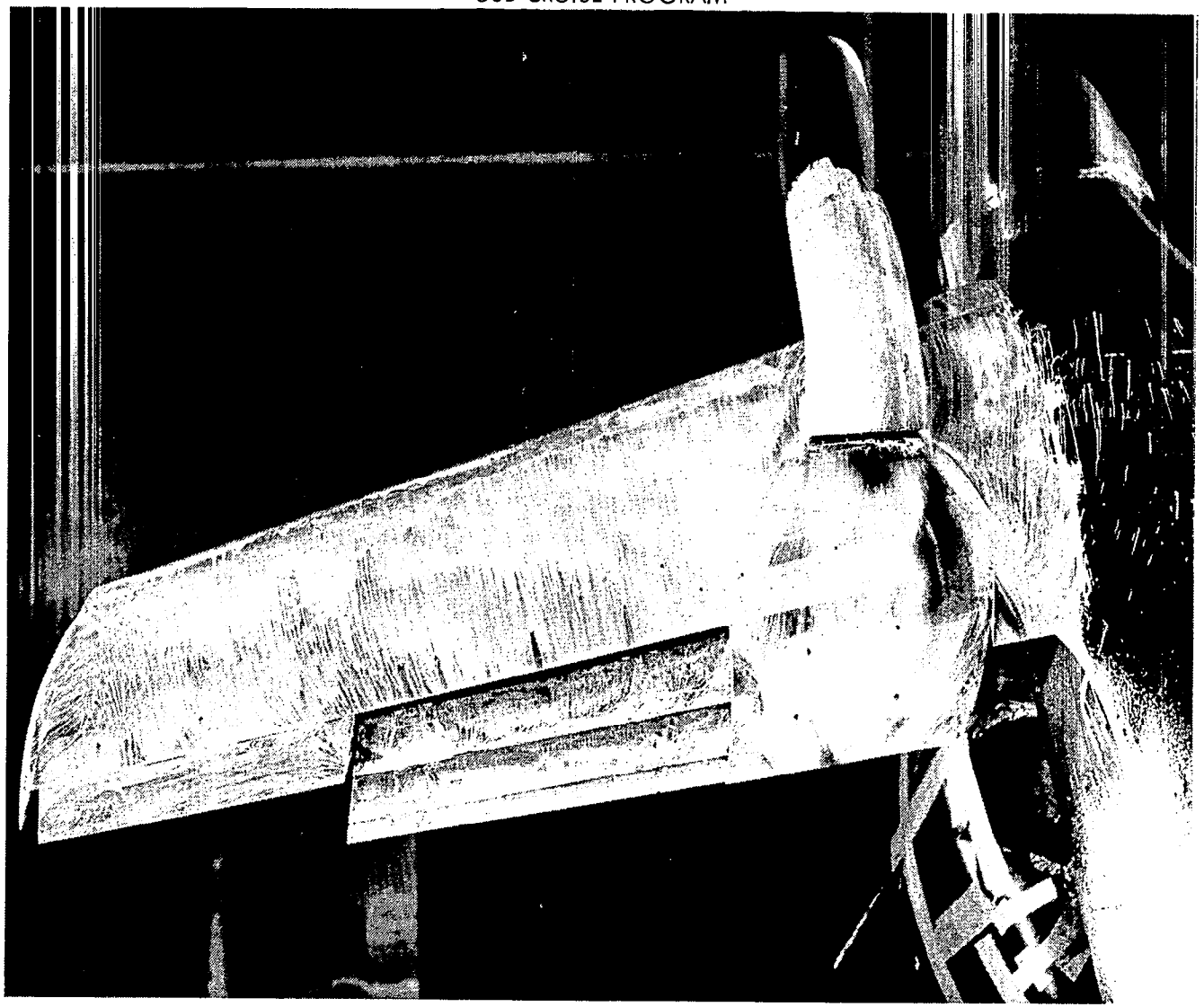

Figure 60. Oil flow photo of nacelle-wing flow pattern,
$q_\infty = 718.2\ N/m^2$ (15 $lb/ft^2$), $\alpha = 10^\circ$, $C_\mu = 1.66$, $\delta_f = 42.5^\circ$

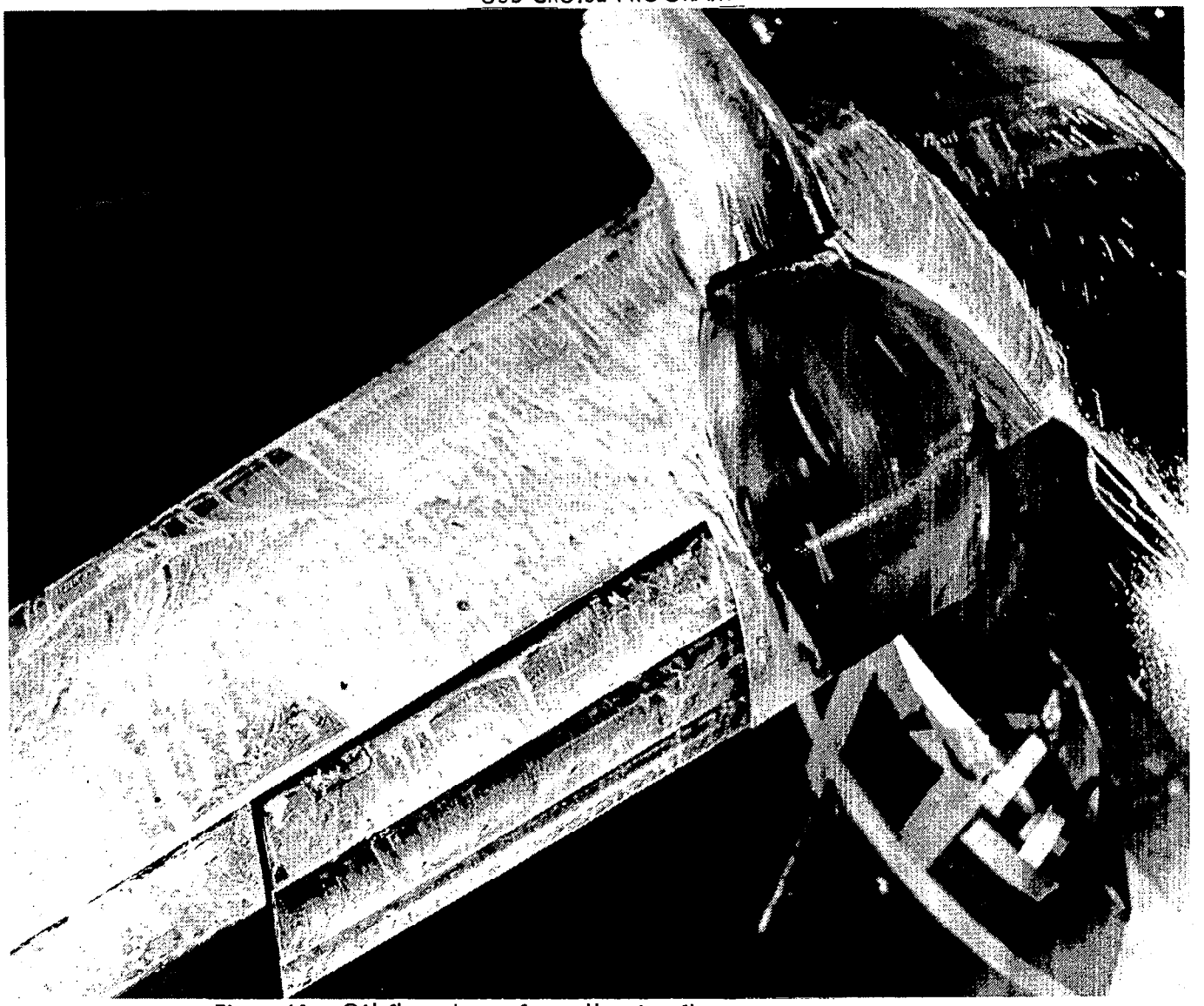

Figure 61. Oil flow photo of nacelle wing flow pattern, $q_\infty = 718.2\ N/m^2$ (15 $lb/ft^2$), $\alpha = 20^\circ$, $C_\mu = 1.66$, $\delta_f = 52.0^\circ$

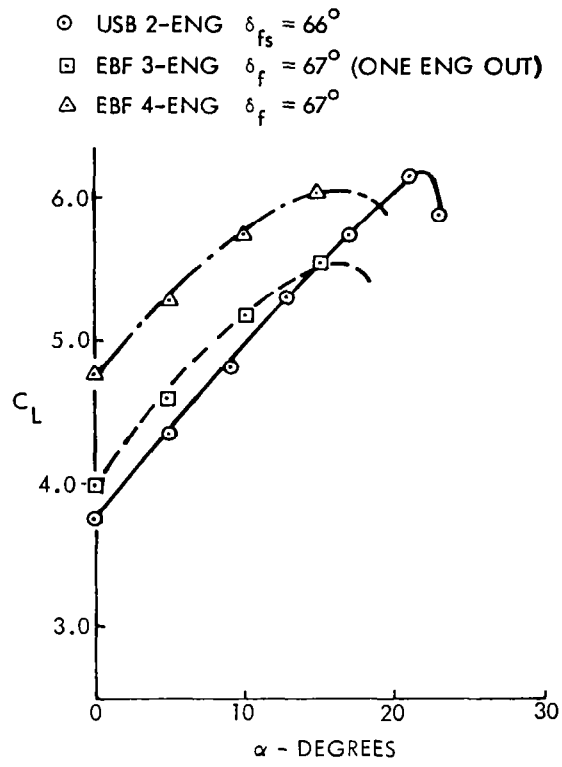


Figure 62. USB/EBF performance comparison, tail-off configuration, $C_\mu = 1.66$.

greater span of blown wing produces a higher lift coefficient. The sensitivity of this system to number of engines is illustrated by the three-engine (engine-out) performance which approaches that of the two-engine USB. In terms of maximum lift, the USB-system provides about the same $C_{L_{MAX}}$ as the four-engine EBF for the thrust coefficient represented ($C_T$ = 1.66). As will be noted in a later paragraph, going to a four-engine USB-installation requires a very careful tailoring of the nacelle/wing leading-edge juncture in order to realize the improved performance associated with the better spanwise distribution of the four-engine blowing. The data of Figure 62 do illustrate, however, that the potential of the USB system for powered-lift generation is competitive with that of a similar EBF arrangement. It should also be noted that the USB-test article represented an unrefined configuration, in contrast to the EBF model for which considerable development testing has been performed. Improved USB performance would be expected where appropriate refinements are made.

## 6.2 Test Data Comparisons, Different Facilities

A comparison of the present USB high lift performance data with similar data obtained on a two-engine USB arrangement is shown in Figure 63. The comparative results are taken from Reference 1 representing large-scale tests of the USB system using JT15D-1 turbofan engines. For a typical landing flap case, the subject USB test results are shown to compare favorably with the large-scale results, although the referenced results represented a wider nozzle, relative to wing span, than does the present case. Comparisons with the more optimized test results from the referenced investigations are shown in Figure 64. Both maximum lift and lift at $\alpha$ = 0 degrees are shown to be less than that found in the large-scale results by $\Delta C_L \simeq 0.5$. This is believed to be indicative of the performance improvements which could be readily obtained from the present system if similar refinements were made.

## 6.3 Powered-Lift Synthesis

For use as a correlation and prediction tool, the Lockheed-Georgia powered lift computer program was employed as an intermediate step between the

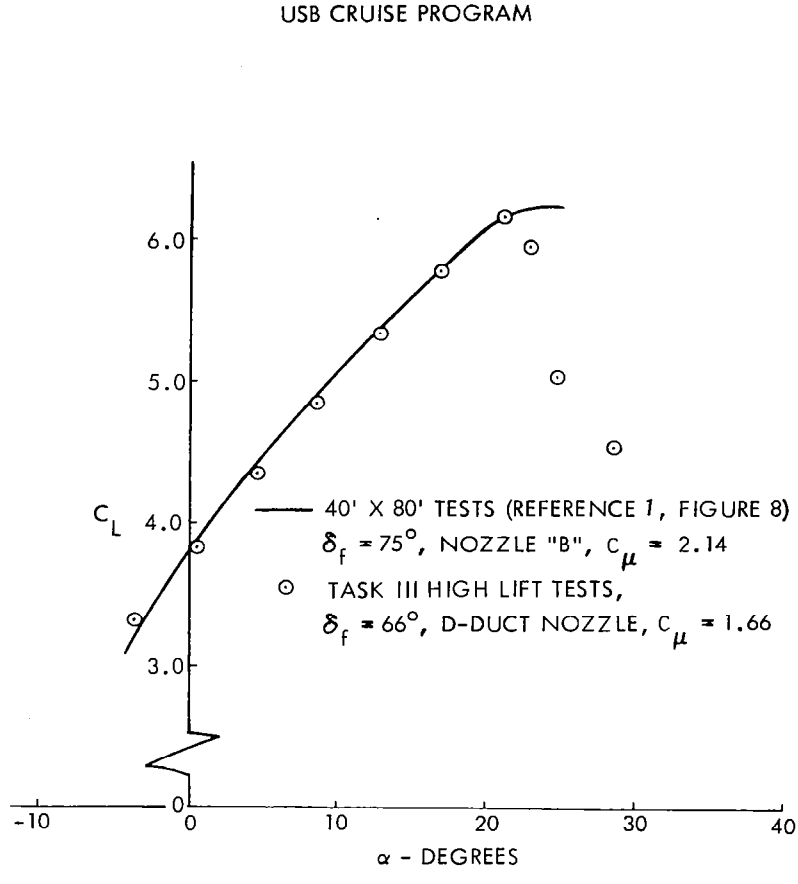


Figure 63. USB performance comparison, two-engine configurations

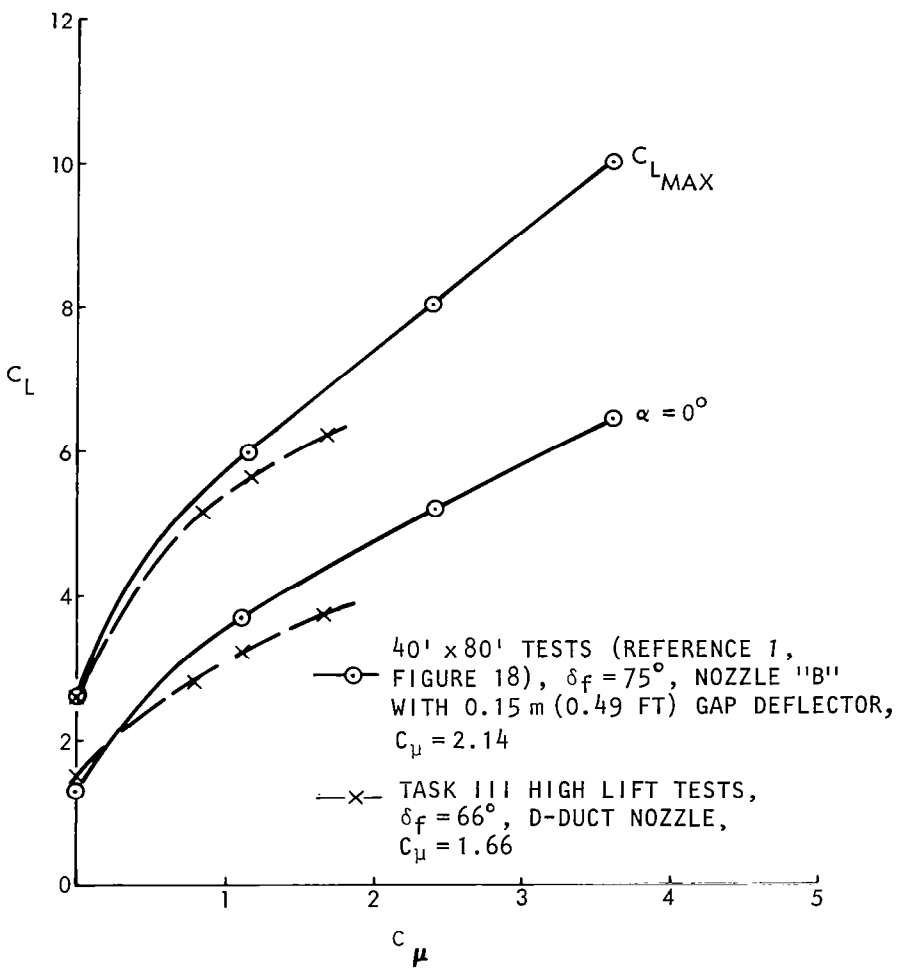


Figure 64. Effect of thrust coefficient on USB performance comparison, two-engine configurations

low-speed test and the full-scale Task III aircraft. This program has been successfully utilized for the design and analysis of a wide variety of powered-lift systems. Figures 65 through 68 show typical examples of this usage and include the Reference 1 USB test results. Good correlation is shown for both lift and drag with the experimental results for the various systems. Use of this program to predict the present experimental configuration performance is represented in Figure 69. The lift shows excellent agreement with the test data; the test drag as shown, when corrected for the ram drag of the ejector units ($\Delta C_D \simeq 0.10$) also correlates well with the program.

Employing the same computer program for predicting the high-lift performance of the Task III aircraft provides the comparison shown in Figure 70. In formulating the analytical results, several refinements were observed. First, the theoretical data were trimmed according to the calculated pitching moments ($\Delta C_M = -0.23$). Secondly, a lift penalty was imposed as representative of four-engine interference effects found in the Reference 2 investigation. While the referenced documents indicated that local unsweeping of the leading-edge between nacelles and nacelle/fuselage could recover most of this penalty, it was judged that this approach may not be compatible with good cruise performance without highly complex leading-edge deployment devices. Accordingly, this penalty was accepted in view of the preliminary nature of the Task III design. Finally, a lift penalty was imposed ($\Delta C_L \simeq 0.3$) to represent a quick-acting, slot-opening device for engine-out conditions. This penalty reflected test results with the Coanda plate removed and with the slot openings behind the nacelles covered on the bottom surface of the flaps (see Figure 39 and compare the data of Figures 49 and 55). The data of Figure 70 shows that the initial Task III high-lift performance used in the parametric sizing programs is in basic agreement with the analytical results after the foregoing refinements were made. The indications are that in the lower blowing range ($C_\mu = 0.6$), slightly better performance could have been projected in the parametric program, although the results, in terms of aircraft size or mission performance, would be negligible. A three-view sketch of the Task III design is given in Figure 71.

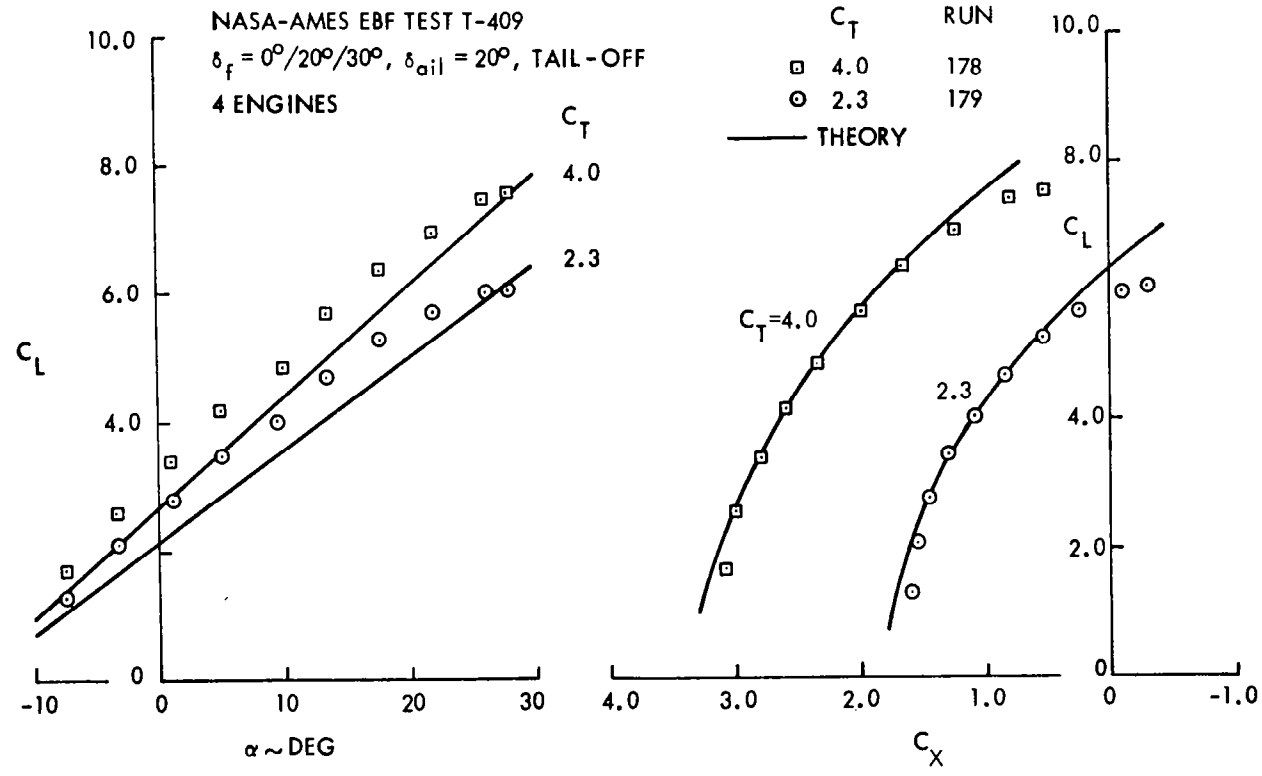


Figure 65. Correlation of theoretical and experimental longitudinal aerodynamic characteristics for a NASA Ames tested high-wing EBF STOL configuration

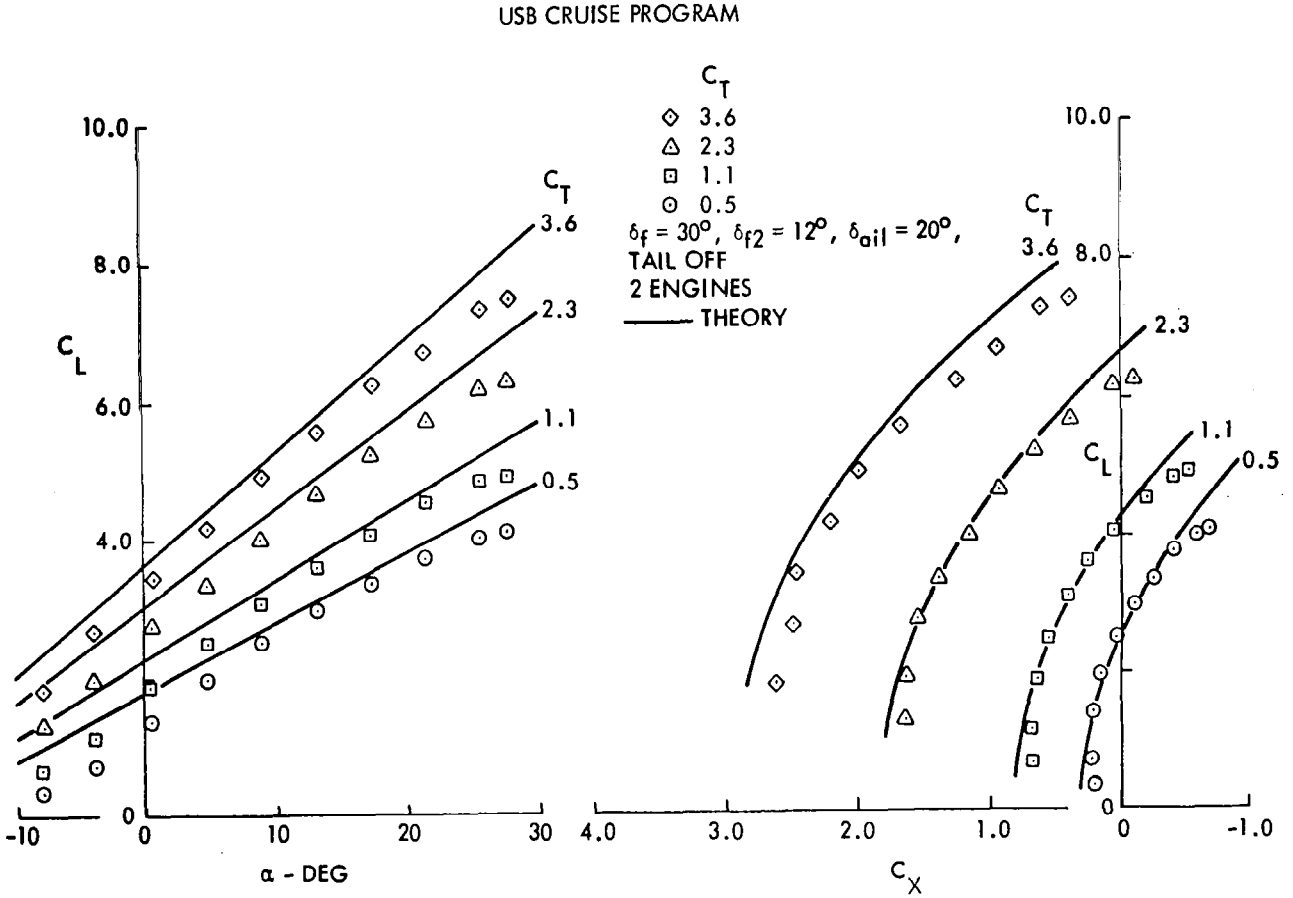


Figure 66. Correlation of theoretical and experimental longitudinal aerodynamic characteristics for a NASA Ames tested high-wing USB STOL configuration

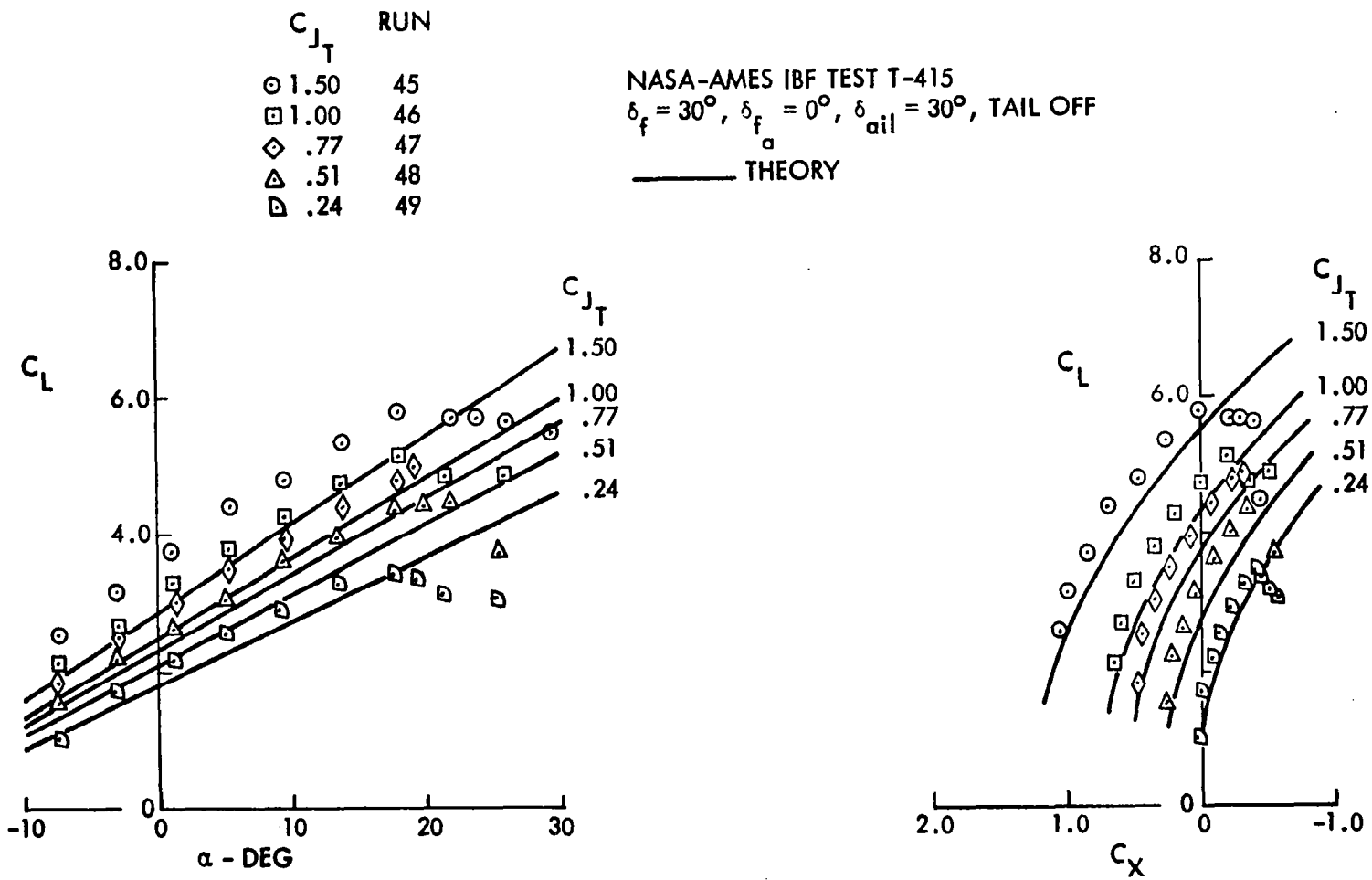


Figure 67. Correlation of theoretical and experimental longitudinal aerodynamic characteristics for a NASA Ames tested high-wing IBF STOL configuration

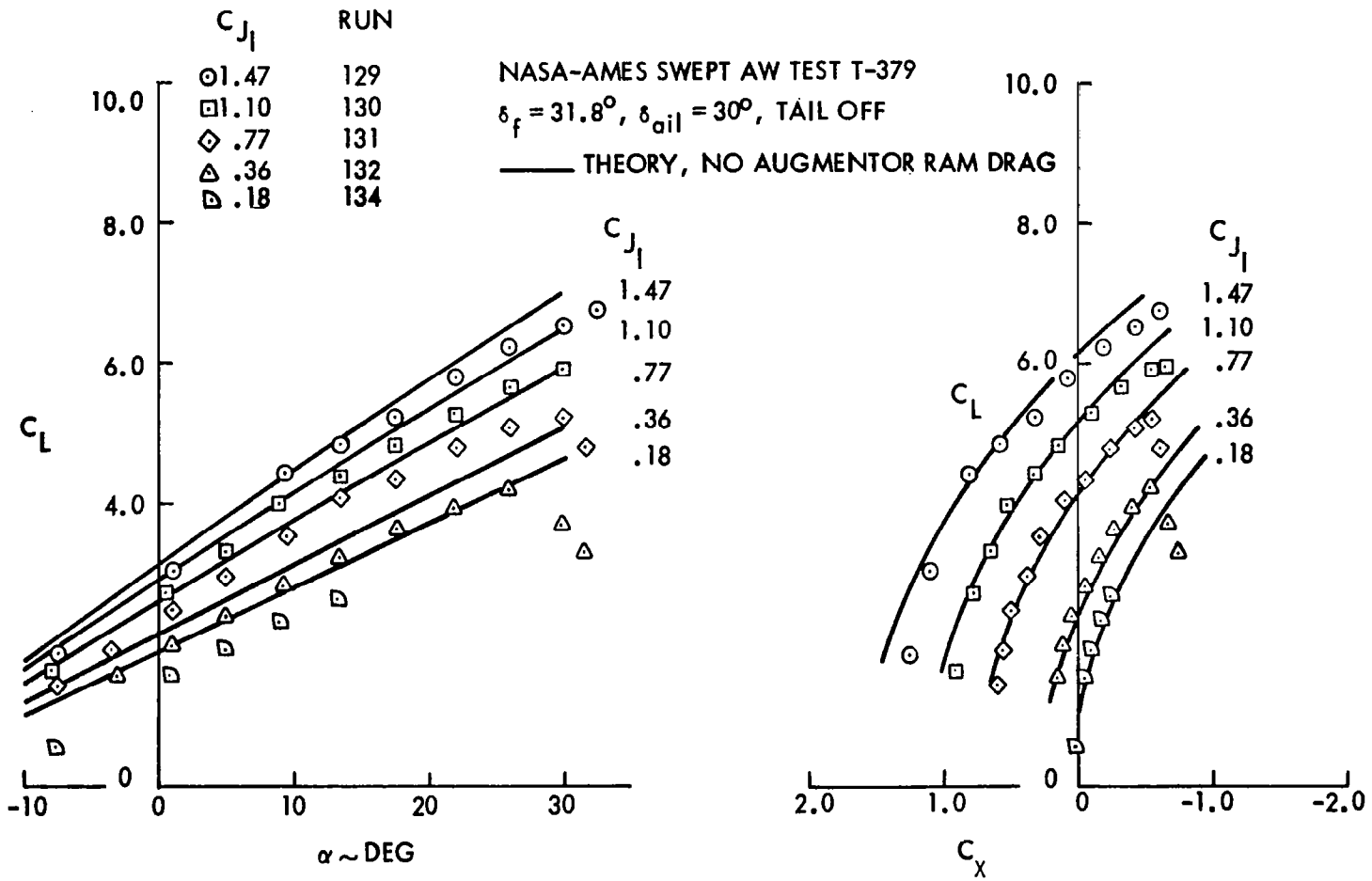


Figure 68. Correlation of theoretical and experimental longitudinal aerodynamic characteristics for a NASA Ames tested high-wing AW STOL configuration

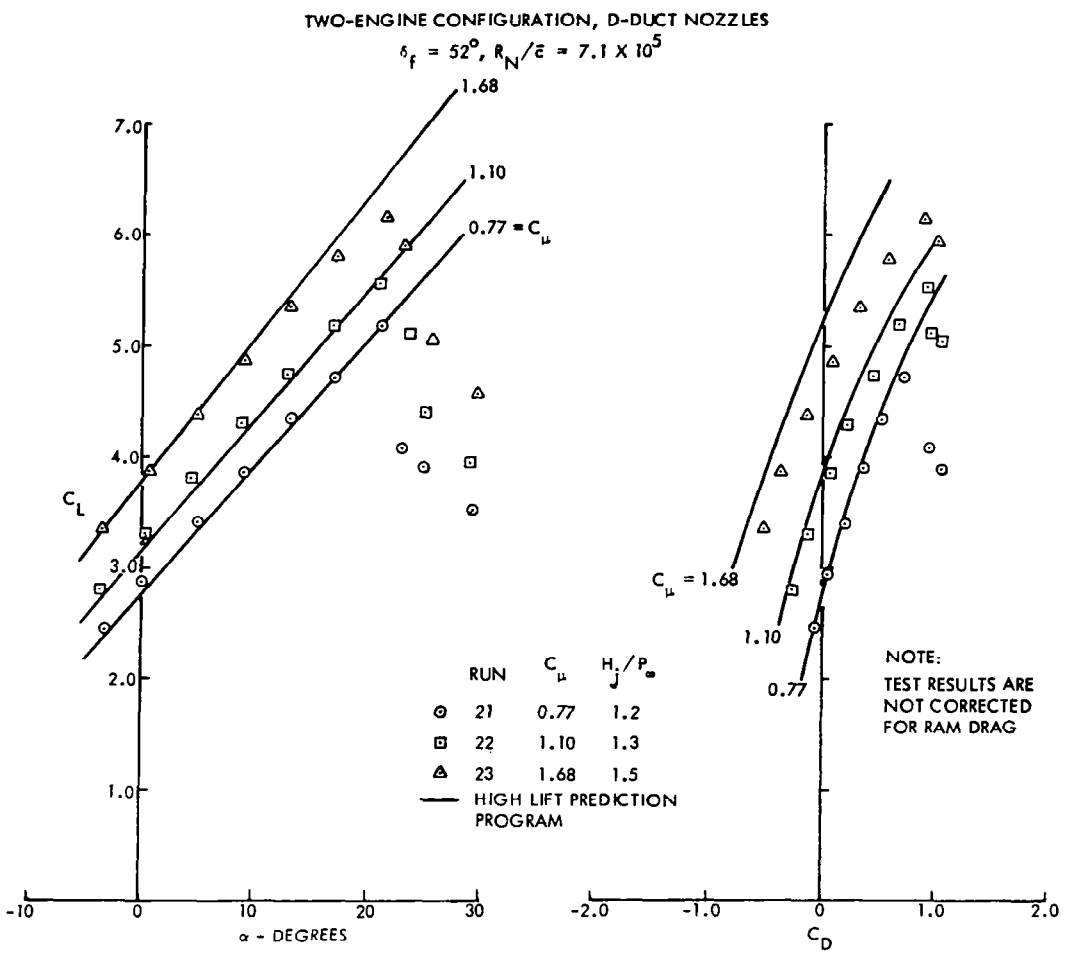


Figure 69. Correlation of theoretical and experimental high-lift performance, USB low speed model, tail off

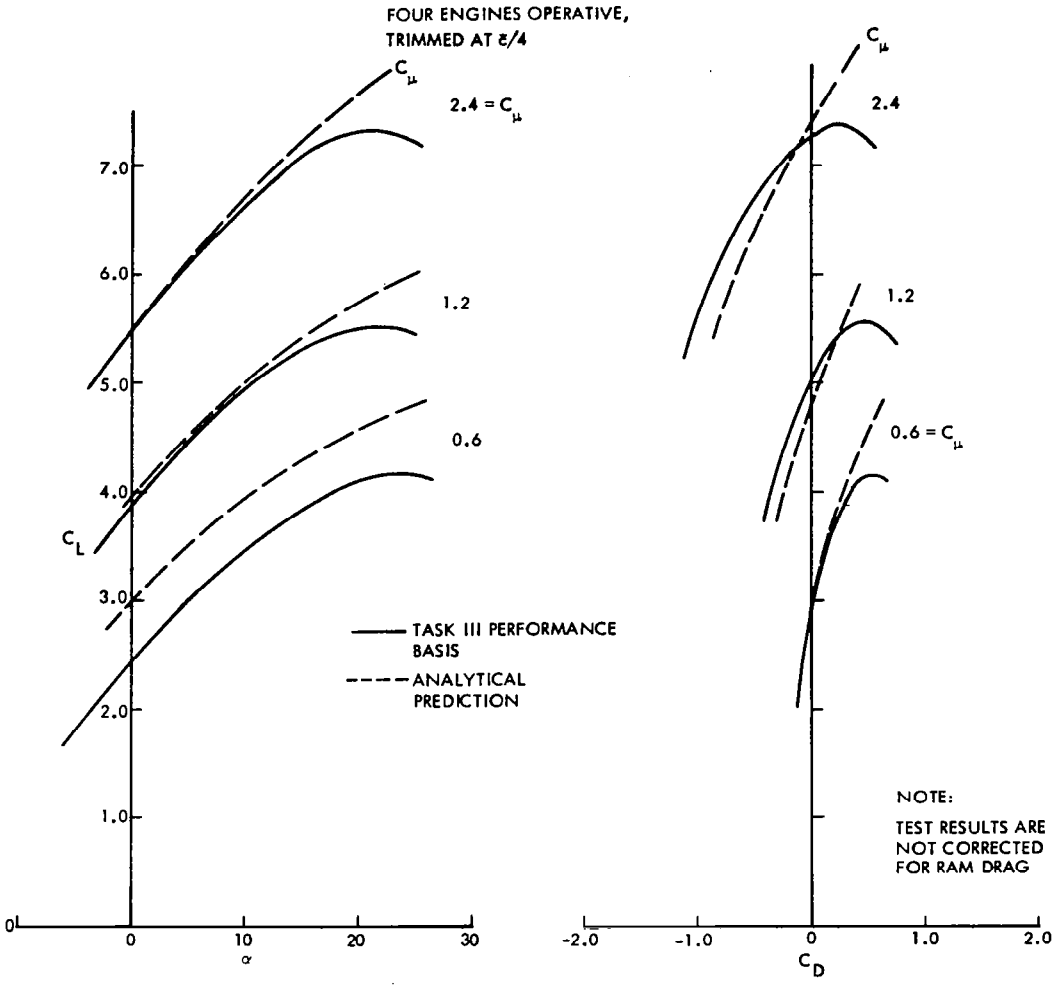


Figure 70. Comparison of Task III USB configuration performance with math model prediction, $\eta_t = 0.90$, $\delta_f = 45^\circ$

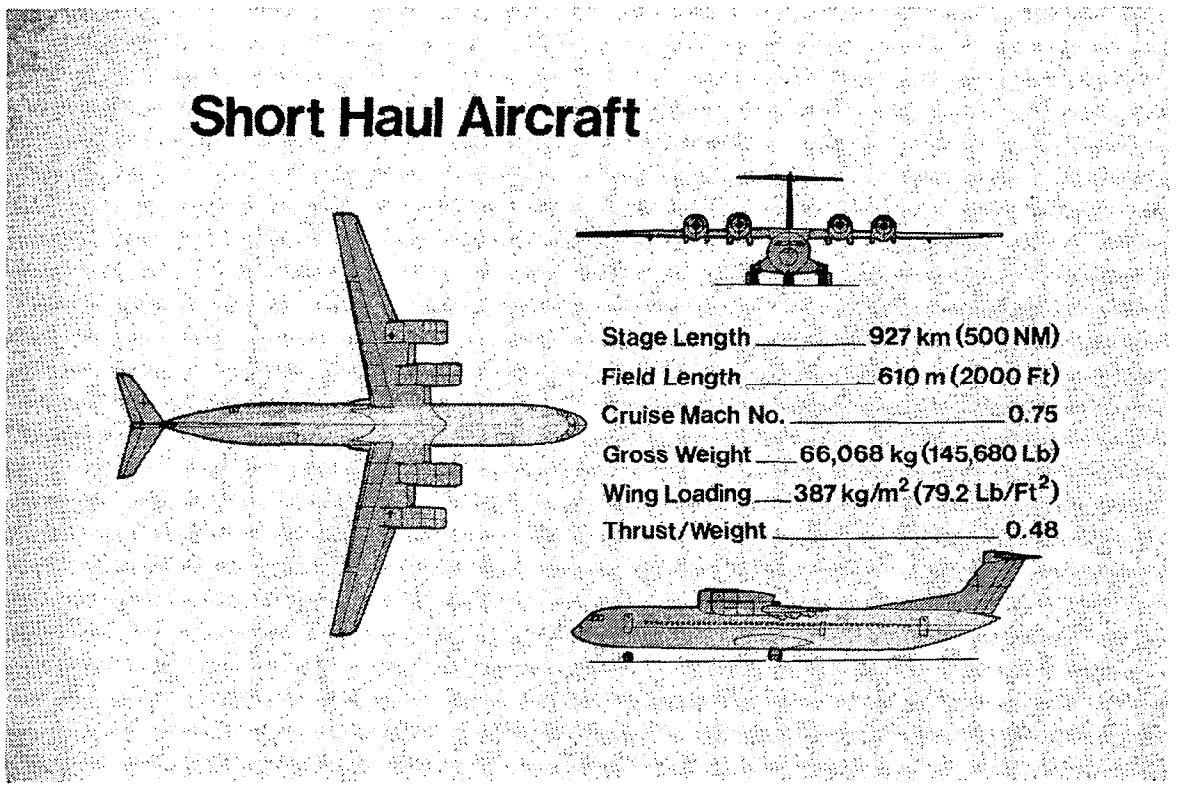


Figure 71. Task III short haul aircraft

## 7.0 CONCLUSIONS

As a result of low-speed, high-lift tests and analysis of a representative USB-model configuration, the following conclusions are drawn:

(1) As tested with the same model hardware, the USB system provided competitive performance with a similar EBF system.

(2) The subject USB test data compared favorably with test results on a large-scale model of a two-engine USB arrangement.

(3) A loss in lift up to stall of $\Delta C_L$ = 0.10 to 0.15 per nacelle was found with the Coanda plate removed and flap slots blocked on the undersurface of the trailing-edge device.

(4) Analytical synthesis of the high-lift configuration showed excellent agreement between calculated and test results.

(5) Analytical high-lift performance predictions for the Task III, four-engine airplane indicated that parametric estimates of the full-scale design were reasonably consistent with test results with the latter conservatively corrected for potential performance penalties.

(6) Additional work is needed to configure the wing leading-edge/nacelle junctures properly for both cruise and high-lift performance when considering four-engine aircraft.

## 8.0 REFERENCES

1. Aoyagi, K., Falarski, M. D., and Koenig, D. G., "Wind Tunnel Investigation of a Large-Scale Upper Surface Blown-Flap Transport Model Having Two Engines," NASA Ames TMX-62, 296, August 1973.

2. Aoyagi, K., Falarski, M. D., and Koenig, D. G., "Wind Tunnel Investigation of a Large-Scale Upper Surface Blown-Flap Model Having Four Engines," NASA Ames TMX-62, 419, 1975.

| 1. Report No. | 2. Government Accession No. | 3. Recipient's Catalog No. |
|---|---|---|
| NASA CR-3192 | | |

| 4. Title and Subtitle | 5. Report Date |
|---|---|
| EXPLORATORY STUDIES OF THE CRUISE PERFORMANCE OF UPPER SURFACE BLOWN CONFIGURATIONS. Experimental Program - Test Facilities, Model Design, Instrumentation, and Low-Speed, High-Lift Tests | June 1980 |
| | 6. Performing Organization Code |
| 7. Author(s) | 8. Performing Organization Report No. |
| J. A. Braden, J. P. Hancock, K. P. Burdges, and J. E. Hackett | LG77ER0028 |
| | 10. Work Unit No. |
| 9. Performing Organization Name and Address | 11. Contract or Grant No. |
| Lockheed-Georgia Company<br>86 South Cobb Drive<br>Marietta, Georgia 30063 | NAS1-13871 |
| | 13. Type of Report and Period Covered |
| 12. Sponsoring Agency Name and Address | Contractor Report |
| National Aeronautics and Space Administration<br>Washington, DC 20546 | 14. Sponsoring Agency Code |

15. Supplementary Notes

Part of a series of Reports Covering Various Phases of the USB Program: CR-3193, CR-3192, CR-159134, CR-159135, CR-159136

Langley Technical Monitor: William C. Sleeman, Jr.

16. Abstract

The present report describes the model hardware, test facilities and instrumentation utilized in an experimental study of upper-surface blown (USB) configurations at cruise. The high-speed (subsonic) experimental work, studying the aerodynamic effects of wing-nacelle geometric variations, was conducted around semi-span model configurations composed of diversified, interchangeable components. Power simulation was provided by high-pressure air ducted through closed forebody nacelles. Nozzle geometry was varied across size, exit aspect ratio, exit position and boattail angle. Both 3-D force and 2-D pressure measurements were obtained at cruise Mach numbers from 0.5 to 0.8 and at nozzle pressure ratios up to about 3.0. The experimental investigation was supported by an analytical synthesis of the system using a vortex lattice representation with first-order power effects. Results are also presented from a compatibility study in which a short-haul transport is designed on the basis of the aerodynamic findings in the experimental study as well as acoustical data obtained in a concurrent program. High-lift test data are used to substantiate the projected performance of the selected transport design.

| 17. Key Words (Suggested by Author(s)) | 18. Distribution Statement |
|---|---|
| Subsonic cruise performance<br>Propulsion integration<br>High-lift<br>Transport design | Unclassified - Unlimited<br><br>Subject Category 02 |

| 19. Security Classif. (of this report) | 20. Security Classif. (of this page) | 21. No. of Pages | 22. Price* |
|---|---|---|---|
| UNCLASSIFIED | UNCLASSIFIED | 110 | $6.50 |

* For sale by the National Technical Information Service, Springfield, Virginia 22161

NASA-Langley, 1980